SURFACE SCIENCE STUDIES OF OXIDIZED ZIRCONIUM

by

YANGMEI WANG

B.Sc., Xiamen University, 1990

A THESIS SUBMITTED IN PARTIAL FULFILLMENT OF THE

REQUIREMENTS FOR THE DEGREE OF

DOCTOR OF PHILOSOPHY

in

THE FACULTY OF GRADUATE STUDIES

Department of Chemistry

We accept this thesis as conforming

to the required standard

THE UNIVERSITY OF BRITISH COLUMBIA

November 1996

In presenting this thesis in partial fulfilment of the requirements for an advanced degree at the University of British Columbia, I agree that the Library shall make it freely available for reference and study. I further agree that permission for extensive copying of this thesis for scholarly purposes may be granted by the head of my department or by his or her representatives. It is understood that copying or publication of this thesis for financial gain shall not be allowed without my written permission.

Department of _Chemistry_

The University of British Columbia
Vancouver, Canada

Date _December 16, 1996_

DE-6 (2/88)

Abstract

Oxidized zirconium surfaces have been studied by X-ray photoelectron spectroscopy (XPS) and low-energy electron diffraction (LEED). The aim is to provide a fundamental understanding of the chemistry and structure of such surfaces as well as for metal-oxide interfaces; the motivation is to help establish understanding in relation to problems associated with nuclear reactor pressure tube corrosion.

The chemistry of a thin film (~20 Å) of oxidized zirconium was studied by XPS. The film, prepared by depositing zirconium onto Au foil in the presence of a H_2O atmosphere in the low 10^{-9} Torr range, has an outer region of ZrO_2 and inner regions containing a lower oxidation state material, ZrO_x, as well as Zr-Au alloy. Initially both ZrO_x and the Zr-Au alloy are oxidized by either H_2O or O_2 at 300°C, although this process is hindered as the ZrO_2 layer gets thicker. However, even with the protective oxide layer, heating in 4×10^{-7} Torr D_2 (with a partial pressure of H_2O at around 1×10^{-9} Torr) can result in all the zirconium being converted to the +4 oxidation state; the process is apparently facilitated by migrating D atoms.

The evolution of structure at the Zr(0001) surface, after exposure to O_2 and an ordering anneal at 220°C, has been studied systematically using LEED crystallography. Additionally, a new analysis was undertaken for the clean Zr(0001) surface, which is confirmed to have a regular hcp-type structure, with a slight contraction (about 1.6%) in the first Zr-Zr interlayer spacing with respect to the bulk value (2.57 Å). The surface formed by a 0.5 monolayer (ML) of O manifests a (2×2)-type LEED pattern. A detailed analysis showed a novel structure with 0.25 ML of O at octahedral hole sites in (2×2) arrays, both between the first and second metal layers and between the second and third layers; these O arrays are displaced laterally from one another, apparently to minimize the O...O repulsions. The incorporated O atoms induce vertical and lateral relaxations

in the metallic structure, which are most significant in the second metal layer. The average O-Zr bond length of 2.28 Å is close to the value (2.30 Å) in bulk ZrO, which also has 6-coordinated O atoms.

For the surface formed by 1 ML of O at Zr(0001), the LEED analysis indicates a structural model where 0.5 ML of O is distributed randomly over octahedral holes between the first and second metal layers, with another 0.5 ML between the second and the third layers. The structural type changes for 2 ML of O at Zr(0001); now O bonds at 1 ML coverage in overlayer hollow sites of three-fold coordination, while there is another 1 ML of O atoms in tetrahedral hole sites between the first and second metal layers. The stacking sequence, designated as (C)B(A)AB.., corresponds to the first three layers of anion-terminated cubic ZrO_2, although some lateral compression is needed for superposition on the regular hcp Zr structure. The absorption of O in tetrahedral holes between the first and second metal layers results in a significant expansion to about 3.44 Å. The O-Zr bond lengths are estimated to equal 2.07 Å for the overlayer O atoms, and 2.22 Å for the O atoms in tetrahedral hole sites.

Table of Contents

List of Tables

List of Figures

Acknowledgments

I would first like to thank my supervisor, Professor K.A.R. Mitchell, for directing me towards challenging research in surface science, and for his encouragement and guidance throughout this thesis.

I owe special gratitude to Dr. P.C. Wong and Dr. Y.S. Li for introducing me to various surface science techniques, and for sharing their valuable experience on the projects described here. My collaboration with them has been very enjoyable and instructive. I am grateful to Prof. M.Y. Zhou especially for helping me start this journey. I thank Dr. D.T. Vu for teaching me the TLEED computer program and Dr. B.J. Flinn for many helpful discussions throughout this research. I have also appreciated my collaboration with Dr. H. Wang in setting up the HREELS system. Throughout I have greatly enjoyed my interactions with other colleagues in our Surface Science Laboratory including Ms. Y.L. Leung, Ms. W.F. Heung, Ms. M. Kono, Mr. Wei Liu, Mr. K.C. Wong, Ms. J. Fang, Mr. M. Saidy, and Ms. D. Susac.

Special thanks are due to Dr. M.A. Van Hove (University of California, Berkeley) for providing computer codes used in the LEED crystallography research. I am also indebted to the staff in the Mechanical and Electronic shops for their continuous assistance in developing and maintaining our equipment.

Finally, but most importantly, I wish to express my deepest gratitude and love to my parents, my sister and my husband, Hong Chen, for their continuous encouragement and support throughout these years of study. To them, I dedicate this thesis.

Chapter 1: Introduction

1.1 Motivation

There has been significant interest in the study of the oxidation of metallic zirconium in both polycrystalline and single-crystal forms [1-19]. The motivation for this interest relates to various applications in materials science and technology of either the metal itself in an oxidizing environment or the coating material ZrO_2 [3,5,20]. Indeed both aspects are involved when zirconium is used as the main component of the structural material for nuclear reactor pressure tubes insofar as an outer film of oxide is generally assumed to provide corrosion resistance. In the particular example of the CANDU reactor [21], the pressure tube material is around 97% zirconium with niobium added to help the mechanical properties, but other impurity elements are present too. The passivation layer is believed to be dominantly zirconium oxide (ZrO_2), and a traditional view has been that this oxide film helps prevent the ingress of hydrogen or other gases into the metal under the operating conditions. However, on occasion, corrosion does occur, apparently resulting from hydrogen penetration through the oxide film and into the metal. The consequent embrittlement of the latter can raise safety concerns and necessitate reactor shutdown with high economic cost.

A current problem for Atomic Energy of Canada Ltd. (AECL) is that the chemistry of the passivating layer on the zirconium alloys is not well understood, and in particular, the detailed mechanisms for the interaction of CANDU pressure tube surfaces with its operating environment, including O_2, D_2O, D_2, and CO_2, are still unknown. To increase basic knowledge, with the view to overcoming the occasional failure problem, AECL has been coordinating a program directed at developing a predictive model for hydrogen ingress and corrosion in the

CANDU reactor pressure tube. To a considerable extent, this requires breaking down a complex problem, and gaining understanding of the most important component parts. In such an approach, one key reference point is provided by the properties of oxidized zirconium surfaces, including atomic-level structure and chemistry at the oxide-metal interface. The existence of basic information on mechanistic features such as dissociative adsorption, binding sites and atomic incorporation appears essential for developing understanding of reactions between oxidized zirconium surfaces and other chemical components in the CANDU reactor environment.

1.2 Surface Science Methods Applied to the O/Zr System

A surface, or more generally an interface, corresponds to the boundary region between two different phases in contact. Frequently, the chemical and physical properties of the surface region of a solid are different from those in the bulk [22]. Whereas bulk atoms are surrounded on all sides by neighbors, surface atoms are surrounded by neighbors only on one side and thus have unsatisfied bonding capacity. As a result, the surface free energy is higher than that of the bulk, and surface atoms have a strong tendency to lower their energy by forming additional bonds through adsorption or by undergoing a surface relaxation or reconstruction. Surface science studies not only topmost atomic layers, but all near layers which may be involved in surface restructurings or reactions. Information gained from fundamental surface science studies has helped to increase understanding in a range of diverse fields of technological importance, including heterogeneous catalysis, adhesion and microelectronics [23-25].

There is a large variety of surface sensitive techniques available for the study of elemental composition, chemical state and structure of the outermost layers of a solid. Table 1.1 lists some

Table 1.1   Summary of some techniques for surface structure and analysis.

Technique	Acronym	Physical measurement	Information gained	Refs.
Auger electron spectroscopy	AES	kinetic energies of electrons emitted by two electron de-excitation of core hole	elemental composition	[26,27]
Infrared Spectroscopy	RAIRS FTIR	absorption of IR radiation as function of energy	$\perp$ vibrational modes	[28]
Low energy electron diffraction	LEED	elastic electron back diffraction	atomic structure and bonding	[29-31]
Nuclear reaction analysis	NRA	yield of emitted particle from a nuclear reaction as function of areal density of emitting atoms	coverage of adsorbate, layer thickness	[32]
Secondary ion mass spectrometry	SIMS	ions sputtered from surface measured in mass spectrometer	elemental composition	[33]
Thermal desorption s spectroscopy	TDS	desorbed species as a function of sample temperature	desorption energy, multiple bonding states	[34]
X-ray photoelectron spectroscopy	XPS	photoemission of core electrons	elemental composition, chemical states	[26,27]
Work-function	$\Delta\phi$	work function changes as function of sample treatment	surface dipole, location of adsorbed species	[35]

3

techniques with relevance to the O/Zr system. Each approach has its own advantages and emphasizes different aspects of the system concerned. Among these techniques, Auger electron spectroscopy (AES) and X-ray photoelectron spectroscopy (XPS) [26,27] are extremely important for chemical analysis and for identifying surface species present; on the other hand, low-energy electron diffraction (LEED) [29-31,36] is the most developed technique for determining ordered surface structure.

The current evidence is that the interaction of oxygen with zirconium surfaces at room temperature yields almost complete dissociation, and that with heating surface to bulk diffusion occurs rather than desorption [1,3]. LEED observations for low oxygen exposures on the (0001) surface of single crystal zirconium showed the existence of a (2×2)-type LEED pattern, and that the surface evolves through two different (1×1)-type structures at higher coverage [14,15]. A preliminary LEED crystallographic analysis [14] indicated that the structure which exhibits a (2×2)-type pattern involves oxygen incorporation into octahedral sites. However, uncertainty remained on whether the incorporated O atoms induced some reconstruction in the metal layers. As well, the depth of O incorporation was still in question. Work function studies [12,17] indicated that oxygen can migrate into subsurface sites even at 90 K, and that they do not migrate deeper below the surface for temperature less than about 230°C [17]. At room temperature, Griffiths [12] found that the interaction of oxygen with Zr(0001) decreased the work function (ϕ), and that a (2×2) LEED pattern of optimal sharpness was formed at the minimum in $\Delta\phi$. Using nuclear reaction analysis (NRA), Zhang *et al.* [17] also found that the sharpest (2×2) pattern corresponds to an oxygen coverage of 0.5 monolayer (ML), and that the formation of the lowest-coverage (1×1) structure corresponds to 1 ML coverage of O. Although initial studies have been

made, an overall picture for the structural evolution with coverage was lacking for this system; definite structural details are clearly needed for the three surface structures involved.

The oxidation of zirconium has been a subject of continuing interest over the past 15 years. AES studies by Tomita *et al.* [9] and Sanz *et al.* [11] have supported the view that below 300°C, the oxidation proceeds through three stages, specifically, dissociative chemisorption, nucleation of oxide on the surface and growth of an oxide layer. XPS has indicated different chemical states of zirconium during the oxidation process; for example, Sen *et al.* [6] and De González *et al.* [7] suggested the formation of the oxides Zr_2O, ZrO, Zr_2O_3, ZrO_2, although using quantitative AES analysis, Tomita *et al.* [9] emphasized the presence of nonstoichiometric oxygen solution in zirconium instead of the formation of real compound suboxides. Nevertheless, all [6,7,9] seem to agree that lower oxidation states for Zr exist in the region between oxide (ZrO_2) and metal. However, little is known about the chemistry of this oxide-metal interface, especially with regard to its stability in oxidizing and hydriding environments.

Initial work has been done for the interaction of H_2 and H_2O with the (0001) surface of single-crystal Zr [37,38] using a variety of surface science techniques, including thermal desorption spectroscopy (TDS). However, so far most effort has been applied to heavily oxidized polycrystalline samples [39-44]. For example, the behavior of CANDU nuclear reactor material in such environments has been studied with secondary ion mass spectroscopy (SIMS), NRA and other materials characterization techniques [40-43] to help establish that the corrosion of the underlying metal relates to H ingress through the zirconium oxide film. AES and electron energy loss spectroscopy studies [3] have revealed that atomic hydrogen can reduce a polycrystalline ZrO_2 sample at 890°C with desorption of H_2O. Additionally, infrared spectroscopy (IR) studies [43,44] have identified OH vibrations when H_2 was introduced to ZrO_2 at room temperature. Although observations have been made, the mechanistic behaviors of

hydrogen in zirconium oxide are still far from being understood, and there remains a paucity of information for the oxide-metal interface in the presence of H. Such knowledge is required for developing models of the CANDU pressure tube in its operating environment.

The O/Zr system represents a challenge for studying with surface science techniques whether starting from well-characterized samples of either Zr or ZrO_2. For the first, the preparation of clean, well-defined samples is complicated by both (i) the bulk phase change (from α-zirconium (hcp structure) to β-zirconium (fcc structure)) at 863°C which prevents heating samples to much above 800°C in practice, and (ii) the extremely high reactivity of this metal. Both effects complicate the cleaning of this metal for surface science study. On the other hand, appropriate macroscopic samples of ZrO_2 are not available. The familiar large cubic crystals of ZrO_2 are impurity stabilized (e.g. with Y, Ca), but crystals of pure ZrO_2 (the mineral baddeleyite) are heavily twinned [45] and are too small for surface science study. Therefore, for these applications, the oxide samples have to be specially prepared. Many previous studies of the reactivity of zirconium metal with oxygen have been made on thick oxide films prepared by oxidizing macroscopic zirconium under high oxygen exposures, but they can suffer from the fact that the interface between the oxide and underlying bulk metal occurs too deep down to be well probed by electron spectroscopic techniques. Such observations provide background to the starting point for the research described in this thesis.

1.3 Objectives for This Work

The work in this thesis aims to contribute to an understanding of the atomic-level structures and chemistry of oxidized zirconium surfaces, and to help establish approaches to meet the challenges of studying such systems, particularly in relation to the problem noted for the

6

CANDU reactor pressure tube. It is hoped that information gained from this research will provide a reference for the more mechanistic studies in the future which should contribute to the establishment of a predictive model for the pressure tube corrosion.

Three specific objectives are identified for this work:

(1) To identify factors involved in the different oxidation states seen by XPS when thin ZrO_2 films are grown on Zr metal, and when they are exposed to reactive environments involving H.

(2) To determine detailed structures identified during the interaction of oxygen with the Zr(0001) surface in the 0.5 to 2 ML (monolayer) regime.

(3) To identify approaches for determining mechanistic aspects of the interaction of H-containing molecules with interfaces associated with real pressure tube material.

The thesis is organized as follows. Chapter 2 introduces the general principles and experimental setups for the XPS and AES techniques, and Chapter 3 reports new XPS studies on the stability and reactivity of thin films of oxidized zirconium deposited on an inert substrate. Chapter 4 reviews approaches for determining surface structure using LEED crystallography, while Chapters 5 and 6 report LEED analyses for the structural evolution of O incorporated into the Zr(0001) surface. Specifically, structural determinations are given in Chapter 5 for the clean Zr(0001) surface and for the surface with 0.5 ML of O, while those for the 1 ML and 2 ML surfaces are given in Chapter 6. Finally, Chapter 7 offers some suggestions for further studies on the O/Zr system in terms of the overall objectives noted above.

Chapter 2: Electron Spectroscopy for Chemical Analysis

2.1 Introduction

Analysis of a surface region for its chemical composition represents a particularly crucial characterization in surface science, and such information, along with geometrical structure, represents the most fundamental knowledge needed to understand the properties of a particular surface system. Two key analytical techniques in surface science are provided by Auger electron spectroscopy (AES) and X-ray photoelectron spectroscopy (XPS) [26], for which brief introductions are given in this chapter. Research in Chapter 3 discusses work with XPS, but since Auger spectra can be produced at the same time, it is convenient to introduce them together now.

The experiment of XPS involves irradiating a sample surface with an X-ray beam and determining the distribution of kinetic energies for the emitted photoelectrons. To a first approximation, the kinetic energy of a photoelectron is

$$E_k = h\nu - E_b \tag{2.1}$$

where $h\nu$ is the photon energy and E_b is the binding energy of the electron in the sample. Since different elements have different sets of electronic binding energies, elemental identification is possible through measurement of photoelectron kinetic energies. Figure 2.1 schematically shows the production of such a photoelectron, and in addition shows two possible de-excitation mechanisms for the atomic core hole produced. One is X-ray emission, and the other is Auger emission produced by a two-electron, radiationless process. The probabilities for Auger electron and X-ray production vary with the atomic number Z and the binding energy associated with the core vacancy, but Auger production always dominates if the core binding energy is 2 keV or less
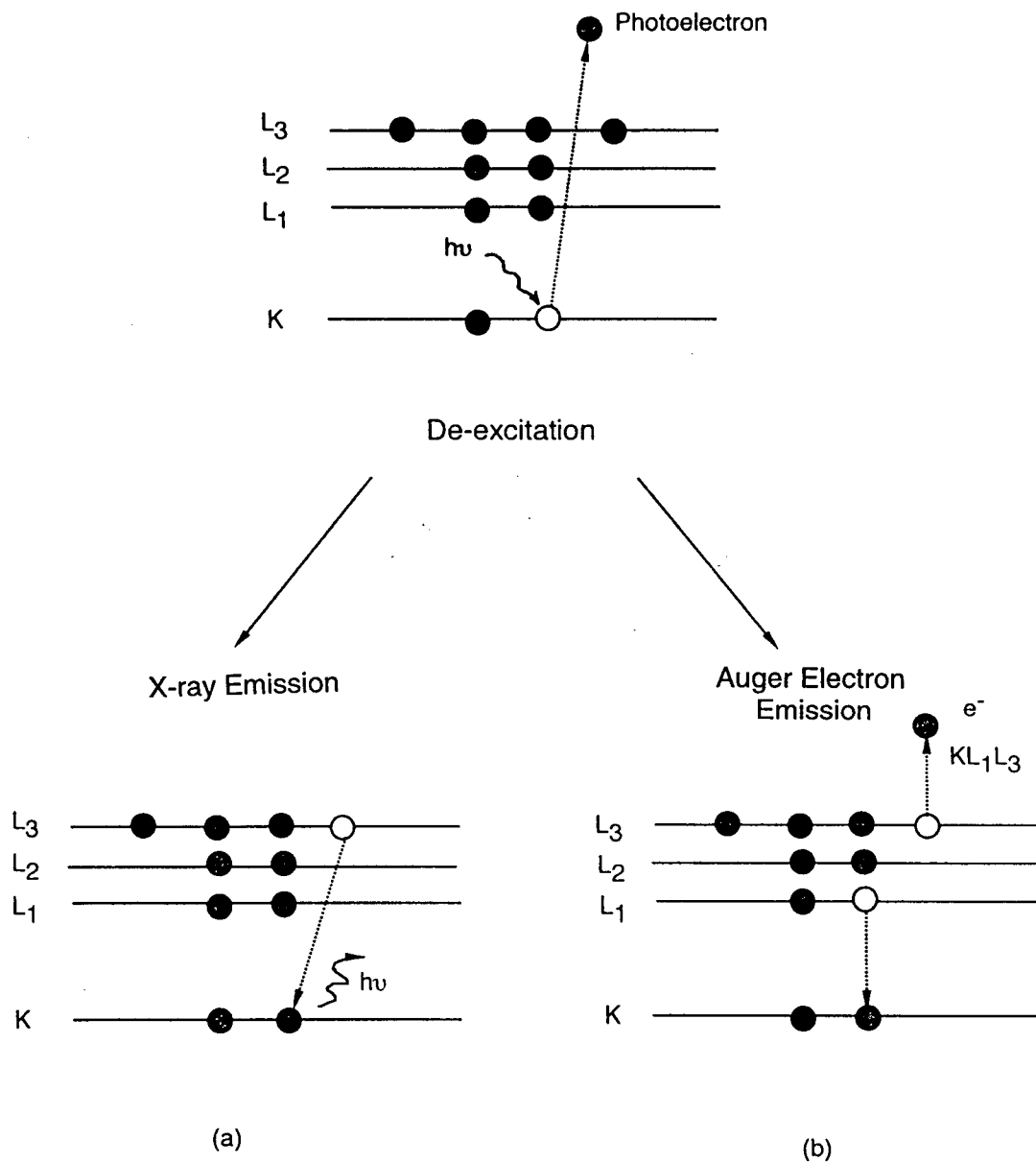
Figure 2.1   Production of a photoelectron by irradiation with soft X-rays and two processes for de-excitation of the atomic core hole produced: (a) X-ray emission and (b) Auger electron emission.

[46]. Figure 2.1 includes the production of a KL_1L_3 Auger electron whose kinetic energy, in a first approximation, is

$$E_{KL_1L_3} = E_K - E_{L_1} - E_{L_3} \qquad (2.2)$$

where E_K, E_{L_1}, E_{L_3} are the binding energies for the levels involved. Strictly some account is needed for relaxation and correlation effects [47], but the point for our purpose is that each element again has its characteristic set of Auger electron kinetic energies. These energies for one element are easily distinguishable from those of other elements, and this allows for elemental identification from measured spectra.

Figure 2.2 indicates the basic dependence of inelastic mean free path (IMFP, Λ) as a function of energy for various materials. The IMFP can be defined as the average distance traveled by an electron in the material without energy loss; empirical values of the IMFP have been provided by Seah and Dench [49]. Frequently the measured kinetic energies of photoelectrons or Auger electrons are in the 100 to 1000 eV range, and, as shown in Figure 2.2, electrons in this energy range have a high probability to experience inelastic scattering in a solid. Inelastic mean free paths of 6 to 20 Å are typical in this energy range and this makes XPS and AES surface sensitive techniques.

The origin of XPS can be traced back to the earliest investigations of the photoelectric effect [50], and measurements of the kinetic energy distributions for electrons resulting from X-ray irradiation of solid materials were reported over 70 years ago [51]. However, it was only during the middle of this century that developments, especially by Siegbahn, led to the current awareness of this technique. He coined the acronym ESCA (electron spectroscopy for chemical analysis) to underline the fact that both photo *and* Auger electron peaks appear in the 'XPS' spectrum [52]. In 1972, Brundle and Roberts performed XPS studies on carefully prepared
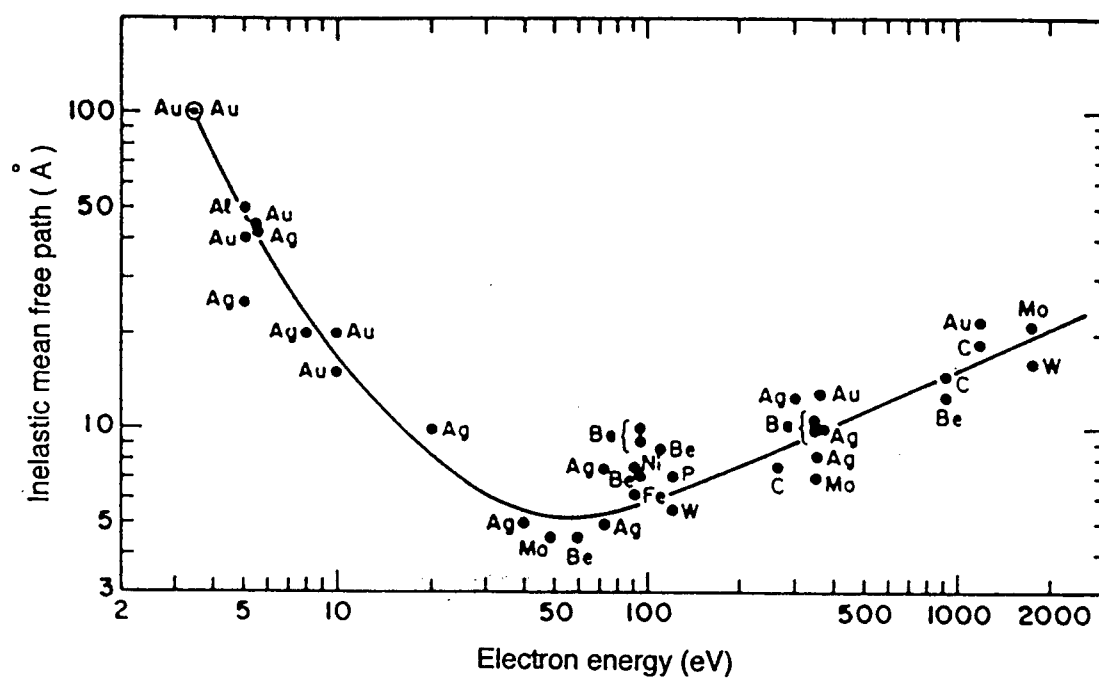
Figure 2.2   Representative inelastic mean free path of electrons in a solid as a function of kinetic energy [48].

surfaces under ultrahigh vacuum conditions [53], and that work first established XPS as a surface analytical technique.

2.2 Auger Electron Spectroscopy (AES)

Auger electrons can be emitted from a solid, through the mechanism indicated in Figure 2.1, resulting from interaction with either an X-ray or energetic electron beam. The latter is used in AES measurements to complement the LEED research reported later in this thesis. Figure 2.3 (a) shows an Auger spectrum in the form of number of electrons (N(E)) versus kinetic energy (E), measured from a thin film of oxidized zirconium deposited onto a gold foil. The emission of Auger electrons appears as small features superimposed on the large background of secondary electrons, and the usual practice is to generate the dN(E)/dE function (Figure 2.3 (b)). This helps make weak features more readily identifiable over regions for which the background is essentially constant. Changes in Auger spectra (e.g. peak shape and position) can occur when the local bonding environment around the atom being analyzed changes [54]. However, since the Auger process involves three energy levels, these changes are generally less easy to interpret than is the case with XPS [55].

The peak-to-peak distance in differentiated Auger spectra for a particular element give a measure of relative surface concentration provided the original peak shapes are constant [56]. But the Auger current also depends on the various experimental parameters used, such as incidence angle, energy of primary beam, and modulation voltage. Therefore, surface concentrations can be compared this way only when the measurement device, and all its working parameters are held constant [26].
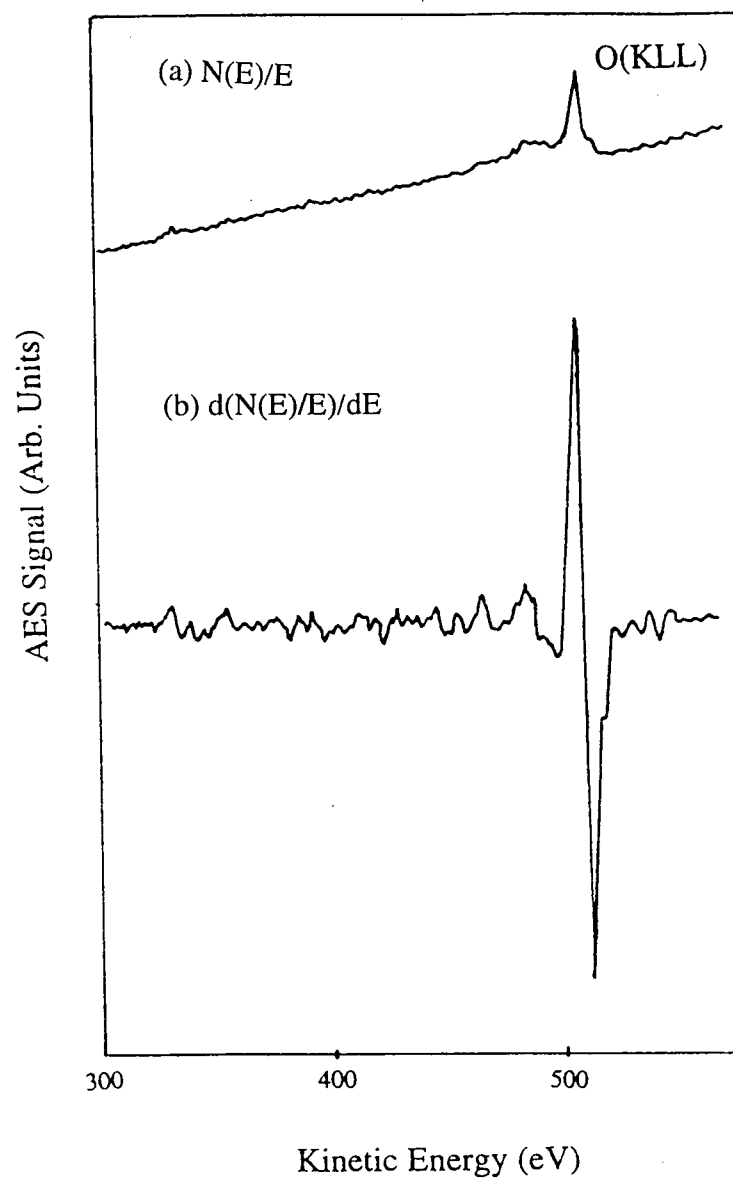
Figure 2.3   Two representations of an O (KLL) Auger electron spectrum measured with a concentric hemispherical analyzer: (a) as N(E)/E vs E and (b) as d(N(E)/E)/dE vs E.

In this thesis, Auger spectra are initially used for qualitative analysis, and this depends on assigning peaks to particular elements with the aid of listed Auger energies [57]. Additionally, the ratio of peak-to-peak distances for adsorbate and substrate is frequently used as a measure of relative coverage for the adsorbate.

2.3 X-ray Photoelectron Spectroscopy (XPS)

2.3.1 Qualitative Analysis

The XPS experiment involves energy analysis of photoelectrons emitted from a sample after irradiating with soft X-rays. An example of a survey scan spectrum is illustrated in Figure 2.4 (a). This spectrum was measured from a cleaned gold foil, and it exhibits sharp peaks, which correspond to the binding energies of the elastically emitted photoelectrons. These peaks directly manifest the core electron structure of the material (e.g. the 4s, 4p, 4d and 4f levels). At higher resolution, doublet structure is seen for photoelectrons from states with nonzero orbital angular momentum (i.e. p, d, f core levels) as a result of spin-orbit coupling. An example is given in Figure 2.4 (b) for a narrow scan spectrum for the Au 4f level. The different peaks are assigned by the j values (i.e. 1/2, 3/2 for p orbitals, 3/2, 5/2 for d orbitals, etc.); and the peak areas are determined by the respective $(2j+1)$ number of states. Accordingly Figure 2.4 (b) shows the $4f_{5/2}$ and $4f_{7/2}$ peaks with the peak intensity ratio of 3:4.

Figure 2.5 shows a survey scan from a thin film of oxidized zirconium deposited onto a gold foil. Now structure is seen from different elements; more generally peaks can be assigned by comparing with standard compilations [26,58], but, as noted in Figure 2.5, Auger peaks may also be observed. Additionally considerable background is present, for example, as a result of photoemission by Bremsstrahlung radiation. Throughout prominent structure is accompanied by

(a)

(b)
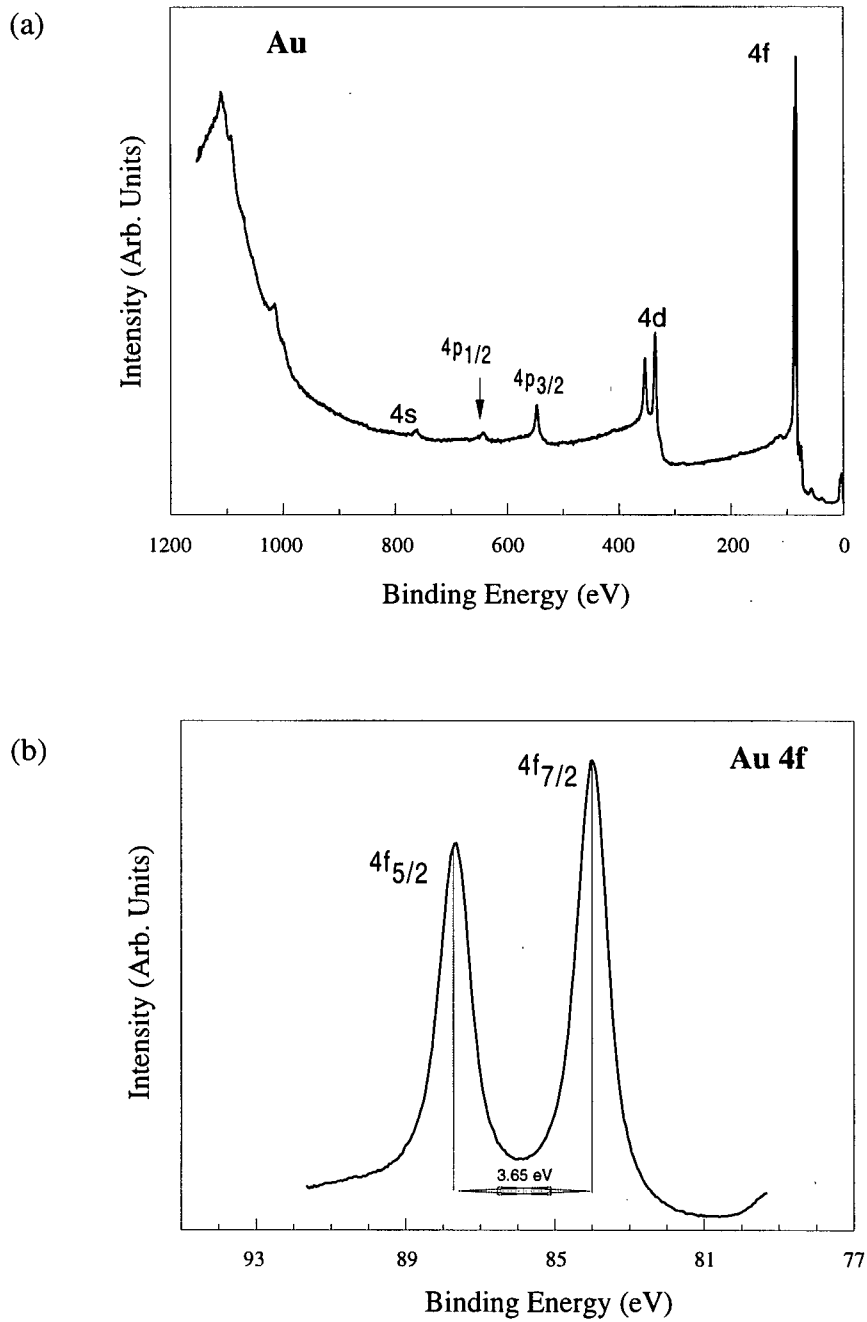
Figure 2.4   Photoelectron spectra from a cleaned Au sample: (a) survey spectrum, (b) high-resolution Au 4f spectrum showing characteristic spin-orbit splitting.
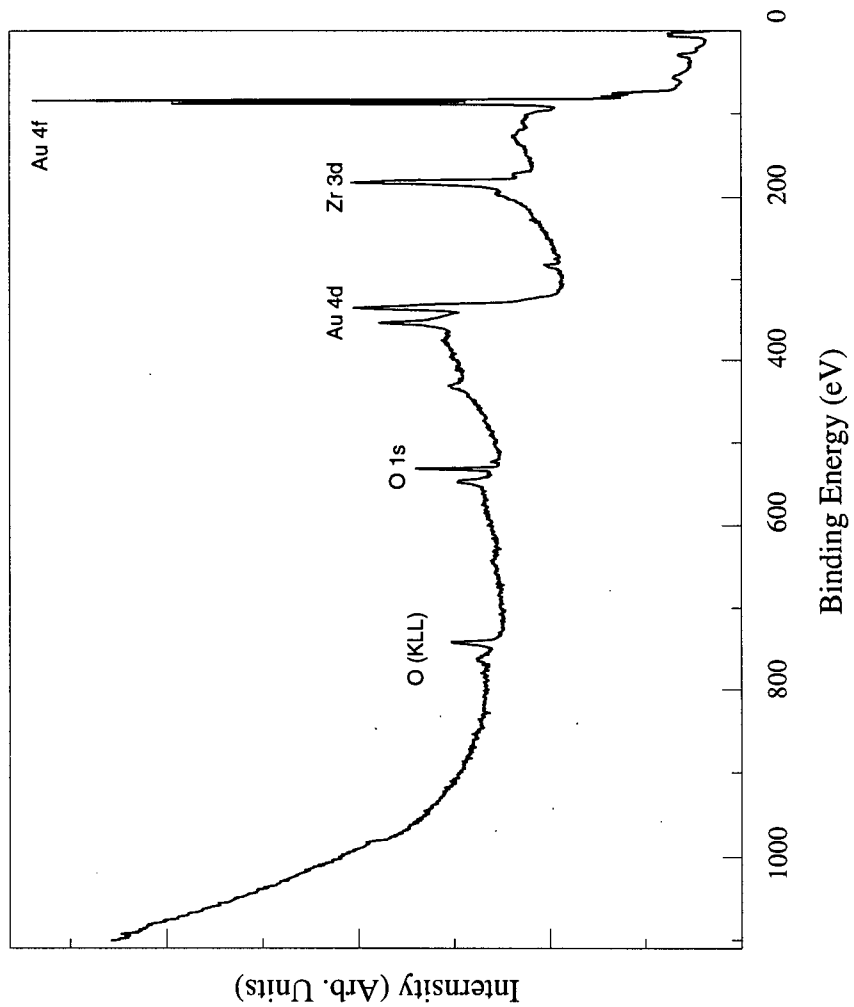
Figure 2.5   Survey scan of a thin oxidized zirconium film deposited onto a gold foil.

a high binding energy tail, which corresponds to photoelectrons which have undergone inelastic scattering on their outward path, so emerging with lower kinetic energy.

In addition to elemental analysis, the presence of the same type of atom, but in different chemical states, can be identified through interpretations of chemical shifts. This follows observations that binding energies of the inner core electrons are influenced by changes in the valence electron environment. An example is shown in Figure 2.6 for a narrow scan of a Al2p spectrum from an aluminum alloy with a native oxide layer; the peak at 71.5 eV is identified as from metallic aluminum, while that at 74.1 eV is from the oxide. This interpretation follows the expectation that Al in the oxide will have a net positive charge, and hence a higher binding energy, compared with the metallic Al. More generally, the distinct chemical states give rise to overlapping peaks. Then a curve synthesis process is required to identify the different contributions from a measured spectrum; this is discussed further in Section 2.4.3 and Chapter 3.

2.3.2 Quantification

The intensity of a photoelectron peak is generally taken to be proportional to the area of the peak determined after background correction to remove contributions from inelastically scattered electrons. The sampling depth for these electrons is conventionally taken to be 3Λ; that is the depth from which 95% of the signal is contributed. For the time being we assume that the photoelectrons are collected in the normal exit direction.

The number of photoelectrons collected by the analyzer per unit time depends on the X-ray flux (F), the photoelectron cross section (σ), the number of relevant atoms per unit volume (D), the area of the sample from which the photoelectrons are collected (A), the instrumental
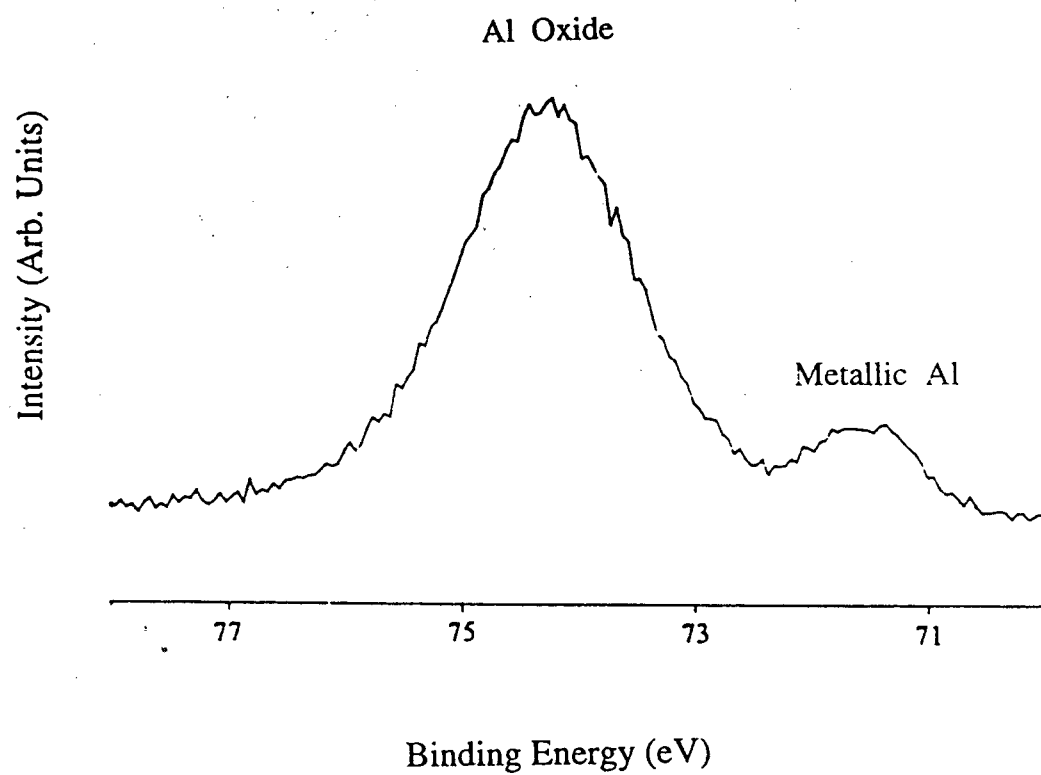
Figure 2.6   High-resolution spectrum of a Al2p photoelectron peak from an aluminum alloy with native oxide layer [59].

detection efficiency (T) and the inelastic mean free path (Λ). The contribution to the intensity

from an incremental thickness dx in the sample (Figure 2.8 (a)) is:

$$dI = f\sigma DAT \exp(-\frac{x}{\Lambda})dx \qquad (2.3)$$

Simple integration from $x=0$ to $x=\infty$ for a semi-infinite homogeneous sample then gives:

$$I = \int_0^\infty f\sigma DAT \exp(-\frac{x}{\Lambda})dx = f\sigma DAT\Lambda \qquad (2.4)$$

A commonly used approach for comparing relative compositions of two elements in a

sample is to group the instrumental factors f, A, T, as well as σ (for each particular photoelectron

peak), into a sensitivity factor S. Such factors, expressed relative to the F 1s peak, are available

for the MAX200 spectrometer where the transmission function from the manufacturer corrects

for the particular instrumental conditions used for each measurement [60]. Then the composition

ratio for two elements in a sample can be expressed as :

$$\frac{D_1}{D_2} = \left(\frac{I_1/S_1}{I_2/S_2}\right)\left(\frac{\Lambda_2}{\Lambda_1}\right) \qquad (2.5)$$

In principle, one can use tabulated values of Λ_1 and Λ_2 for the appropriate photoelectrons in the

material of interest [49]. For semiquantitative work, a common practice is to take the ratio of

Λ_1/Λ_2 as effectively constant so that the ratio I_1/I_2, from the measured peak intensities, can help

estimate the elemental composition ratio D_1/D_2 within the depth probed.

2.3.3 Angular Dependent Measurement

Surface sensitivity can be enhanced by varying the take-off angle (θ, angle between the

plane of the surface and the axis of the energy analyzer) as illustrated in Figure 2.7. For normal

take-off ($\theta = 90°$), the sampling depth is 3Λ while at grazing angles of emergence, the sampling

Energy
Analyzer

Energy
Analyzer

X-ray source

X-ray source

90°

take-off
angle

θ

3Λ

A

3Λ sinθ

A/sinθ
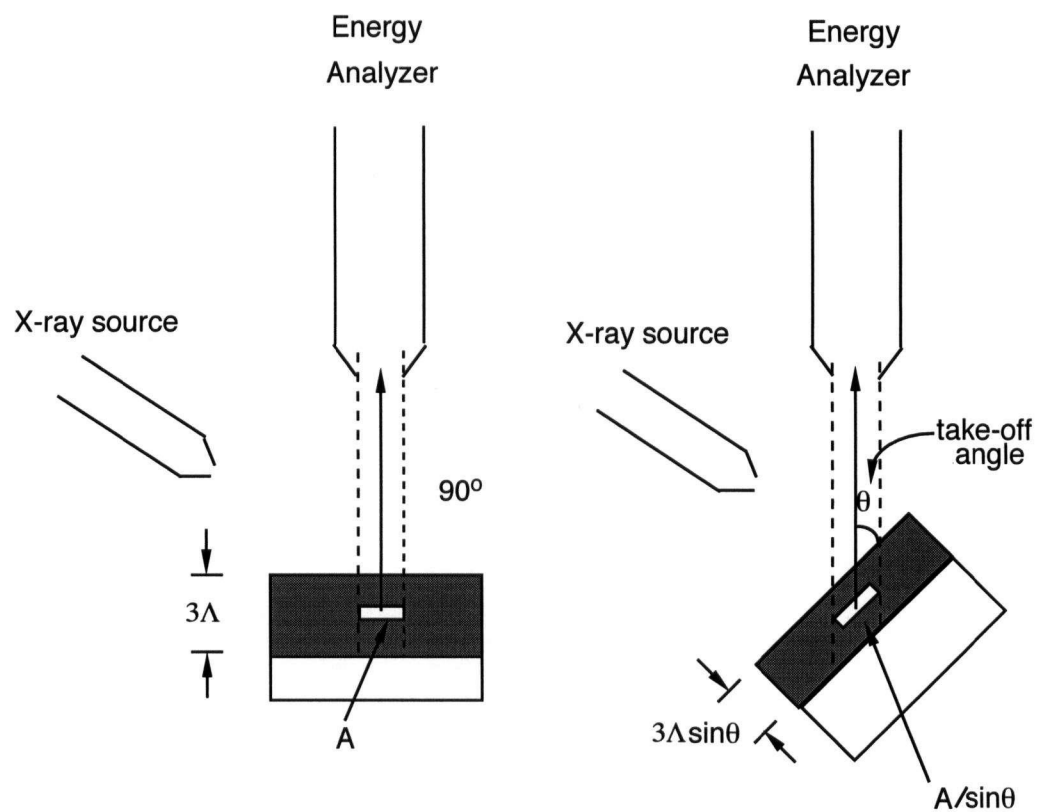
Figure 2.7   Illustration of the principle of angular dependent XPS.

depth is reduced to $3\Lambda\sin\theta$. Therefore contributions in spectra from surface species are more pronounced by making measurements with low take-off angle.

Figure 2.8 (b) illustrates a sample consisting of an overlayer (thickness d) on top of a substrate material. In relation to measurements associated with varying take-off angle θ, Eq.(2.3), after correcting for angular effects, integrates to yield:

$$I_s = f\sigma_s D_s A T \Lambda_s \exp\left(\frac{-d}{\Lambda_{so}\sin\theta}\right) \tag{2.6}$$

$$I_o = f\sigma_o D_o A T \Lambda_o \left[1 - \exp\left(\frac{-d}{\Lambda_o\sin\theta}\right)\right] \tag{2.7}$$

for photoelectron intensities from substrate and overlayer respectively. In Eq. (2.6) and (2.7), Λ_s and Λ_o are inelastic mean free paths for photoelectrons originating in, and traveling in, the substrate and overlayer respectively, while Λ_{so} is the inelastic mean free path of photoelectrons from the substrate traveling in the overlayer. The ratio I_o/I_s increases strongly as θ decreases, and Eqs. (2.6) and (2.7) can be useful in interpreting the relative orientation or composition gradients for different species for the assumed model [61]. Further, Eq. (2.6) can be modified to compare I_s values for different θ against that for normal exit ($\theta = 90°$) to yield:

$$\ln\left[\frac{I_s(\theta)}{I_s(90°)}\right] = \frac{-d}{\Lambda_{so}}\frac{1}{\sin\theta} + \frac{d}{\Lambda_{so}} \tag{2.8}$$

Then the overlayer thickness (d) can be determined from the slope of $\ln[I_s(\theta)/I_s(90°)]$ versus $1/\sin\theta$, provided information is available for Λ_{so}.

Eqs. (2.6) and (2.7) provide the basis for the most commonly used approaches of angular dependent XPS, including those made in this thesis. However other important developments should be mentioned briefly. First, there has been interest in developing quantitative information

(a)

photoelectron

hυ

0

dx

x

(b)

x=0

overlayer film | d

x=d
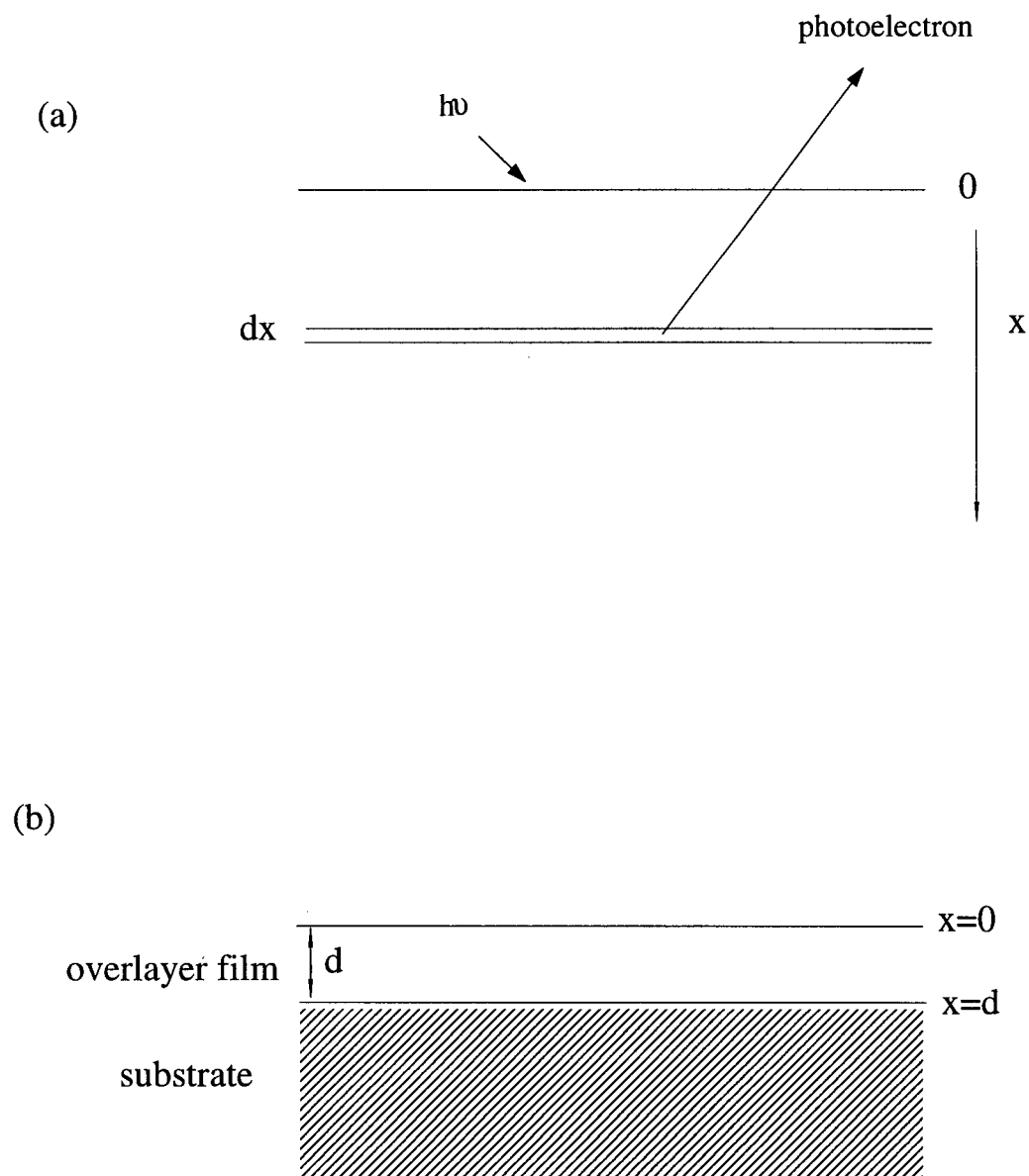
substrate

Figure 2.8   Some notation for: (a) a semi-infinite homogeneous sample and (b) a sample with an overlayer of thickness d on top of a substrate.

for more heterogeneous (i.e. less ideal) systems, and algorithms have been proposed for determining concentration-depth profiles from ADXPS measurements using least-squares fitting [62], and the Tikhonov regularization [63] and maximum entropy [64] methods. A recent review was given by Cumpson [65]. Second, the background to Eqs (2.6) and (2.7) effectively assumes that there are no preferred directions in the sample. This is not the case with single crystals where strong forward focusing effects are detected, and provide the basis for photoelectron diffraction [66]. The full background theory is like that for LEED (Chapter 4). The use of angular resolved measurements to determine local structural arrangements has great potential importance, particularly with third generation synchrotron radiation sources. Recent reviews have been given by Fadley *et al.* [67], Egelhoff [68] and Chambers [69].

2.4. Instrumentation for XPS

2.4.1 Ultrahigh Vacuum (UHV)

Modern surface science requires the use of ultrahigh vacuum (UHV), in which pressure is maintained below the 10^{-8} Torr region. This requirement is especially to keep a surface in an essentially constant state during the time for doing an experiment. According to the kinetic theory of gases [70], for CO or N_2 (with M=28) at room temperature and a pressure of 10^{-9} Torr, a surface can be completely covered by an adsorbed monolayer (ML) in about one hour if each colliding molecule sticks to the surface. In practice, sticking coefficients are often less than unity, but it is clear that background pressures (especially for reactive gases) around 10^{-10} Torr or less are necessary for well-controlled research over reasonable time spans. Low pressure is also needed to ensure that any particles, such as electrons and ions, being used in the experiment have a sufficiently long mean free path in order to travel from sample to detector without being

affected significantly by collisions with gas phase molecules. Additionally, in general, conducting experiments in UHV helps to achieve longer instrument lifetimes, especially for fragile components such as filaments, channeltrons and channel plates.

The XPS studies reported in this thesis were carried out in a major UHV facility which is composed of four interlinking chambers (Figure 2.9) for sample entry, analysis, sample preparation and high pressure sample treatment. The work described in Chapter 3 particularly used the analysis and preparation chambers. After a full bakeout, the base pressure of each of these two chambers can be maintained below 2×10^{-10} Torr, and it represents an important feature of this facility that samples can be transferred between these two chambers under continuous UHV. The analysis chamber is based around a Leybold MAX200 spectrometer (described below), but it also has an ion gun for sputtering and ion scattering spectroscopy (ISS), an electron gun to enhance Auger spectra and a separate electron flood gun to aid studies on insulating samples. The preparation chamber has an evaporation source for growing thin films, a variable leak valve for introducing gas to the sample and a quadrupole mass spectrometer for detecting residual gas. Samples can be heated by means of radiative heating, and cooled by liquid N_2 in both chambers.

The pumping system used in the XPS facility is shown in Figure 2.10. The chambers are initially rough pumped to the 10^{-3} Torr range by rotary pumps, then pumped to the 10^{-7} Torr range or below by the turbomolecular pumps. The base pressures are achieved after baking at around 130°C for 12 hours or more, followed by the degassing of all filaments. A supplementary ion pump is available for the X-ray source system.
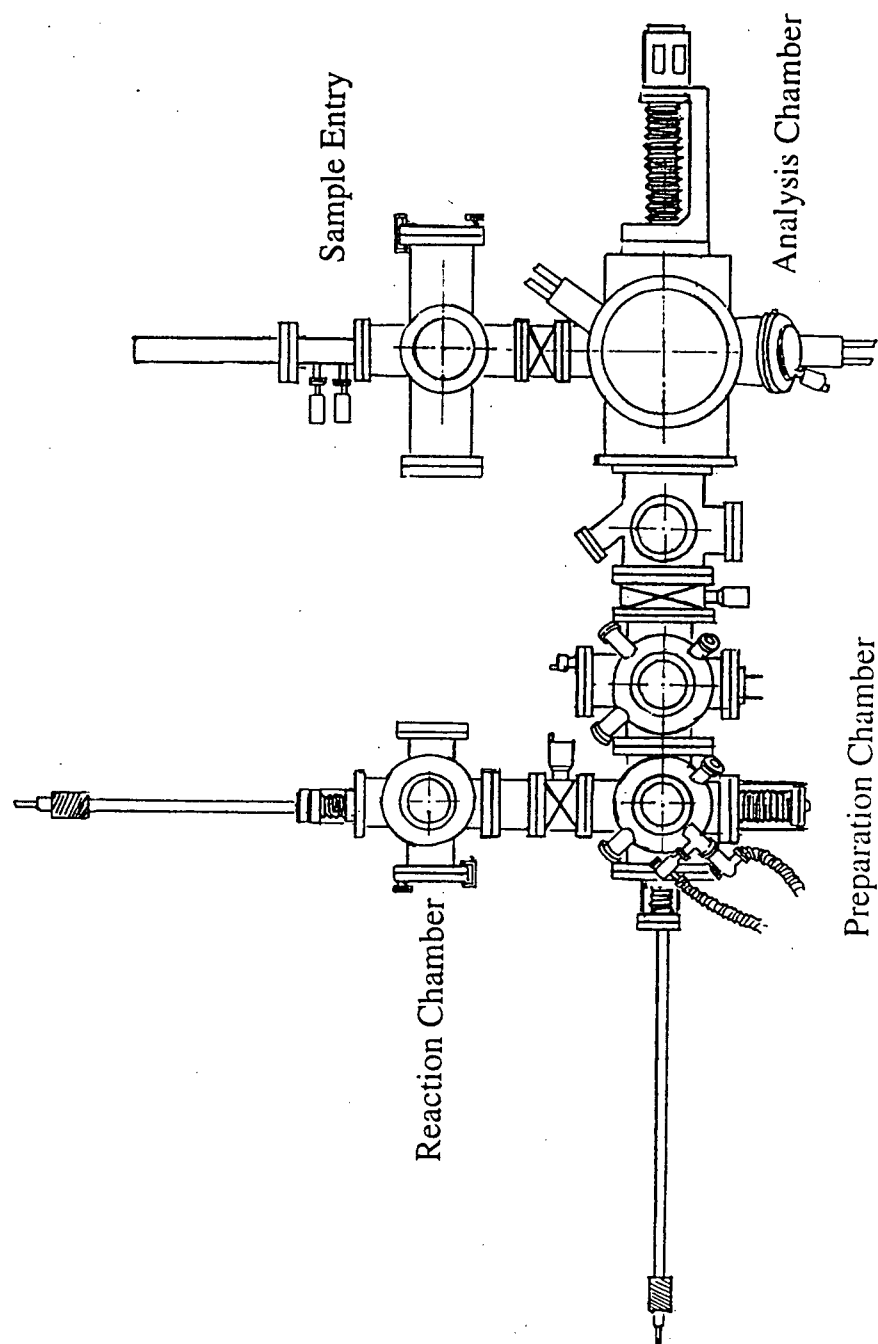
Figure 2.9 Top view of the MAX200 facility.

25
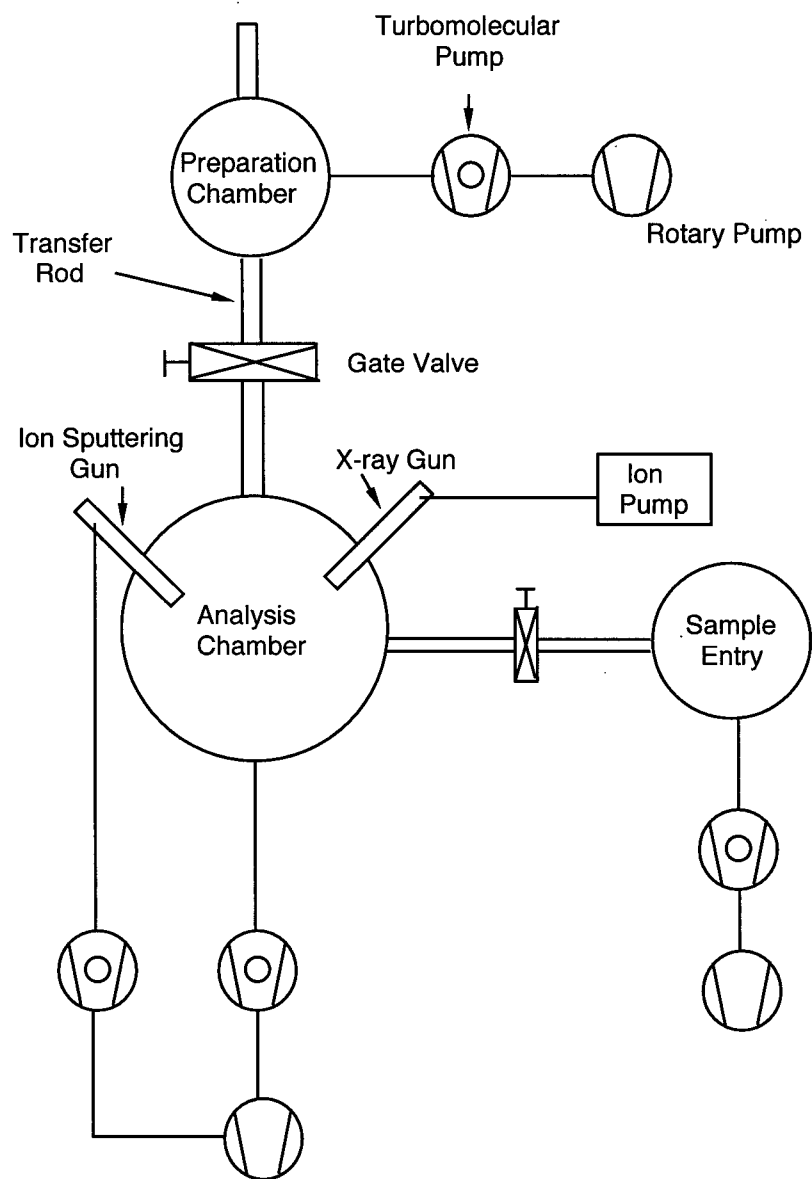
Figure 2.10   Schematic diagram of the pumping configuration for analysis, preparation and sample entry chambers on MAX200 facility.

2.4.2 Spectrometer

Major components of the Leybold MAX200 spectrometer used in this work include a dual anode X-ray source, a five-motion manipulator and a EA 200 hemispherical electrostatic energy analyzer (a separate AlKα monochromator is also available although it was not used in this research). The spectrometer collects data digitally and is interfaced to a HP 1000 based microprocessor. The latter uses Data System DS 100 software for selecting instrumental parameters, and for operations of data acquisition and processing [60]. A sample held on the PTM 60 UHV manipulator can be subjected to x, y, z translations and two rotations (θ and ϕ) under computer control, so that sample analytical positions can be reproducibly recovered after operations during a study (e.g. after sample transfer to the preparation chamber).

X-rays are produced from anodes bombarded by electrons accelerated through about 15 kV after emission from a heated filament. The dual-anode source (schematically indicated in Figure 2.11) in the MAX200 spectrometer provides a choice between the two X-ray lines: MgKα (1253.6 eV) and AlKα (1486.6 eV). It has two filaments and two anode surfaces, one of magnesium and one of aluminum, and switching from one source to the other can be done in a few seconds. The 2 μm thick aluminum foil window is transparent to the photons, and is sufficiently thin that the X-ray flux is not significantly attenuated, but it prevents stray electrons, radiative heating and contamination from the anode region reaching the sample.

Energy analysis is done with the EA 200 hemispherical electrostatic energy analyzer, for which its key components are shown schematically in Figure 2.12. It consists of a vacuum housing and three major internal components: (A) the input lens system for receiving photoelectrons ejected from sample, (B) the 180° hemispherical capacitor with nominal radius

Cooling Water

Focusing Shields

Filament 1

Filament 2

Al Anode

Mg Anode

e⁻

$h\upsilon$

Al Window
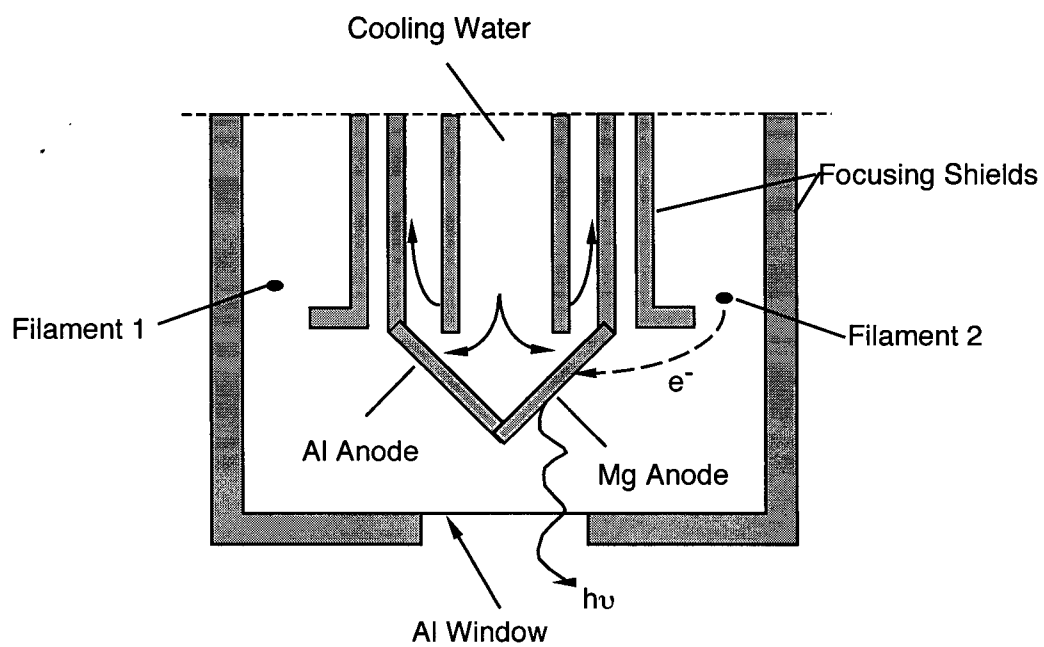
Figure 2.11   Schematic diagram showing a dual-anode X-ray source.
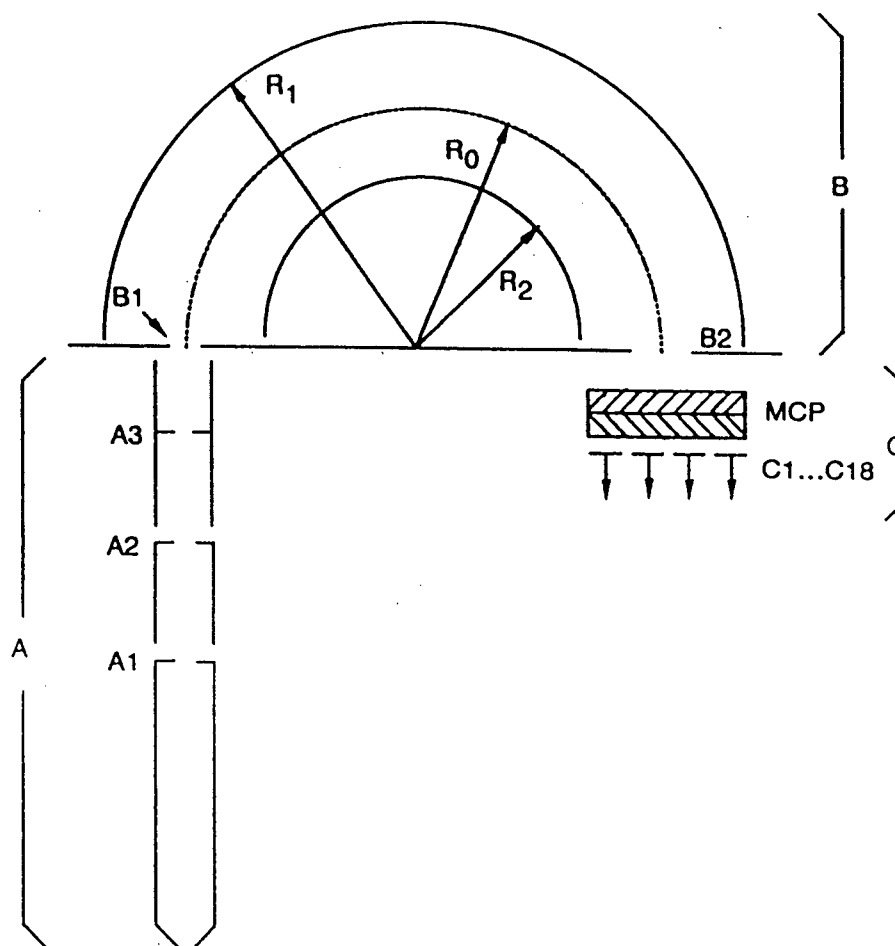
Figure 2.12   EA 200 spectrometer: (A) input lens system (with A1 to A3 apertures), (B) hemispherical capacitor (with outer and inner radii of R_1 and R_2 and nominal capacitor radius of R_0) and (C) detector assembly (C1 to C18 are discreet collectors and MCP is the microchannel plate assembly).

(R_0) of 150 mm for performing electron energy analysis and (C) a multichannel detector with 18 discrete channels capable of count rates above 10^7 s^{-1}.

The input lens system has two stages. The first lens stage (including a variable angular aperture A1 and image aperture A2) defines the analysis area and acceptance angle by imaging the sample onto the image aperture A2; it simultaneously restricts the acceptance angle by the angular aperture A1. Electrons passing through A2 are focused onto the input slit B1 of the hemispherical capacitor by the second lens stage, where they are retarded for subsequent energy analysis in the hemispherical capacitor. In addition the second lens stage defines the capacitor acceptance angles by a fixed aperture A3.

In the hemispherical capacitor a deflecting potential ΔV is applied between the two concentric hemispheres of radii R_1 (190 mm) and R_2 (110 mm). Electrons travel on the central circular trajectory and reach output plane (B2) at the nominal radial position R_0, where $R_0 = (R_1+R_2)/2$ (i.e. 150 mm in the EA 200), provided their kinetic energy E_0 satisfies

$$e\Delta V = E_0 \left(R_1 / R_2 - R_2 / R_1 \right) \tag{2.9}$$

where ΔV is the deflecting potential [71,72]. Electrons with higher kinetic energy are focused further outside R_0 and those with lower energy are focused further inside, on the plane B2. Images of electrons possessing different energies within the capacitor are concentric circles, and the radial image position R for electrons with kinetic energy E_{kin} in the hemispherical capacitor is given, in a first order approximation, by [73]

$$R = R_0 + D(E_0) \times (E_{kin} - E_0) \tag{2.10}$$

with $D(E_0)$ being the hemispherical capacitor dispersion for the selected pass energy, E_0. This offers the possibility for multichannel detection, with simultaneous recording of an energy band around the nominal pass energy, E_0.

If the capacitor is allowed to accept the half angle α in the dispersion direction, then, in a first order approximation, the FWHM (full width at half maximum) of the energy analyzer resolution ΔE_{spec} is [26]

$$\Delta E_{spec} / E_0 = (s_1 + s_2) / 2R_0 + \alpha^2/4 \tag{2.11}$$

where s_1 is the radial width of the input slit at plane B1, s_2 is the radial width of each collector channel at the exit plane B2. Since s_1, s_2, R_0 and α are restricted by the spectrometer construction, the relative resolution of the spectrometer varies with E_0, but a measured line width also has contributions from the inherent line width of the atomic level involved (ΔE_{line}) and from the natural line width of the exciting radiation (ΔE_{source}). The observed line width in a measured spectrum satisfies

$$FWHM_{total} = (\Delta E^2_{source} + \Delta E^2_{analyzer} + \Delta E^2_{line})^{1/2} \tag{2.12}$$

provided all contributions have the Gaussian form [26].

To perform an energy analysis under constant resolution, electrons entering the analyzer are pre-retarded by the lens system to a pass energy E_0. This energy is chosen according to the level of resolution needed. Then the deflecting potential of the analyzer (ΔV) is set according to Eq. (2.9) for that particular pass energy. The actual scanning of the kinetic energies is done by ramping the retarding field voltage during the pre-retardation process. In principle, a lower pass energy gives better analyzer resolution, but the signal intensity drops off rapidly with retardation. Therefore, for each situation, an appropriate pass energy is chosen to give the optimal balance between resolution and intensity. In this work, survey scans used a pass energy 192 eV while the higher resolution spectra used 24 eV.

Signal sensitivity is improved by having an electron multiplying component between the exit plane of the hemispherical capacitor (B2) and the collector electrodes. In the EA 200, a set of two microchannel plates is used in a chevron arrangement (Figure 2.12), and this leads to an amplification in the electron signal by about 10^7. Electrons from the second microchannel plate are postaccelerated onto the nearest collector electrode, and each charge pulse is normalized to the original single electron count. Multichannel detection is performed by appropriately arranging several collector electrodes, in shape similar to the entrance slit B1 and with the centers on concentric circles in the exit plane B2. The radial distance between neighboring collectors is selected according to Eq. (2.10) to meet the requirement of constant kinetic energy difference between neighboring channels. As the kinetic energy of the electrons arriving at each collector is known from Eq. (2.10), the numbers in each channel (with the same kinetic energy), can simply be added up to give a measured spectrum (i.e. total number of electrons for each kinetic energy).

The kinetic energy of a photoelectron measured in the spectrometer (E_k') is referenced to the vacuum level of the spectrometer. In turn the binding energy E_b of the electron in the sample is referenced to the Fermi energy of the sample. For a conducting sample in electrical contact with the spectrometer (equal Fermi energies), Eq. (2.1) needs modification to

$$E_k^{'} = h\nu - E_b - W_{sp}. \tag{2.13}$$

The spectrometer work function, W_{sp}, can be corrected by calibration with standard samples; in general, it remains constant while the spectrometer is held under UHV. Eq. (2.13) therefore enables photoelectron kinetic energies to be converted to binding energies. The spectra shown in this thesis have been calibrated against the gold $4f_{7/2}$ peak, whose binding energy is 84.0 eV.

2.4.3 Data Analysis

Treatments of raw spectra directly from the measurement process are needed before performing a spectral interpretation. First, structure of interest in a spectrum must be background subtracted and there are several methods available [74-77]. Figure 2.13 schematically indicates an example of subtraction using the non-linear approach proposed by Shirley [74]. This method assumes that in a photoelectron peak, which dominantly involves elastically scattered electrons, there are contributions from inelastic processes, and that at any part of the spectral peak, the number of inelastically scattered electrons is proportional to the number of elastically scattered electrons at higher kinetic energies. The subtraction is applied to an energy region of $E_{min} < E < E_{max}$, for which the operator chooses the lower and upper energies. The correction for inelastic contributions is determined by the iterative algorithm:

$$n'_{k+1}(E) = n(E) - n(E_{max}) - S \int_E^{E_{max}} n'_k(E) \, dE \qquad (2.14)$$

where n(E) is the measured count rate and the $n'_k(E)$ identify count rates after subtraction of background contributions (the latter have subscripts, for example 'k' indicates the background corrected value according to the kth iteration). The reference background level is provided by $n(E_{max})$; S is a constant which is fixed by the requirement that $n'_k(E_{min}) = 0$. The process starts with $n'_1(E) = 0$ and continues until $n'_{k+1} \sim n'_k$; it normally converges after three or four iterations. After subtracting background, the peak area associated with the elastically scattered contributions can be determined by integration.

As noted in Section 2.3.1, a particular high-resolution spectrum may contain overlapping contributions from different chemical states for the same atom. Then curve synthesis is required to identify individual components. To do this one needs to select functions that can represent the
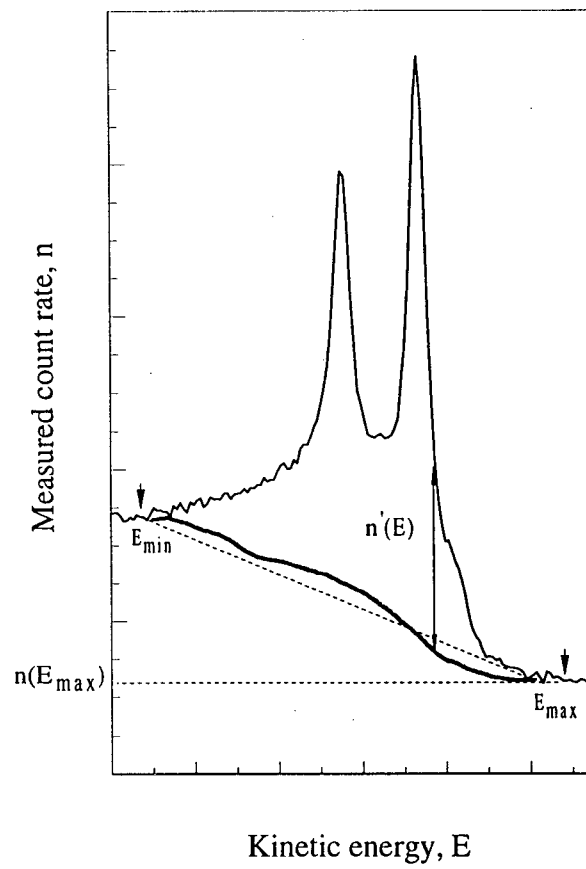
Figure 2.13   Notation for non-linear background subtraction, method proposed by Shirley.

component profiles; the objective is to find the combination of component functions that sum to give a close representation of the background-corrected experimental spectrum. The individual component functions are fixed by functional form, as well as by variables such as position, intensity and width. The most effective approach is to use the mixed Gaussian/Lorentzian form as a function of energy [26]:

$$f(E) = \text{peak height} / [1 + M(E-E_o)^2/\beta^2] \exp\{(1-M) [\ln 2(E-E_o)^2]/\beta^2\} \tag{2.15}$$

where E_0 is the individual component peak energy, the parameter β fixes the FWHM, and M is a mixing ratio (1 for pure Lorentzian; 0 for pure Gaussian).

Functions of the type in Eq. (2.15) are used for the individual components in the curve synthesis process as carried out by the DS 100 software in the MAX200 system. A relatively simple example of the curve synthesis process is illustrated in Figure 2.14 for a Zr 3d spectrum from an oxidized thin film of zirconium. Two dominant peaks are apparent, consistently with the 3/2, 5/2 doublet, but closer scrutiny of the right hand peak suggests there are two overlapping components: one gives the main peak at 182.9 eV and the other the shoulder at about 181.0 eV. Two doublets are therefore assigned for this spectrum with parameters that are varied to optimize the fit to the experimental curve. The components in each doublet maintain the required $3d_{3/2}$ to $3d_{5/2}$ area ratio of 2 to 3, and the spin-orbit splitting is fixed at 2.4 eV. The curve synthesis is done iteratively by optimizing the fit between the measured curve (after background subtraction), and the sum of the optimized component functions. The latter is done by least-squares fitting; the quality of fit is evaluated by the function:

$$\chi = \left[\frac{1}{N_{free}} \sum_{i=1}^{N} \frac{(Y_{mea,i} - Y_{fit,i})^2}{Y_{mea,i}} \right]^{\frac{1}{2}} \tag{2.16}$$
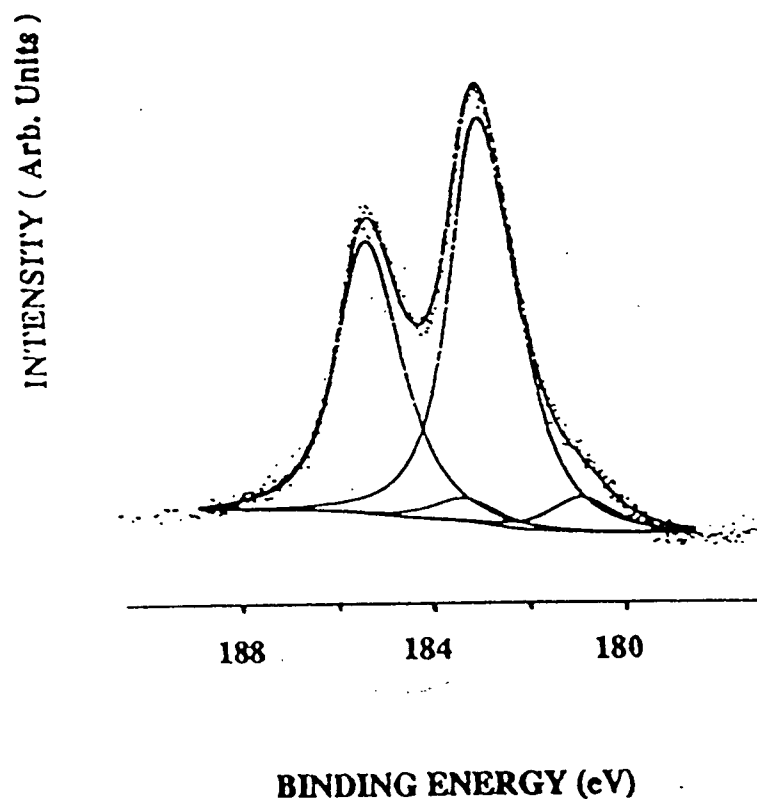
Figure 2.14   High resolution scan of Zr 3d photoelectron peak from an oxidized zirconium film.

where the sum is over the N data points in the spectral region to be fitted. In Eq. (2.16), $Y_{mea,i}$ is the measured count rate at the ith data point, $Y_{fit,i}$ is the corresponding value in the fitted envelope, and N_{free} equals $N - N_{fit}$ (N_{fit} is the number of parameters to be fitted). Parameters in the curve analysis are varied by the conditions that the χ value is minimized, and that visual comparison indicates a close agreement between the simulated and measured spectra. If a given number of functions of the type in Eq. (2.15) cannot converge to a reasonable correspondence, more functions can be added; however this must be done according to basic physical and chemical principles.

Chapter 3: XPS Studies of Thin Films of Oxidized Zirconium

3.1. Introduction

The oxidation of zirconium surfaces has importance in relation to nuclear technology, as noted in Chapter 1. A particular aspect of this subject concerns the chemistry applying within the region of the oxide-metal interface, where a range of oxidation states may be present. Information on how this region is affected by reactive gases is extremely limited. In this chapter, we report a new direction for investigating the stability and reactivity of the oxide-zirconium interface in oxidizing and hydriding environments. The studies were carried out over a range of temperature including 300°C, the operating temperature of the CANDU reactor [78,79].

The use of electron spectroscopic techniques to probe the chemistry of oxidized zirconium can be affected by surface charging, and by oxygen diffusion into the bulk metal at temperatures above 230°C [16,17]. To overcome these problems, we used the approach of studying thin films of oxidized zirconium grown on a gold substrate. This has several advantages. First the insulating properties are suppressed so that the charging problem can be avoided. Second, the inert substrate helps to ensure that the oxygen stays with the zirconium in the film even at elevated temperatures. Third, since the total amount of zirconium present is restricted (unlike the situation with a bulk sample), this allows wider-ranging control of the amount of oxygen in the sample in relation to the amount of zirconium. Compared with other noble metals, gold appears suitable as the substrate for this work since the intermixing between Zr and Au is relatively less prominent [80,81]. As well, the Au $4f_{7/2}$ line provides a convenient reference for calibrating other photoemission lines (cf. Section 2.4.2) throughout the study.

3.2. Experimental

All experiments were carried out in the UHV facility, which is composed of an analysis chamber, a preparation chamber and a transfer chamber, as described in Section 2.4.1. Thin films of oxidized zirconium were prepared in the preparation chamber. The effective base pressure of this chamber was 6×10^{-10} Torr with water as the dominant component in the ambient gas, a feature that was deliberately built into the experimental design by not completely baking the preparation chamber. The resulting ambient enabled a zirconium oxide film to be formed by depositing zirconium sufficiently slowly on to the gold substrate. This is consistent with earlier observations using secondary ion mass spectrometry (SIMS) that when zirconium is exposed to H_2O in the 10^{-8}-10^{-9} Torr range, the main product is the metal oxide rather than the hydride [82]. The gold foil was cleaned prior to zirconium deposition by repeated cycles of Ar^+ sputtering (2.5 kV, 10 mA) and annealing (500°C, 20 minutes) until no impurities could be detected by XPS. Figure 3.1 shows schematically the zirconium evaporation source used in this work. It contained a pair of copper electrodes covered by a protective quartz tube. Tungsten wire (99.98%, diameter 0.5 mm) co-wrapped with thin Zr wire (99.9%, diameter 0.01 mm) was coiled to form the filament, and mounted across the electrodes through which AC power was applied to the filament; the evaporation rate could be controlled by changing the voltage. The melted zirconium coated the tungsten filament evenly and provided a stable evaporation rate. To minimize contamination in the deposited film, the source was initially outgassed for about 40 hours at slightly below the operating temperature. For most studies discussed, the source operated at about 1700°C and produced approximately 1 Å per minute. For these operating conditions, the pressure in the preparation chamber increased to around 5×10^{-9} Torr, but the
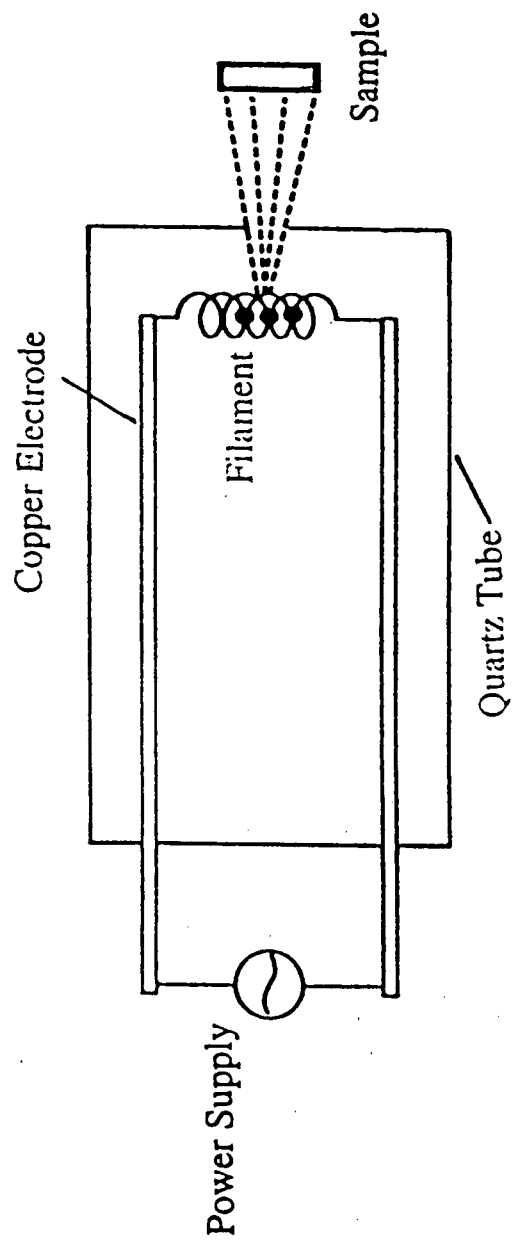
Figure 3.1   Schematic diagram of the zirconium evaporation source.

quadrupole mass spectrometer showed that water was still the dominant component. After preparation, a sample could be heated and exposed to gases introduced through the leak valve into the preparation chamber. At each appropriate point in the preparation procedure, the sample could be transferred under continuous UHV to the analysis chamber for detailed determination. From this initial sample, a series of successive treatments were made, as detailed in Table 3.1, and the designations A1 to A6 define the various sample surfaces studied by XPS.

For XPS measurements, the MgKα excitation source was operated at 15 kV and 20 mA, and the emitted photoelectrons were collected from a 2×4 mm^2 area. At each stage of the study, high-resolution narrow-scan spectra were measured for the Zr 3d, O 1s and Au 4f core levels at a 24 eV pass energy. Core binding energies were referenced to the Au 4f$_{7/2}$ peak at 84.0 eV. Angle-dependent spectra were obtained by varying the angle (θ) between the plane of the sample surface and the axis of the detector. Throughout, after operations of sample treatment and transfer, samples were assessed to ensure that the results below were not artefacts introduced by contamination (checked by XPS) or any charging effect (checked by the bias potential technique described by Leung *et al.* [83]).

3.3. Results

3.3.1 Characterization of Freshly Deposited Film

Figure 3.2 shows Zr 3d and Au 4f$_{7/2}$ photoelectron spectra measured at θ = 90° and 30° from the freshly deposited film. The deposition was done for 30 minutes with the source operating at about 1700°C. More than one chemical state is indicated for both Zr and Au, and the curve synthesis followed the procedures described in Section 2.5. The Zr 3d spectra were interpreted with three doublets, and the following discussion notes in particular the 3d$_{5/2}$

Table 3.1 Successive sample treatments used in this work.

Designation	Preparation treatment
A1	Zirconium was deposited at 5×10^{-9} Torr (ambient dominantly H_2O) for 30 min onto clean Au foil to give the initial oxidized film
A2	Heat sample A1 to 250°C for 5 min with ambient H_2O at about 1×10^{-9} Torr, and then to 320°C for a further 2 min.
A3	Expose sample A2 at 300°C to O_2 at 4×10^{-7} Torr for 10 min
A4	Heat sample A3 in low 10^{-9} Torr H_2O atmosphere at 300°C for 30 min, and then at 400°C for another 30 min.
A5	Expose sample A4 at 300°C to D_2 at 4×10^{-7} Torr for 1 hr
A6	Heat sample A5 at 500°C (effectively in low 10^{-9} Torr H_2O atmosphere) for 5 min
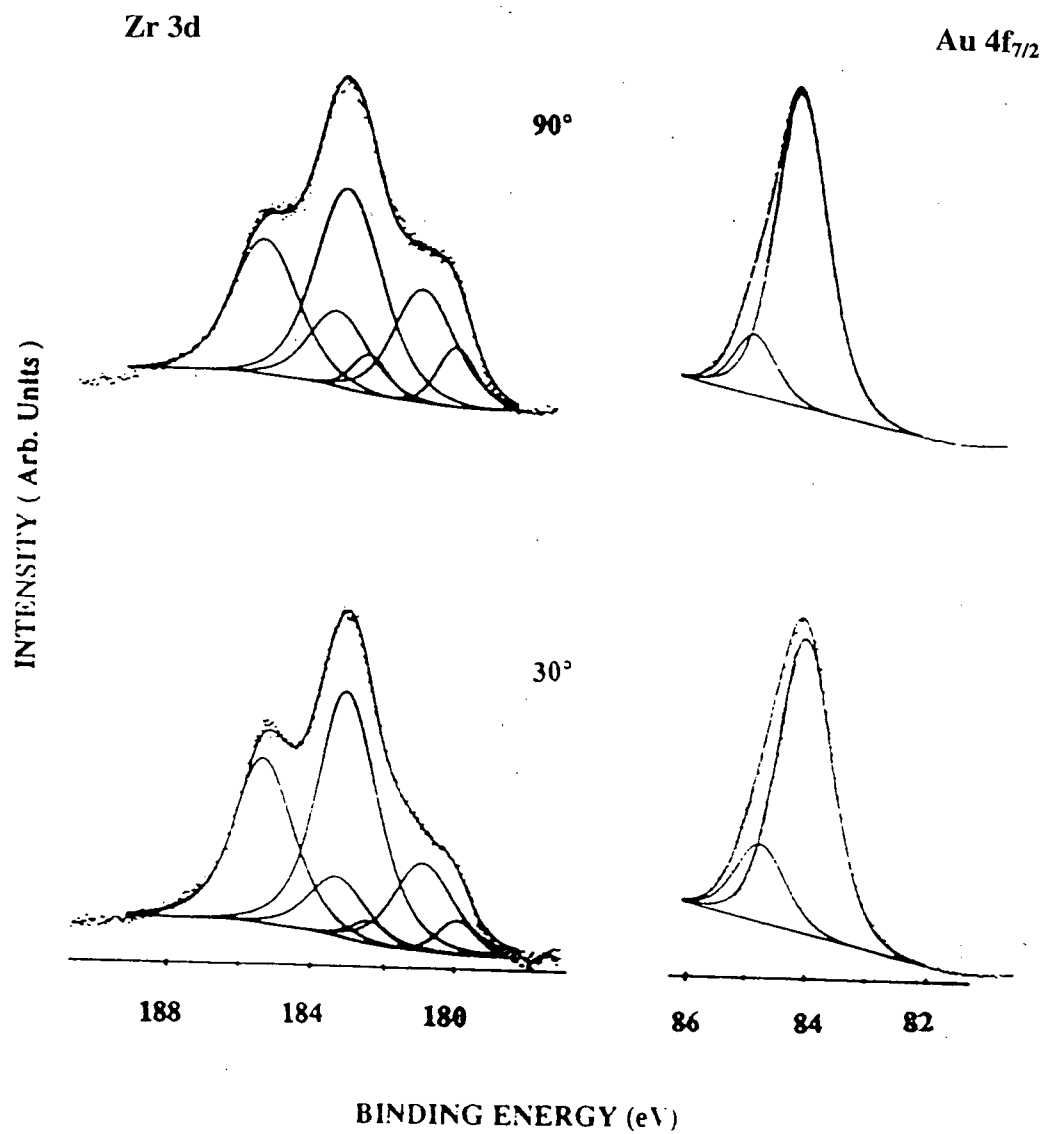
Figure 3.2   Zr 3d and Au 4f$_{7/2}$ spectra for take-off angles equal to 90° and 30° for the freshly deposited oxide film as in sample A1.

components. The component at 182.9 eV is assigned to ZrO_2. This binding energy agrees closely with that reported by Maurice *et al.* [84]; the latter authors studied the oxidation of a very thin film of zirconium and they had direct structural evidence for the formation of ZrO_2. The component at 180.8 eV is assigned to a lower oxidation state material, ZrO_x (where x is intermediate between 0 and 2), which has also been proposed previously [4,6,7]. The third component at 179.9 eV has a shift of 1.2 eV from the metallic Zr 3d core level (178.7 eV [4]). The Au $4f_{7/2}$ spectra show two components; that with binding energy 84.0 eV is the regular gold reference, while the other component is shifted to higher binding energy by 0.7 eV.

The area of the Zr $3d_{5/2}$ peak at 179.9 eV decreased progressively upon annealing in a background of around 1×10^{-9} Torr H_2O (to form sample stage A2), and this peak could no longer be detected after the sample was heated in an atmosphere of O_2 at 4×10^{-7} Torr (to form sample stage A3). A corresponding behavior was observed for the higher binding energy component of the Au $4f_{7/2}$ peak. The intensity ratio of these two components (Zr $3d_{5/2}$ at 179.9 eV and Au $4f_{7/2}$ at 84.7 eV) remained constant during the heating process. These observations suggest that these two components originate from a Zr-Au alloy. It is noted that the magnitudes of the binding energy shifts (compared to values for the pure metals) found here are comparable to values measured in known alloy systems, for example the Zr 3d shifts of 1.14 and 0.85 eV reported for Zr-Pd and Zr-Cu alloys, respectively [85]. Moreover, calculations of binding energy shifts, using the method of Mårtensson *et al.* [86,87], predict shifts of 1.30 and 0.81 eV for Zr 3d and Au 4f, respectively, which are reasonably close to the values 1.2 and 0.7 eV observed here. The full width at half maximum (FWHM) for the shifted component (1.4 eV) in the Zr 3d spectrum is less than those for the oxide components (1.9-2.0 eV), and essentially equals that for the pure metal. Taking all these factors together, we believe that the Zr $3d_{5/2}$ peak at 179.9 eV and the Au

$4f_{7/2}$ peak at 84.7 eV arise from a Zr-Au alloy phase in the interface region. Other examples of intermetallic compound formation at zirconium interfaces include those observed in the Zr/W(100) and Zr/Pt(100) systems [88,89]. Table 3.2 summarizes the binding energies and FWHM values used for the components in the decomposition of the measured spectra, and Table 3.3 reports ratios of component areas with varying take-off angle, θ. The ratio of the ZrO_2 component to each of the Au, ZrO_x and Zr-Au alloy components increases quite markedly with decreasing θ, and this is consistent with the ZrO_2 being located in the outermost region of the film. The ratios of ZrO_x and Zr-Au alloy to Au increase more slowly with increasing surface sensitivity, and generally the trends for ZrO_x and Zr-Au alloy with changing θ are similar (see the relatively constant I_{ZrO_x} to I_{Zr-Au} ratio in Table 3.3). We therefore propose that between the ZrO_2 and Au substrate there are regions of ZrO_x and Zr-Au alloy, as illustrated schematically in Figure 3.3. The thickness of the film was estimated to be about 20 Å. This was done by following the attenuation of the Au 4f component (procedure indicated in Section 2.3.3) and assuming a mean free path of 24 Å in ZrO_2 [49].

3.3.2 Stability of Film in Different Environments

Sample A1 was annealed in an environment which was dominantly water at about 1×10^{-9} Torr. The initial heating was for 5 minutes at 250 °C, and then the sample was heated for a further 2 minutes at 320 °C (to give sample stage A2). Figure 3.4 (b) includes Zr 3d and Au $4f_{7/2}$ spectra for normal emission after this annealing, and Table 3.4 summarizes composition ratios, and the relative amounts of Zr in the different compound forms, after the different treatments. The relative elemental amounts were determined from the peak areas in high-resolution spectra

Table 3.2   Binding energies and FWHM values (in eV) used to decompose the Zr 3d and Au $4f_{7/2}$ spectra for sample A1.

Component	Zr			Component	Au	
	$3d_{5/2}$	$3d_{3/2}$	FWHM		$4f_{7/2}$	FWHM
Zr-Au alloy	179.9	182.3	1.4	Zr-Au alloy	84.7	1.0
ZrO_x	180.8	183.2	1.9	Bulk Au	84.0	1.0
ZrO_2	182.9	185.3	2.0			

Table 3.3   Ratios of intensities of different components in Zr 3d spectra for sample A1 at different take-off angles, θ

θ (deg)	I_{ZrO_2} / I_{Au}	I_{ZrO_2} / I_{ZrO_x}	I_{ZrO_2} / I_{Zr-Au}	I_{ZrO_x} / I_{Zr-Au}
90	0.5	2.0	6.3	3.1
60	0.9	2.9	9.7	3.4
45	1.1	3.2	11.2	3.5
30	1.4	3.6	12.3	3.4
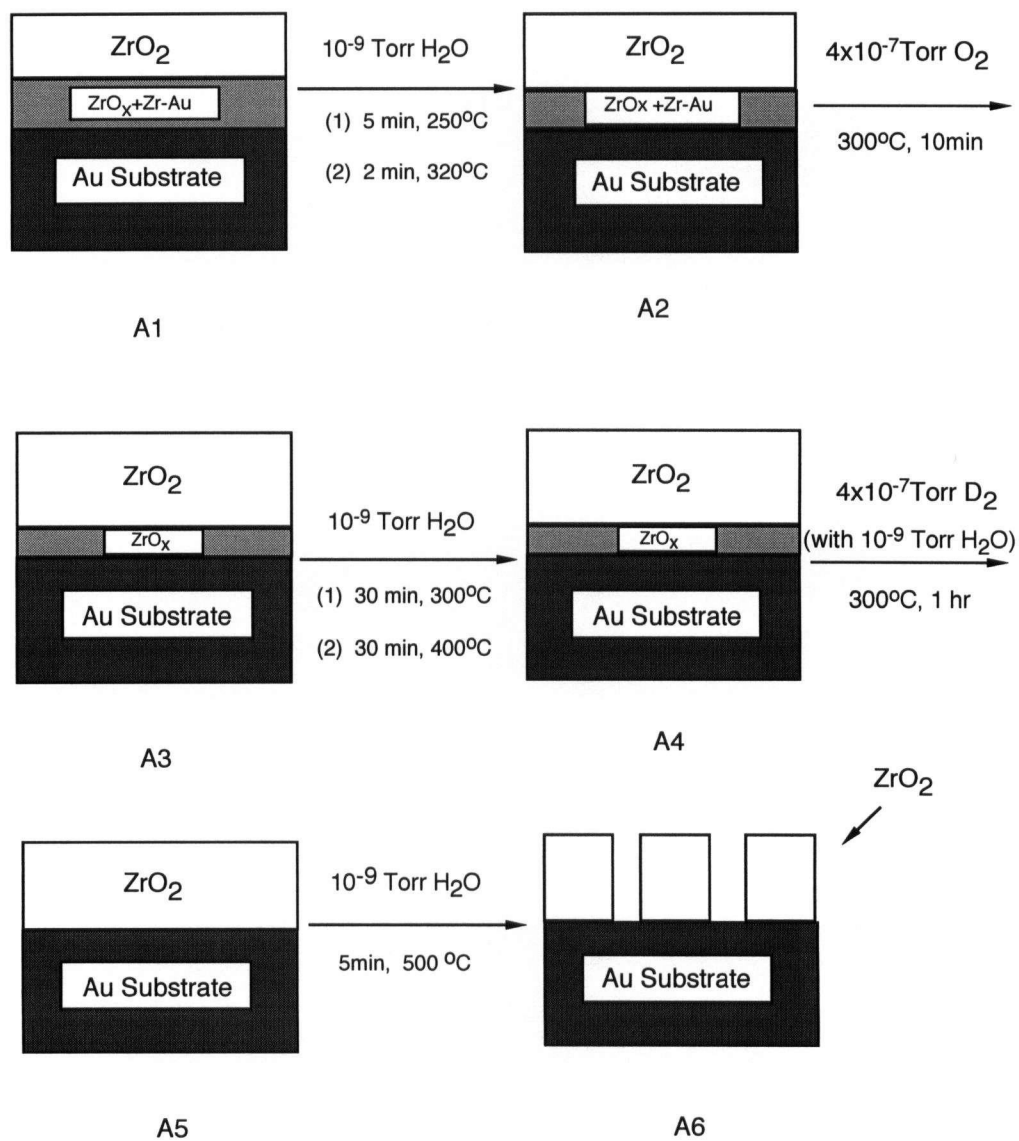
Figure 3.3 Changes in the film composition indicated by XPS following the sequential treatments specified in Table 3.1.
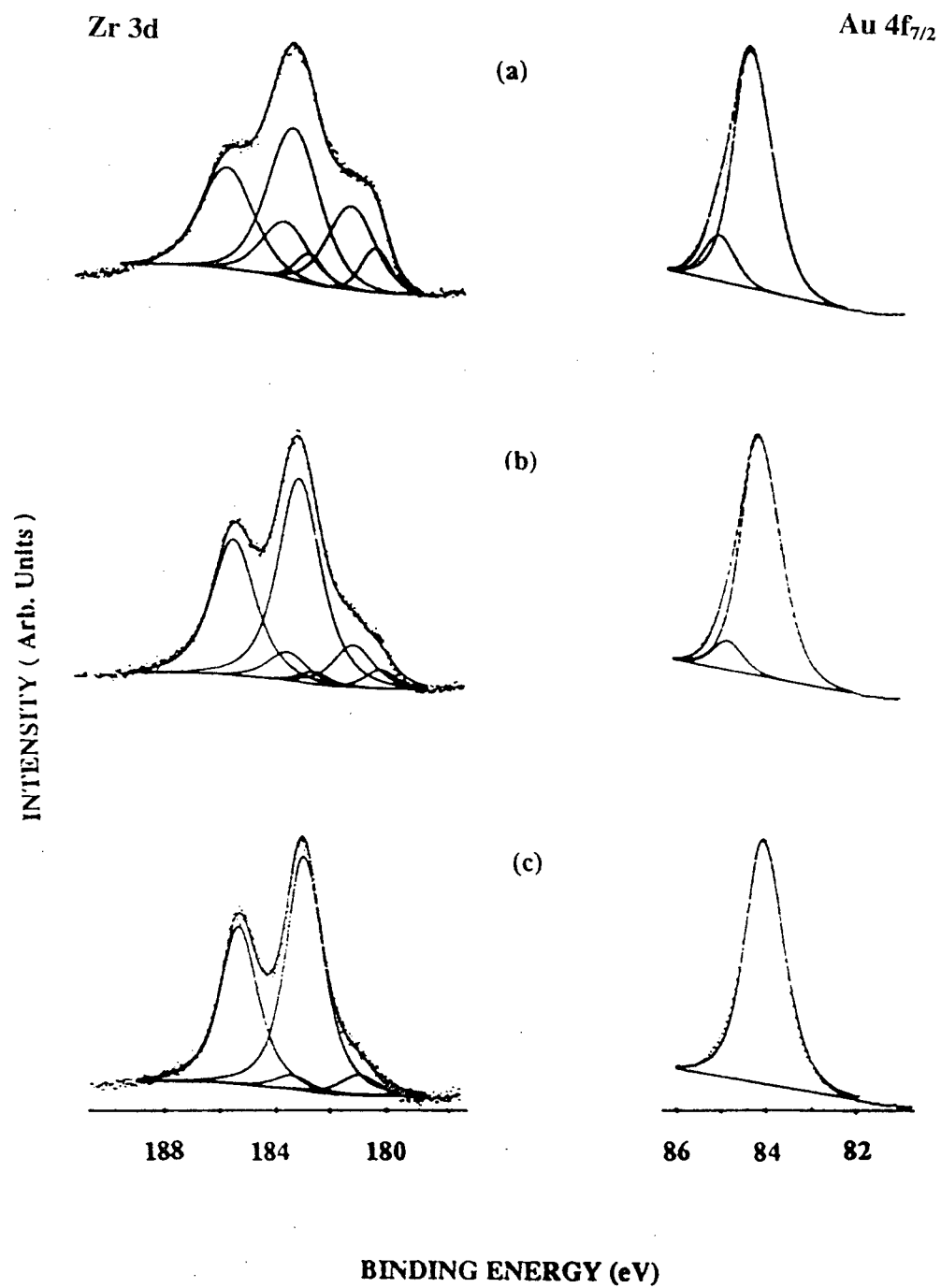
Figure 3.4   Zr 3d and Au 4f$_{7/2}$ spectra measured for samples: (a) A1 (as deposited), (b) A2 (after annealing in 10^{-9} Torr H$_2$O) and (c) A3 (after heating in 4×10^{-7} Torr O$_2$ for 10 min).

Table 3.4   Atomic composition ratios for the oxidized Zr film as initially formed and after annealing treatments in about 1×10^{-9} Torr H_2O.

State	O/Au	O/Zr_t	ZrO_2/Zr_t	ZrO_x/Zr_t	$Zr-Au/Zr_t$
Initial (A1)	1.2	1.1	0.60	0.30	0.10
5 min at 250°C	1.7	1.6	0.75	0.16	0.08
2 min at 320°C[*]	1.8	1.7	0.79	0.15	0.08

Zr_t refers to the total Zr content, i.e. sum of ZrO_2, ZrO_x and Zr-Au alloy components.

* Corresponds to formation of sample A2.

after correcting for background and atomic sensitivity factors. As the temperature is raised, the ZrO_x and Zr-Au alloy components decreased while the amount of ZrO_2 increased, with a net increase in O. It is clear for these conditions of sample and annealing, that ambient H_2O at around 1×10^{-9} Torr is able to promote the oxidation of both ZrO_x and the Zr in alloy form.

Sample A2 was then further heated to 300°C for 10 minutes in 4×10^{-7} Torr O_2 (to give sample stage A3). Changes in the Zr 3d and Au $4f_{7/2}$ spectra are shown in Figure 3.4 (c). Components associated with the Zr-Au alloy phase were no longer identifiable in the spectra. The amount of ZrO_x decreased, but both the O-to-Zr and O-to-Au ratios increased. When this resulting sample (A3) was annealed at 300°C in a low 10^{-9} Torr H_2O atmosphere for 30 minutes, and then at 400°C for 30 minutes (to form sample stage A4), no further changes were detected by XPS. At this stage it appears that the outer layer of ZrO_2 is sufficiently thick to slow oxidation of the underlying structure by the low-pressure H_2O.

Sample A4 was exposed to 4×10^{-7} Torr D_2 at 300°C for 1 hour (to give sample stage A5). Figure 3.5 compares the Zr 3d spectra before and after this treatment. Surprisingly, this treatment results in removal of the ZrO_x component; also the resulting spectrum (with $3d_{5/2}$ and $3d_{3/2}$ components at 182.9 and 185.3 eV, respectively, and relative intensities in the ratio 3 to 2) is characteristic of ZrO_2. This treatment gives small increases in the O-to-Au and O-to-Zr ratios. Prior to the D_2 exposure, no change was detected in the film on heating in the oxidizing atmosphere for 1 hour. Therefore it appears that, at this stage, the further oxidation of the inner region of the film is very slow. However, exposure to D_2 for 1 hour results in the complete conversion of ZrO_x to ZrO_2. Since during this exposure there is still H_2O in the chamber in the low 10^{-9} Torr range, the net increase in O is presumably supplied from this source. Water at the same basic pressure was also present during the heating that converted sample A3 to sample A4,
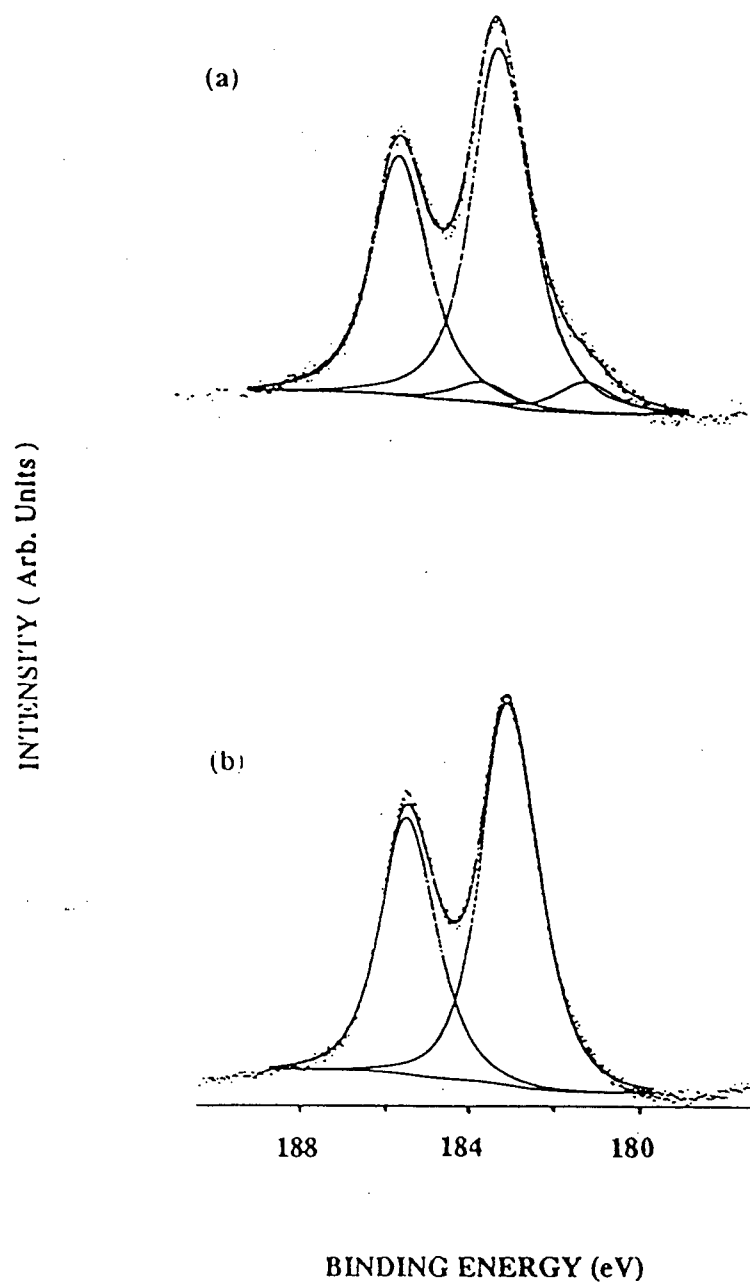
Figure 3.5   Zr 3d spectra for oxidized zirconium film samples: (a) A4 (before D_2 exposure) and (b) A5 (after annealing at 300°C for 1 hr in 4×10^{-7} Torr D_2).

but since XPS did not detect changes for that process, it must be concluded that the D_2 effectively predisposes the film to the further oxidation seen in the spectrum for sample A5.

Sample A5 was annealed at 500°C in UHV (i.e. effectively in an atmosphere of H_2O in the low 10^{-9} Torr range) for 5 minutes to form sample A6. This resulted in an increase in the Au 4f intensity, although with no evidence in either the Au 4f or Zr 3d spectra for the formation of the Zr-Au alloy phase. In an earlier study, in which ZrO_2 was grown on a Au(111) single-crystal surface [90], it was observed that the Au Auger signal increased with heating temperature over the range from 400 to 850°C. Two possibilities were proposed, namely either Au migrates upwards to form intermetallic Zr-Au in an interface region, or the ZrO_2 layer agglomerates. The observation here suggests the latter gives a more reasonable explanation for these conditions. This points to an advantage for using Au as the substrate material since the mixing of ZrO_2 and Au is not pronounced for temperatures 500°C or below.

3.3.3 Other Observations

A parallel study was made on another sample (B1 in Figure 3.6) prepared at a higher deposition rate (about 2 Åmin^{-1}), but otherwise for conditions similar to those specified in Table 3.1 for the formation of sample A1. For B1, XPS indicated the presence of metallic Zr in addition to other components identified in the first film (sample A1). However, when sample B1 was heated to 400°C for 20 minutes in an atmosphere of H_2O in the low 10^{-9} Torr range (to form sample B2), the metallic Zr component was no longer identifiable in the XPS spectrum. This heating resulted in increases in the O-to-Zr_t (here Zr_t refers to the total peak area of Zr 3d peak) and ZrO_x-to-Zr_t ratios, but to decreases in the Zr_t-to-Au and O-to-Au ratios. It was concluded that as a result of this heating some metallic Zr in sample B1 was converted to ZrO_x, while the
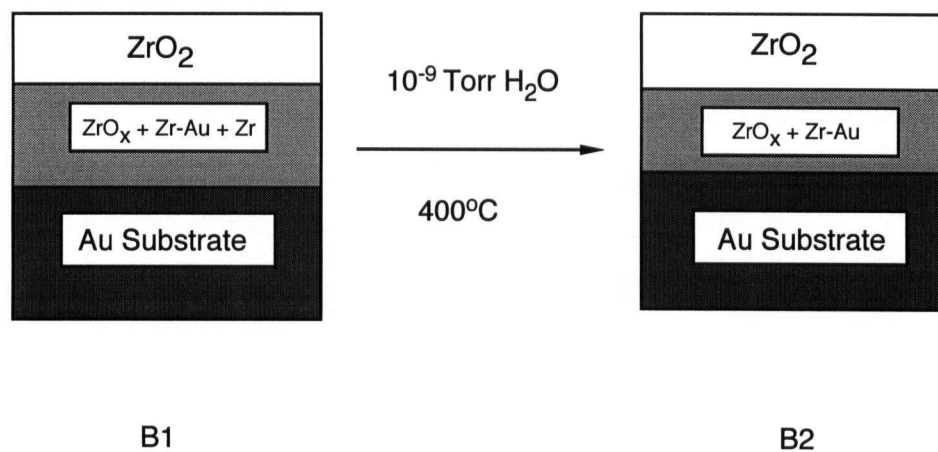
Figure 3.6 Changes in the film composition indicated by XPS for film B1 to give sample B2.

rest was converted to Zr-Au alloy. At sample stage B2, the composition and morphology of the oxidized Zr film was basically the same as those found for sample A1, although film B2 was slightly thicker (about 30 Å). When sample B2 was subjected to further changes, similar to those reported in Table 3.1 starting from A1, very similar behaviors were observed for the ZrO_2, ZrO_x and Zr-Au alloy regions as for the first film. The initial results appear reproducible, but because some variables (e.g. temperature) did not fully correspond to those of the first study (Table 3.1), a further more systematic study was made in subsequent work [91,92]. All other studies found evidence for the H 'catalytic' effect observed here, and so we believe that the H effect identified first in this work is not an artefact.

3.4 Discussion

Changes in the structure and composition of the oxidized zirconium film during the successive sample treatments (A1 to A6) are summarized schematically in Figure 3.3 and some points of interest are noted as follows:

(1) The initial films (sample stages A1 and A2) have an outermost layer of ZrO_2 on top of a lower oxide, ZrO_x, and some Zr-Au alloy.

(2) The $ZrO_2/ZrO_x/Zr$-Au film in sample A2 can be further oxidized by either H_2O or O_2 at 300°C, although this process is hindered as the ZrO_2 layer gets thicker.

(3) While treatment of the film at 300°C by O_2 at 4×10^{-7} Torr (with H_2O in the low 10^{-9} Torr range) does not convert all of the zirconium into ZrO_2, a further heating with D_2 at 4×10^{-7} Torr in the presence of H_2O (again low 10^{-9} Torr range) can activate the oxidation process sufficiently to convert all Zr to the +4 oxidation state.

It is clear that the reaction that dominates in the synthesis of the oxidized zirconium films involves the formation of ZrO_2 from Zr and H_2O, a process driven by the highly negative free energy of formation for ZrO_2. If the initial zirconium deposition rate were sufficiently slow, compared with the impact rate for the H_2O pressure, the whole sample product may be ZrO_2 according to an equation like

$$Zr + 2\,H_2O \rightarrow ZrO_2 + 2H_2 \,. \tag{3.1}$$

However, for sample A1, the oxidation was not complete since the deposited film had O deficient regions (as indicated by the presence of lower oxide ZrO_x), while for B1 (with a faster Zr deposition rate), regions of metallic Zr remain in addition to the ZrO_2 and ZrO_x regions. Evidence here shows that, although reaction of oxygen with zirconium dominates, once all the O is bound, excess Zr may bind to Au depending on the circumstances. The latter process is also driven by an exothermic heat of formation [80], although limits are set by conditions for intermetallic migration. For the formation of sample B1, it appears that the zirconium layer builds up faster than intermetallic migration occurs so that a pure metallic region can be identified in the deposited film.

Molecular dissociation is often believed to occur on oxide surfaces, especially at atomic steps and other defects [93], and the research described here helps to supplement the relatively limited knowledge currently available for the interaction of H_2O, O_2 and D_2 with ZrO_2 surfaces. Molecular dissociation of H_2O on the oxidized surfaces provides oxidant that can migrate from an adsorbed layer into the bulk, for example by a cascade-type process illustrated in Figure 3.7. Such a model helps account for the observation that, on heating freshly prepared oxide film in around 1×10^{-9} Torr of H_2O, the outermost ZrO_2 region increases while the inner ZrO_x and Zr-Au
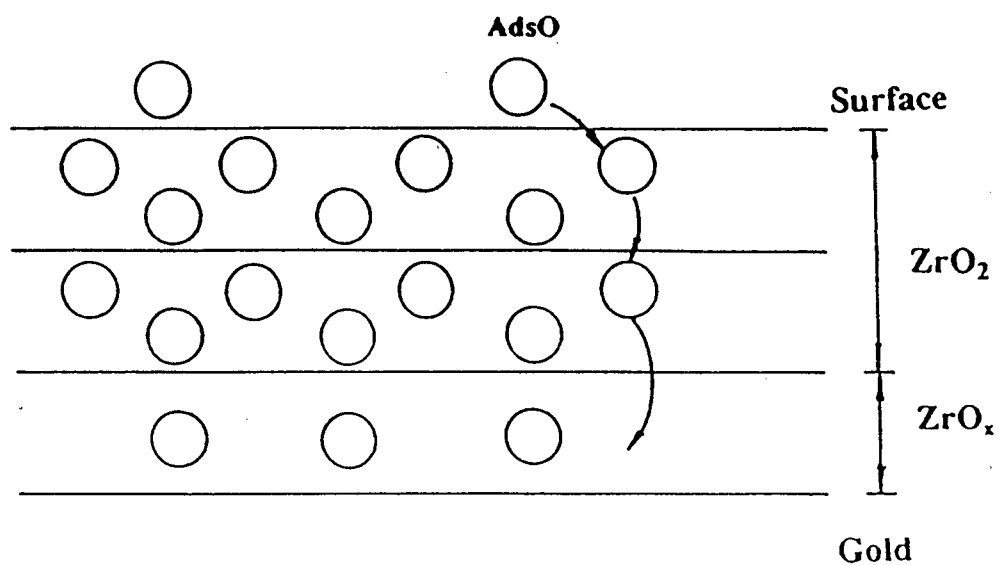
Figure 3.7   Schematic diagram of O incorporation into a thin film of oxidized zirconium grown
on a gold substrate. For convenience of presentation the horizontal lines represent
layers of Zr atoms and the open circles represent O atoms.

alloy regions decrease. Heating in O_2 can continue this process until all the Zr-Au alloy is converted to oxidized zirconium and gold.

Oxidation rates for some transition metals, such as zirconium, depend on the rate of O transport through the oxide films [94]. Since oxygen diffusion is slower in ZrO_2 than in the zirconium suboxide [95], the migration of O from above to the inner region of the film occurs significantly only to a limiting thickness of the ZrO_2 layer so that the oxidation process is hindered as the ZrO_2 layer gets thicker. However, that material does change in the presence of D_2 at 300°C, suggesting that deuterium can facilitate (or catalyze) the oxidation process at the oxide interface to convert all zirconium to the +4 oxidation state. The D atom, with its small size, can occupy interstitial sites or as a deuteron effect some substitution of O^{2-} by OD^-, or even D_2O, in the metal oxide. The "substitutional hydroxide" is likely to reduce the effective oxygen radius and thereby make it easier for migration in the oxide [42,94,96,97]. Possibly this indicates a sense in which D_2 can facilitate further incorporation of O from above. Although this suggests an explanation of the effect of D atoms on the ZrO_2/ZrO_x system, more mechanistic information is required to put the proposal on a firmer basis.

Chapter 4: Low Energy Electron Diffraction (LEED)

4.1 General Principles

Structure is particularly fundamental to determining other physical and chemical properties, and this is true in surface science as in other areas of chemical physics. The potential of LEED to probe atomic arrangements at single crystal surfaces was first realized in 1927 by Davisson and Germer [98], when they discovered the phenomenon of electron diffraction. Much subsequent work, particularly in the past 25 years, has been done to develop the experimental techniques and to establish the theory. Today, LEED is the most developed method to give surface structure information [29], but other techniques are available including surface X-ray diffraction [99], ion scattering [55,100], scanning tunneling microscopy [101], surface-extended X-ray absorption fine structure [102] and photoelectron diffraction [67,69]. The recent development of tensor LEED [103] is opening applications to more challenging surfaces, and the existence of detailed structural information from LEED and the other techniques, is providing a basis for development of the principles of structural chemistry.

4.1.1 Introduction

The experiment of LEED involves directing a beam of electrons of well defined energy on to a well-characterized single crystal surface, and observing the elastically backscattered diffracted beams. For the typical energy range of 30 to 300 eV, the electron wavelength can be expressed as

$$\lambda \, (\text{Å}) = \sqrt{\frac{150.4}{E(eV)}} \tag{4.1}$$

from the de Broglie relation. Diffraction can occur for these energies since the wavelengths (2 - 0.7 Å) are comparable with lattice spacings. Furthermore, electrons in this energy range have a high probability to experience inelastic scattering in a solid. According to Figure 2.2, the associated inelastic mean free paths are typically around 5 to 15 Å; this range corresponds to a probing depth of just a few atomic layers and in turn this makes LEED a surface sensitive technique.

Another important feature of the LEED process is its multiple-scattering nature. Electrons in the low-energy range also experience strong elastic scattering with the target material; their scattering cross sections are around 10^6 times larger than those for X-rays. Indeed, the scattering cross-section of an atom as seen by a LEED electron is of the order of its physical cross-sectional area. As a result, electrons have a high probability to be scattered more than *once* in the solid before they can exit. Forward scattering is more probable than back scattering and, with strong inelastic scattering, this ensures that only a small fraction (e.g. 1- 5%) of the incident electrons are backscattered into vacuum without losing energy.

4.1.2 Diffraction Conditions

Consider an electron beam in field free space interacting with an ordered surface region for which its diperiodic character is characterized by unit mesh vectors, s_1 and s_2. The effective translational symmetry for the sample is then specified by translation vectors

$$t = m \, s_1 + n \, s_2 \,, \tag{4.2}$$

where m, n are integers. The electron beam in vacuum can be described by a plane wave

$$\Psi(r) = \exp(ik \cdot r), \tag{4.3}$$

where **k** is the wave vector (magnitude $2\pi/\lambda$ with direction of beam) and **r** the position vector. In general, for particles scattering into solid angle Ω, the differential cross-section

$$\frac{d\sigma}{d\Omega} = \left(\frac{m}{2\pi\hbar^2}\right)^2 \left| < \Psi |T| \Psi_0 > \right|^2 \tag{4.4}$$

is determined by a matrix element $< \Psi \,|\, T \,|\, \Psi_0 >$ of the transition operator T, where Ψ and Ψ_0 are the incident and scattered plane waves respectively. For an ordered surface, the Hamiltonian of the LEED electron in the presence of the scattering crystal is invariant under a symmetry operation S of the crystal, then following Messiah [104]

$$< \Psi \,|\, T \,|\, \Psi_0 > \,=\, < \Psi \,|\, S^{-1}\,TS \,|\, \Psi_0 > \,=\, < S\Psi \,|\, T \,|\, S\Psi_0 >. \tag{4.5}$$

If, in particular, S represents a diperiodic translation vector **t** of the surface net, then

$$S\Psi(\mathbf{r}) = \Psi(\mathbf{r}+\mathbf{t}) = \exp[\,i\mathbf{k}\cdot(\mathbf{r}+\mathbf{t})\,] \tag{4.6}$$

Here S has the effect of translation from **r** to **r** + **t**. A corresponding relation holds for $S\Psi_0(\mathbf{r})$, and hence the two ends of Eq.(4.5) give

$$< \Psi \,|\, T \,|\, \Psi_0 > \,=\, \exp[\,i\,(\mathbf{k}_0 - \mathbf{k})\cdot\mathbf{t}\,] < \Psi \,|\, T \,|\, \Psi_0 > \tag{4.7}$$

which with Eq.(4.4) immediately requires either $< \Psi \,|\, T \,|\, \Psi_0 > \,=\, 0$ (i.e. no scattering intensity) or

$$\exp[\,i\,(\mathbf{k}_0 - \mathbf{k})\cdot\mathbf{t}\,] = 1 \tag{4.8}$$

Equation (4.8) is satisfied by

$$(\mathbf{k}_0 - \mathbf{k})\cdot\mathbf{t} = 2\pi \times integer \tag{4.9}$$

or alternatively

$$\mathbf{k}_{g\,\|} = \mathbf{k}_{0\,\|} + \mathbf{g} \qquad \text{(diffraction condition)} \tag{4.10}$$

where the subscript $\|$ indicates a component parallel to the surface, and each scattered wave vector $\mathbf{k}_g$ is characterized by **g**, a reciprocal net vector of the diperiodic surface. There is

therefore a direct correspondence between individual diffracted beams and individual vectors of the reciprocal net. The latter can be expressed as

$$\mathbf{g} = h\ s_1^* + k\ s_2^* \qquad\qquad \text{(h, k integers)} \qquad\qquad (4.11)$$

where

$$s_1 \cdot s_1^* = 2\pi \qquad\qquad\qquad s_1 \cdot s_2^* = 0$$

$$s_2 \cdot s_2^* = 2\pi \qquad\qquad\qquad s_2 \cdot s_1^* = 0 \qquad\qquad (4.12)$$

and (s_1^*, s_2^*) are the corresponding unit mesh vectors in reciprocal space.

For elastic scattering, the wave vectors of the incident $(\mathbf{k_0})$ and diffracted $(\mathbf{k_g})$ waves satisfy:

$$|\mathbf{k_g}| = |\mathbf{k_0}|. \qquad\qquad (4.13)$$

The two basic conservation conditions for elastic LEED are Eqs. (4.10) and (4.13); the first corresponds to the conservation of momentum parallel to the surface, and the second to the conservation of energy.

Changes in the diperiodicity of a well-ordered crystal surface, for example following the adsorption of a gas, result in changes observed in the diffraction pattern. Frequently, the new surface unit mesh vectors, s_1 and s_2, are simply related to those of the substrate (i.e. the ideal surface truncated from the single-crystal bulk), $\mathbf{a}_1$ and $\mathbf{a}_2$. There are two nomenclatures in use to describe the associated surface structures, namely that due to Wood [105] and the more general matrix notation [106]. In this work, Wood's notation in the form (p×q) is sufficient, and is the only one detailed here. An illustration is given in Figure 4.1, where unit mesh vectors s_1 and s_2 with O adsorbate present (at 0.25 ML coverage, i.e. one O atom for every four Zr atoms in topmost layer of the substrate) are compared with those ($\mathbf{a}_1$ and $\mathbf{a}_2$) of the Zr(0001) substrate. For that case,
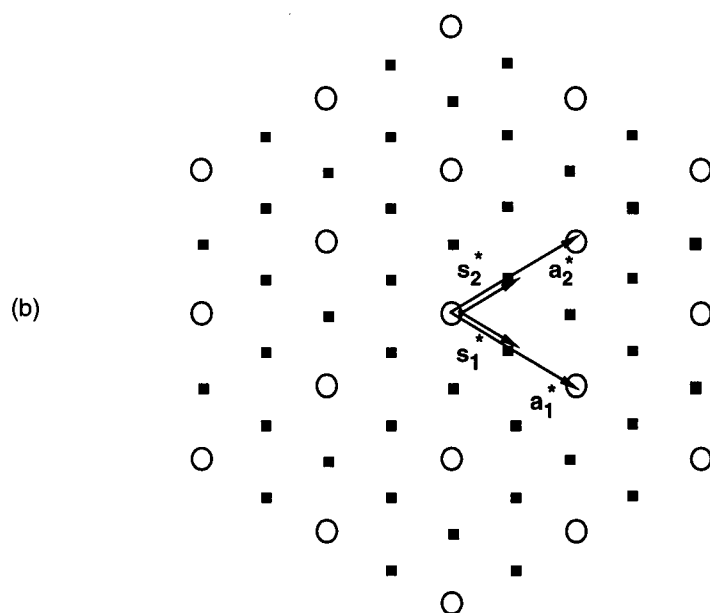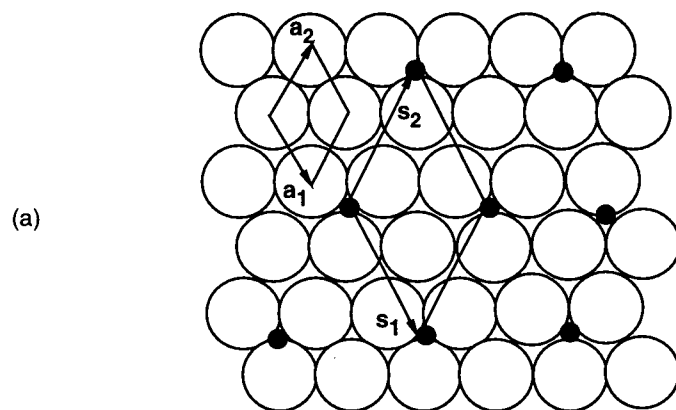
Figure 4.1   Diagrams showing: (a) unit mesh vectors for the Zr(0001)-(2×2)-O surface and the Zr(0001) substrate, (b) the corresponding reciprocal space vectors.

$$s_1 = 2\,\mathbf{a}_1 \qquad (p = 2)$$

$$s_2 = 2\,\mathbf{a}_2 \qquad (q = 2)$$

and the notation for the surface structure is written Zr(0001)-(2×2)-O. The corresponding reciprocal vectors for the surface with adsorbate (s_1^* and s_2^*) and the substrate ($\mathbf{a}_1^*$ and $\mathbf{a}_2^*$) are indicated in Figure 4.1 (b).

4.1.3 LEED from Incompletely Ordered Surfaces

At the microscopic level, single crystal surfaces inevitably have some heterogeneous character, for example associated with adsorbate islands or separate domains resulting from the presence of atomic steps. The diffraction pattern observed depends both on the domain dimension and the instrumental transfer width [107]. The latter gives the maximum distance over which the instrument can recognize atomic order; it is infinite for ideal equipment, but finite for real instruments with divergences in beam directions and energies (LEED instrumentation of the sort used here typically has a transfer width of around 100 Å). For the zirconium surface used in this work, which has the hexagonal close packed (hcp) structure, the individual close packed layers, parallel to the (0001) plane, are stacked in the ABAB... sequence. But two terminations are possible: either as ABAB... or as BABA.... For careful cutting of the crystal, each type of domain should have equal probability. The actual LEED pattern observed represents a summation of patterns from the individual types of domain provided their dimensions are greater than the instrumental transfer width. For these conditions, the LEED pattern from a Zr(0001) surface shows an apparent 6-fold symmetry at normal incidence; this is a 'domain averaged' pattern which results from the superposition of two 3-fold patterns (Figure 4.2).
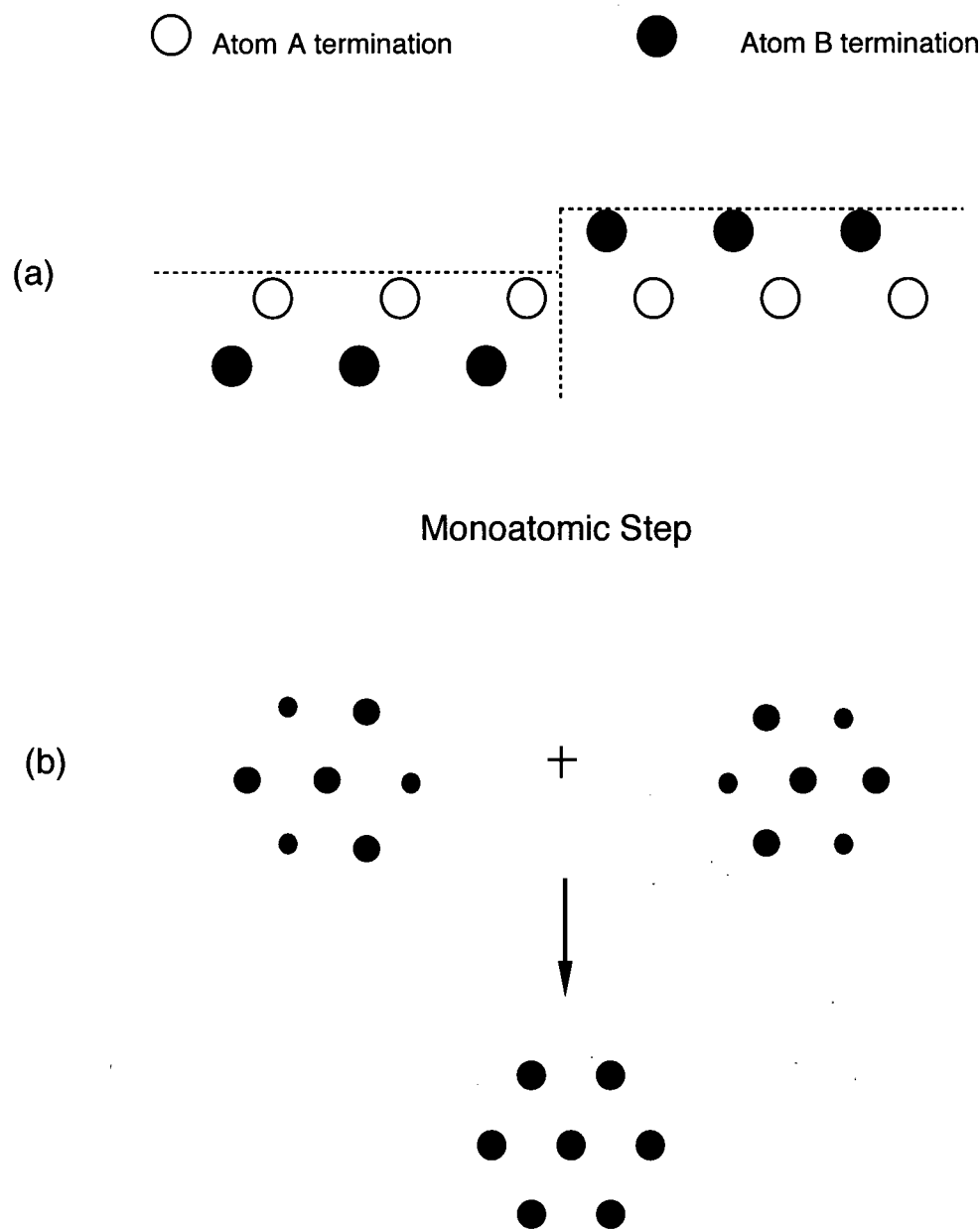
Figure 4.2   Termination at hcp(0001) surface: (a) side view with A termination and B termination, (b) superposition of two 3-fold symmetrical LEED patterns to form a 6-fold symmetrical LEED pattern at normal incidence.

The existence of domains can sometimes lead to ambiguity in interpretation of a LEED pattern. The example of a (2×2)-type pattern just considered could also arise from 3 equivalent (2×1) domains, which are rotated by 120° to each other. The two types of superstructures, and their individual and summed LEED patterns are illustrated in Figure 4.3.

An ideal LEED instrument would detect diffracted beams of δ-function form from an ideal ordered surface, but this picture must be modified for real heterogeneous surfaces studied with real equipment. A sharp LEED pattern, with low background between the diffracted beams, is generally taken as a guide to a well-ordered surface. This is most meaningful when measurements are made with a high-resolution instrument with large transfer width, as is used in LEED spot profile analysis [108]. In that approach, the measured broadening of diffracted beams is used to quantify disorder characteristics for the surface. The further method of diffuse LEED (DLEED) allows measurement and analysis of diffuse intensities from disordered surfaces to give local structural information [109,110].

4.2 Multiple Scattering Calculation of LEED Intensities

The strong elastic scattering, and the consequent multiple scattering nature of low-energy electron diffraction (Section 4.1.1), results in the kinematic theory, which has been most successful for treating X-ray diffraction [111], being insufficient to handle LEED. A dynamical theory of diffraction is thus required for the latter context. Fuller accounts of the theory can be found in many references [29,30,112-114], but only introductory outlines of the calculation schemes are given here.

In LEED, the total wave function outside a crystal can be written as
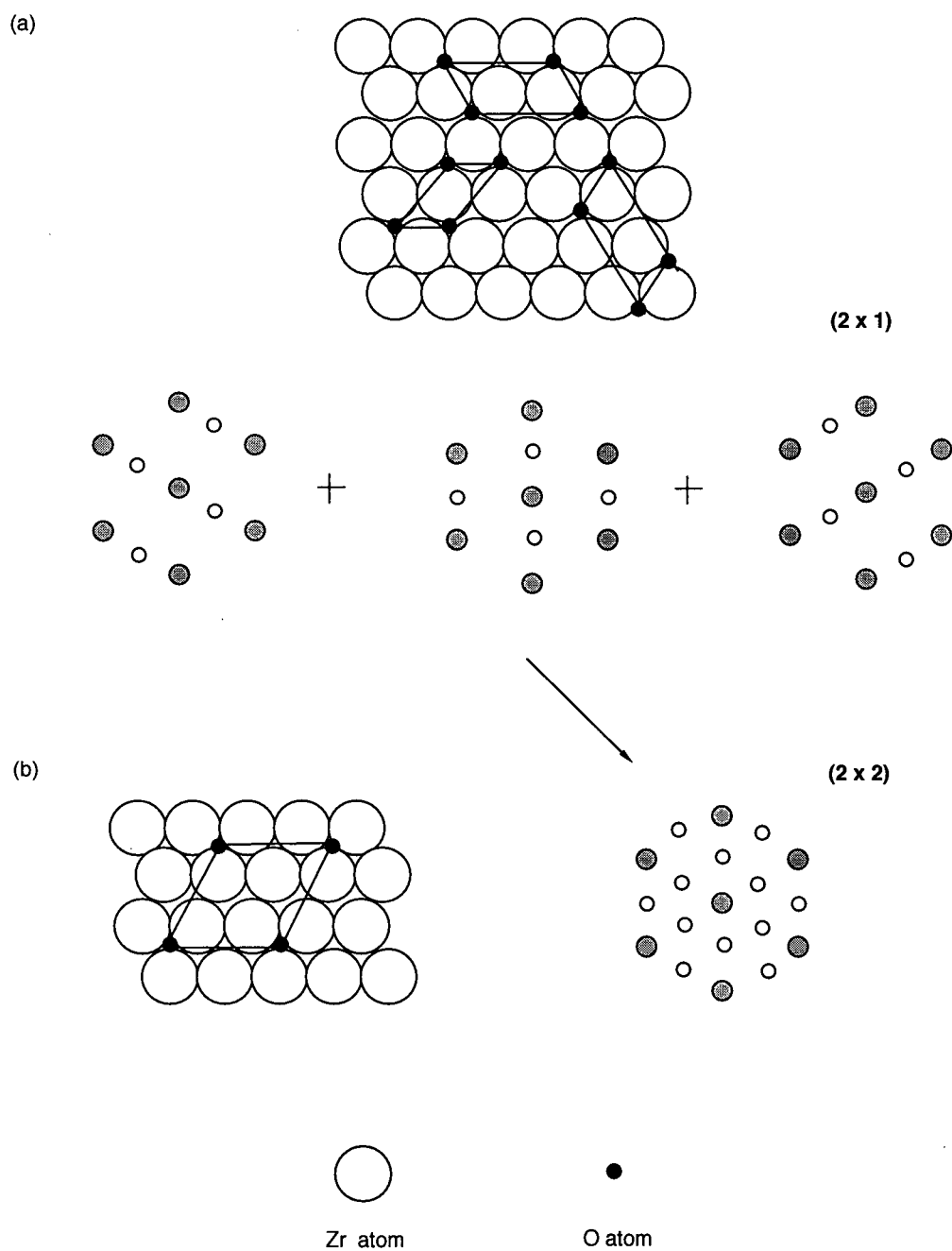
Figure 4.3   Possible structures compatible with (2×2) LEED pattern formed by O at Zr(0001)

surface: (a) three rotationally-related domains of (2×1), (b) a genuine (2×2) surface.

$$\Psi_{out}(\mathbf{r}) = \exp(i\,\mathbf{k}_0 \cdot \mathbf{r}) + \sum c_g \exp(i\,\mathbf{k}_g \cdot \mathbf{r}) \qquad (4.14)$$

where exp $(i\mathbf{k}_0 \cdot \mathbf{r})$ and exp $(i\mathbf{k}_g \cdot \mathbf{r})$ represent the incident and diffracted plane waves respectively. The beam intensity (or reflectivity) of the **g**th diffracted beam is

$$R_g = \frac{k_{g\perp}}{k_{0\perp}} |c_g|^2 , \qquad (4.15)$$

where $k_{g\perp}$ and $k_{0\perp}$ are the perpendicular components of wave vectors of the diffracted and incident beams respectively [115]. The objective of a LEED calculation is to determine the intensities of the elastically diffracted beams, normally as a function of electron energy to give the intensity-versus-energy or I(E) curves. In LEED crystallography, I(E) curves calculated for various surface models, and for all diffracted beams, are compared with experimental I(E) curves to determine the correct structural arrangement. In this way, surface structural information such as adsorption sites, bond lengths and interlayer spacings can be obtained.

Most LEED calculations use the muffin-tin model [30] for the scattering potential (Figure 4.4). In this model, a spherically symmetric potential (of appropriate muffin-tin radius) is assumed around each atom, with a constant potential for the interstitial region outside of the spherical regions. The constant potential between the spheres (called the 'muffin-tin zero' V_o) is given the complex form

$$V_0 = V_{0r} + iV_{0i} \qquad (4.16)$$

The real component V_{0r} accounts for the lowering in potential energy which an electron experiences on entering the solid. Variations in its value primarily shift the energy scale of the calculated I(E) spectra, and V_{0r} is normally treated as an adjustable parameter in a structural search [30]. The imaginary component V_{0i}, when negative, accounts for the attenuation of the electron beam intensity, caused by inelastic processes including plasmon and phonon excitations,

(a)

X   X'

Potential

(b)

V_0

Position
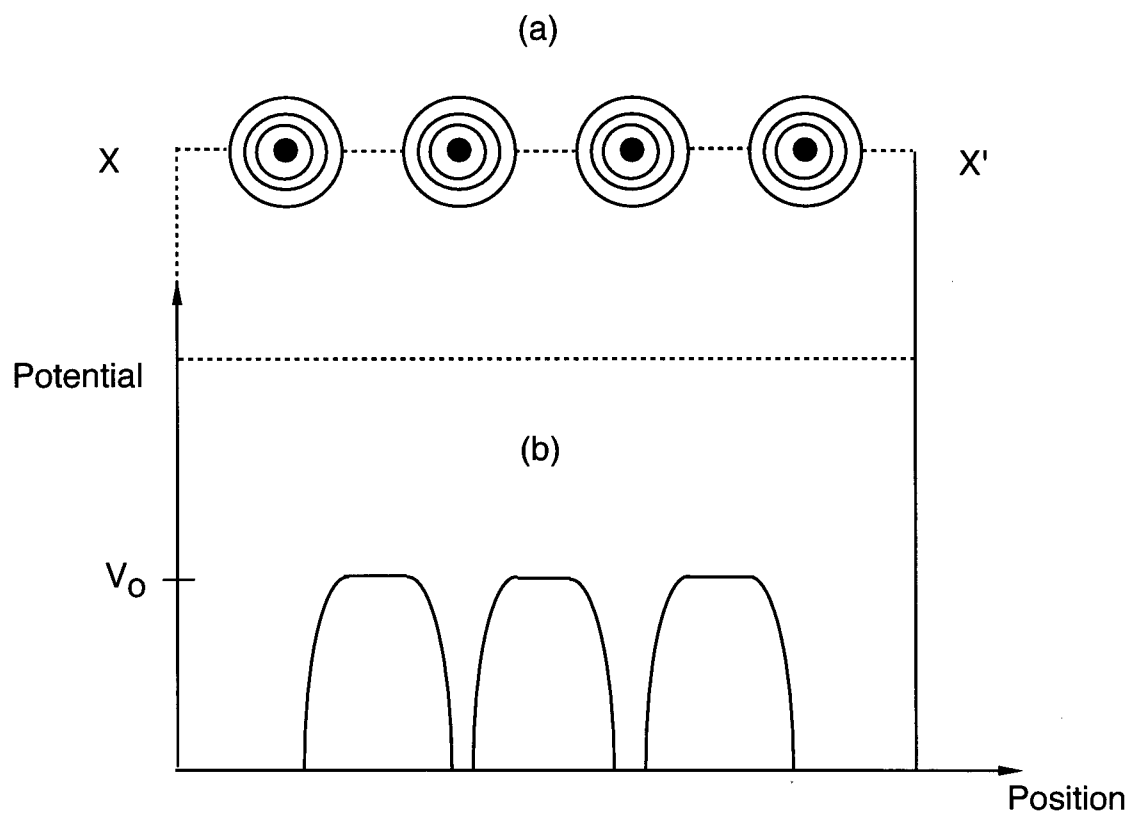
Figure 4.4   Illustration of muffin-tin approximation through a single row of ion cores along XX': (a) potential contour plot, (b) variation of potential (V_0 is muffin-tin zero).

68

as the beam propagates in the crystal. Also, V_{0i} determines the width of the interference peaks in the I(E) spectra in the sense that the larger $|V_{0i}|$, the broader the peaks. Some have suggested a weak energy dependence for this parameter (e.g. as $E^{1/3}$ [116]), but a constant value of -5 eV has been used for V_{0i} throughout the LEED calculations made in this work.

The calculation of LEED intensities for scattering by a well-ordered surface region is conveniently done in three steps: It starts with scattering by a single atom, followed by coherent summation of atomic scattering amplitudes from all atoms in a layer; and finally, contributions from different layers are summed to give the total diffraction amplitude scattered by the surface. Mathematically, two different types of basis functions are suggested. In the angular-momentum (L-space) representation, the electron waves are described by spherical waves, which occur naturally for scattering by spherically symmetric potentials, while in the linear momentum (K-space) representation, use is made of plane waves, which occur naturally for regions of constant potential. In principle, wave functions for LEED electrons inside a crystal surface can be expanded in terms of either spherical waves or plane waves, and Marcus [31] has discussed the mathematical transformations between these two representations. Throughout the formulation of a LEED calculation, these two approaches are available; which is used at each point is decided by the efficiency for the whole calculation.

1. *Atom Scattering* The elastic interaction of an incident plane wave (wave vector **k**) with a spherical atomic potential yields a scattered wave with the asymptotic form

$$\exp(i\mathbf{k.r}) + t(\theta) \frac{\exp(ikr)}{r}, \qquad (4.17)$$

where t(θ) is the scattering amplitude for scattering angle θ and r is the distance from the nucleus.

The scattering amplitude can be expressed in terms of Legendre polynomials P_ℓ by a partial

wave expression:

$$t(\theta) = 4\pi \sum_\ell (2\ell + 1) \, t_\ell \, P_\ell(\cos\theta)$$ (4.18)

where t_l is a t-matrix element given by

$$t_\ell = \frac{\exp(i\delta_\ell)\sin\delta_\ell}{2k}$$ (4.19)

The δ_ℓ in Eq (4.19) are the phase shifts (for angular momentum values $\ell = 0,1,2, ..$) [117] and

they are characteristic of the particular potential and energy. The phase shifts are attained by

integration of the radial Schrödinger equation in the presence of the ion core potential. In general

the number of phase shifts required is smaller for weakly scattering atoms than for those that are

strongly scattering; also the number required increases with energy.

Thermal effects are included by multiplying the atomic scattering amplitude t(θ) with a

Debye-Waller factor:

$$t^T(\theta) = \exp(-M) \, t(\theta)$$ (4.20)

where $t^T(\theta)$ is the effective atomic scattering amplitude and

$$M = \frac{1}{6}|\Delta k|^2 < (\Delta r)^2 >$$ (4.21)

Here Δk is the momentum transfer due to diffraction from one plane wave into another and

$<(\Delta r)^2>$ is the mean-square amplitude of vibration. For isotropic harmonic vibrations,

$$< (\Delta r)^2 > = \frac{9T}{mk_B\theta_D^2}$$ (4.22)

70

in the high temperature limit. In Eq. (4.22) T and θ_D are the real and Debye temperatures, m is the atomic mass, and k_B is Boltzmann's constant. The Debye temperature indicates the rigidity of a solid with respect to vibrations; the higher θ_D the stronger the bonding in the solid [118].

For these assumptions, Jepsen *et al.* [119] have shown that the effect of a vibrating lattice can be included by a renormalizaton of the atomic phase shifts for the corresponding stationary lattice. Given this, the temperature-dependent phase shifts δ_ℓ^T for a LEED calculation are generated automatically by the computer program given the basic input parameters including phase shifts for stationary atoms (δ_ℓ), the Debye temperature (θ_D) and the surface temperature (T). In practice for a vibrating lattice, $\ell_{max} = 7$ (i.e. eight phase shifts) is generally satisfactory for energies less than about 250 eV. That has been followed in the present work. The phase shifts used for Zr were initially determined from a band structure calculation by Moruzzi *et al.* [120] whereas those for O were determined by Demuth *et al.* [121] from an atomic potential calculated in an appropriate cluster using the superposition of atomic charge density procedure [122].

In summary, the scattering properties of an atom enter the LEED calculation via the atomic phase shifts, which are determined by the potential extending from the nucleus to the muffin-tin radius. In effect, the use of phase shifts allows the atom to be treated as a point scatter without the need to consider its extension in space in the full calculation. Parameters required as input to a program for LEED multiple scattering calculations divide into two groups: (i) the geometrical (or structural) parameters which fix atomic positions within the model of the surface, and (ii) the 'non-structural' parameters which include the atomic phase shifts, the Debye temperature and muffin-tin zero parameters (V_{or} and V_{oi}).

2. *Layer Diffraction* Spherical waves which have been scattered by one atom can subsequently

be multiply scattered by other atoms in the same layer. Figure 4.5 (a) indicates schematically

multiple scattering between two atoms. In the L-space representation, the scattering from one

atom to another is covered by propagators (Green's functions, e.g. G^{21} and G^{12} in Figure 4.5 (a))

which describe the free-space propagation of scattered spherical waves between the atoms and

are implicit function of atomic positions [29]. The amplitude of a wave which arrives at the

second atom after being scattered by the first is represented by $G^{21}t^{1}$, where t^{1} is the t-matrix of

atom 1 (assumed for a vibrating atom). This scheme can be extended, by matrix equations which

sum over all possible scattering paths to an infinite, diperiodic plane. The layer diffraction is

then described by a diffraction matrix $M^{\pm\pm}$, as has been discussed by Van Hove and Tong

[114]. The matrix element $M^{\pm\pm}_{g'g}$ specifies the amplitude of a diffracted beam $k^{\pm}_{g'}$, given an

incident plane wave $k^{\pm}_{g}$ of unit amplitude. The $M^{\pm\pm}$ matrix distinguishes between reflected and

transmitted plane waves as illustrated schematically in Figure 4.5 (b). The layer reflection (r) and

transmission (t) matrices satisfy:

$$r^{+-} = M^{+-}, \qquad r^{-+} = M^{-+}, \qquad t^{++} = M^{++} + I, \qquad t^{--} = M^{--} + I \qquad (4.23)$$

where I is the unit matrix for representing the unscattered plane wave when it is transmitted

without change of direction through the layer [114].

3. *Diffraction by a Stack of Layers* The presence of significant inelastic scattering experienced

by electrons propagating in real solids ensures that the surface diffraction can be represented by

diffraction by just a finite stack of layers. The associated diffraction matrices are calculated by

stacking the single layer diffraction matrices. In principle, this can be performed in either the K-

or L-space representations. Since K-space calculations generally require less computational
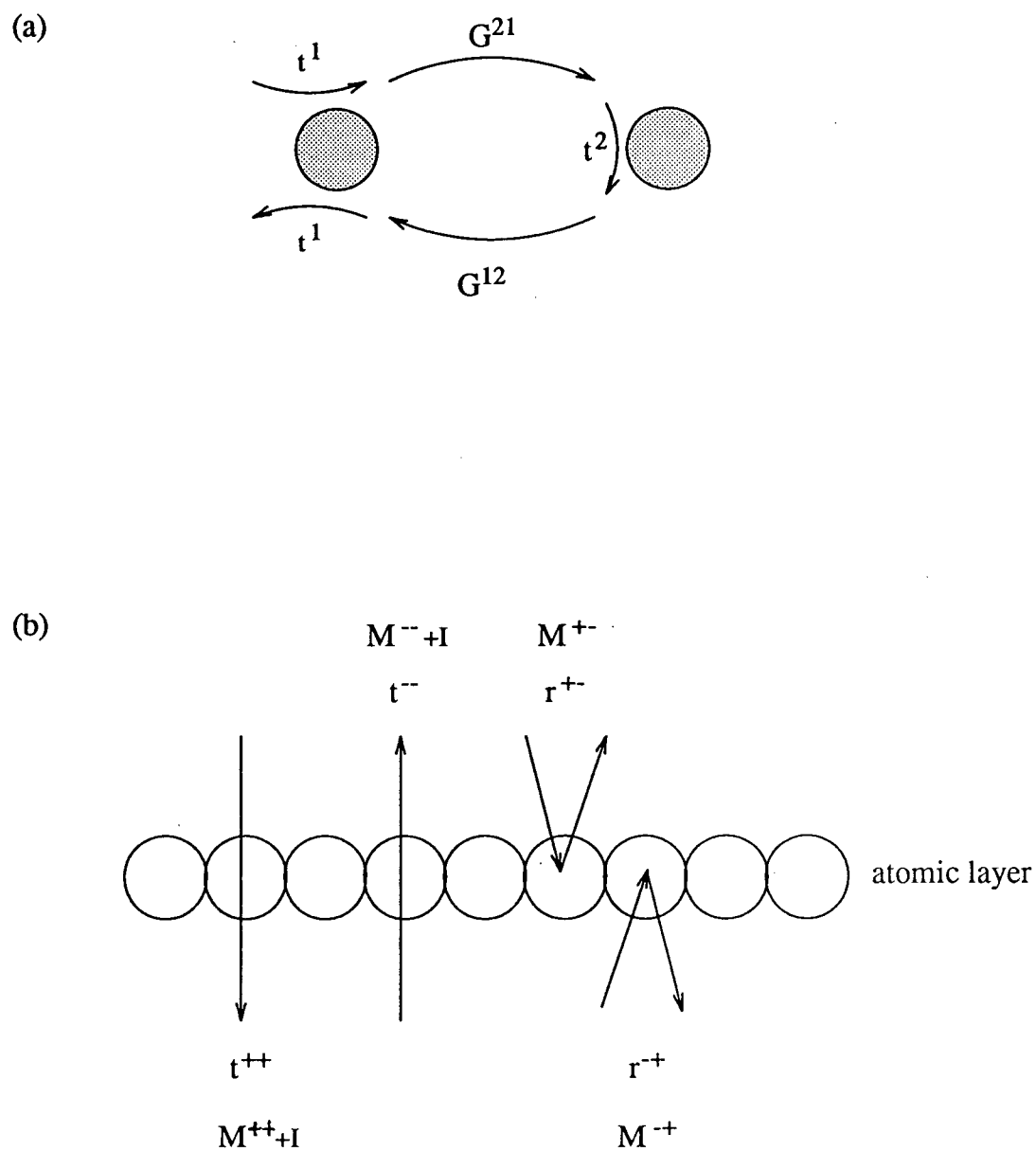
Figure 4.5 Schematic indication of multiple scattering: (a) between two atoms, (b) showing the transmission (t) and reflection (r) matrices for scattering by a single layer of atoms.

times, this approach is favored when there is satisfactory convergence. Specific methods available are the renormalized-forward-scattering (RFS) method and the layer-doubling (LD) method, both introduced by Pendry [30], and the combined-space (CS) method introduced by Tong and Van Hove [123]. Calculations of LEED intensities in this research used both the RFS and CS methods.

(I) Renormalized-forward-scattering (RFS) method

The RFS method is a perturbative approach based on the idea that backward diffraction (or reflection) is weak compared to forward diffraction (or transmission) [124]. Figure 4.6 illustrates a number of the possible scattering paths in which beams propagate into the crystal, and undergo various scatterings in both the forward and back directions according to the layer reflection (r) and transmission (t) type matrices respectively. The longer the path the greater the damping, and all possible paths that can scatter significant amplitude back into vacuum are grouped, on the basis of the number of backscattering events, into first, second, third and higher order categories. The wave backscattered out of the crystal to first order have undergone one layer reflection; those to second order have undergone three layer reflections, and so on. The backscattered amplitude is summed until higher order contributions become negligible, at which point the process is considered to have converged.

RFS is the fastest method for stacking layers, but it may need the inclusion of as many as 12-15 layers and 3-4 orders of iteration for convergence. However, this method can fail to converge with interlayer spacings less than about 1 Å. In such cases the LD method or CS method should be used instead.
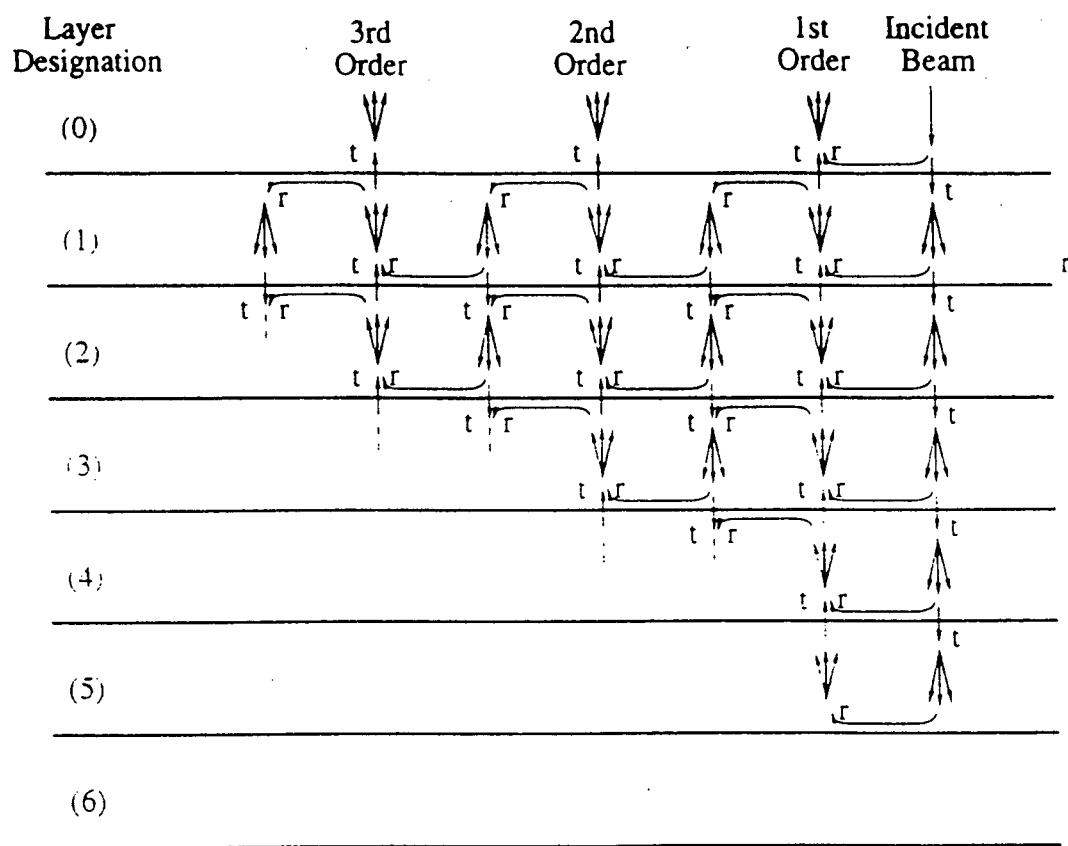
Figure 4.6   Some scattering paths in the renormalized forward scattering (RFS) perturbation method.

(II) Combined-space (CS) method

Both the RFS and LD methods use the plane wave (K-space) representation to calculate the scattering amplitude from a stack of layers, but the number of plane waves needed increases as the interlayer spacings reduce. For spacings less than about 0.5 Å, the dimension of the matrices involved can become too large for numerical reliability. In such circumstances, the more time-consuming full matrix inversion procedure [125] within the L-space representation is required. However a compromise is possible for surfaces which have some close interlayer spacings, while others are more widely spaced. For this situation, Tong and Van Hove formulated a 'combined space method' [123]; in this approach the surface layers, where small interlayer spacings occur, are treated as a composite layer consisting of two or more subplanes, each of which contains only one atom per unit mesh. Diffraction properties of the composite layer are calculated in the L-space representation, while the stacking of the composite layer onto the substrate is done in the K-space representation.

When the rotational symmetry of a surface is lower than that of the substrate, rotationally related domains are to be expected. At normal incidence, when it is along a symmetry direction, diffracted intensities need only be calculated from one domain, but an appropriate averaging of diffracted beams is required to effect a summation of the different patterns from the different domains [126]. The above procedure assumes that the domain sizes are large (compared to the instrumental transfer width) and that the different domains are equally populated. Such conditions may be approximated in practice when the sample is well-oriented, and it manifests a sharp diffraction pattern.

4.3 Measurement of LEED Intensities

4.3.1 Instrumentation

The LEED studies in this work were performed in a Varian chamber, which is ion-pumped to maintain a base pressure of around 2×10^{-10} Torr. A top view of the chamber is depicted in Figure 4.7 (a). The single-crystal sample sits inside a molybdenum sample cup, which is equipped with a resistive heater and to which is attached a thermocouple for measuring crystal temperature. The whole assembly is mounted on a manipulator to allow five degrees of movement for the sample: translation along three orthogonal directions (x, y, z), and variations of the polar (θ) and azimuthal angles (ϕ). Gases are introduced through a variable leak valve from the gas side line; other facilities available are the LEED optics (Varian 981-0127), a cylindrical mirror analyzer (Omicron, CMA100), a sputtering gun and a quadrupole mass spectrometer.

Figure 4.7 (b) shows the pumping system used for this chamber and the associated gas line. Initial roughing (to ~ 10^{-3} Torr range) is accomplished by a liquid nitrogen-cooled sorption pump; the chamber pressure is then reduced to about 10^{-7} Torr by a water-cooled, liquid nitrogen-trapped diffusion pump prior to turning on the ion pump which reduces the chamber pressure to about 10^{-8} Torr; and UHV is achieved after baking the chamber at about 150 °C for 12 hours or more followed by a degassing of all filaments.

Figure 4.8 (a) schematically indicates the four-grid LEED optics used in this work. The electron beam, generated by a directly heated tungsten filament, is collimated by a lens system and accelerated to the desired energy E. The sample and the final electrode in the gun are grounded so that the electrons move in a field-free region. Typically the electron beam has a diameter of 1 mm or less over the crystal surface (about 10 cm away), an energy spread less than 1 eV and a current of around 2 μA (lower values for below 120 eV). The detector system

(a)

Ion Gauge

LEED Optics

Sample

Sputtering Gun

Manipulator

CMA

Leak Valve

MS

View Port

(b)

Titanium Sublimation Pump

TSP

IG

Leak Valve

Varian UHV
Chamber

IG

Diffusion
Pump

Gas Line

TCG

TCG

Ar

O₂

20 L/S
Ion Pump

Sorption
Pump

200 L/S
Ion Pump
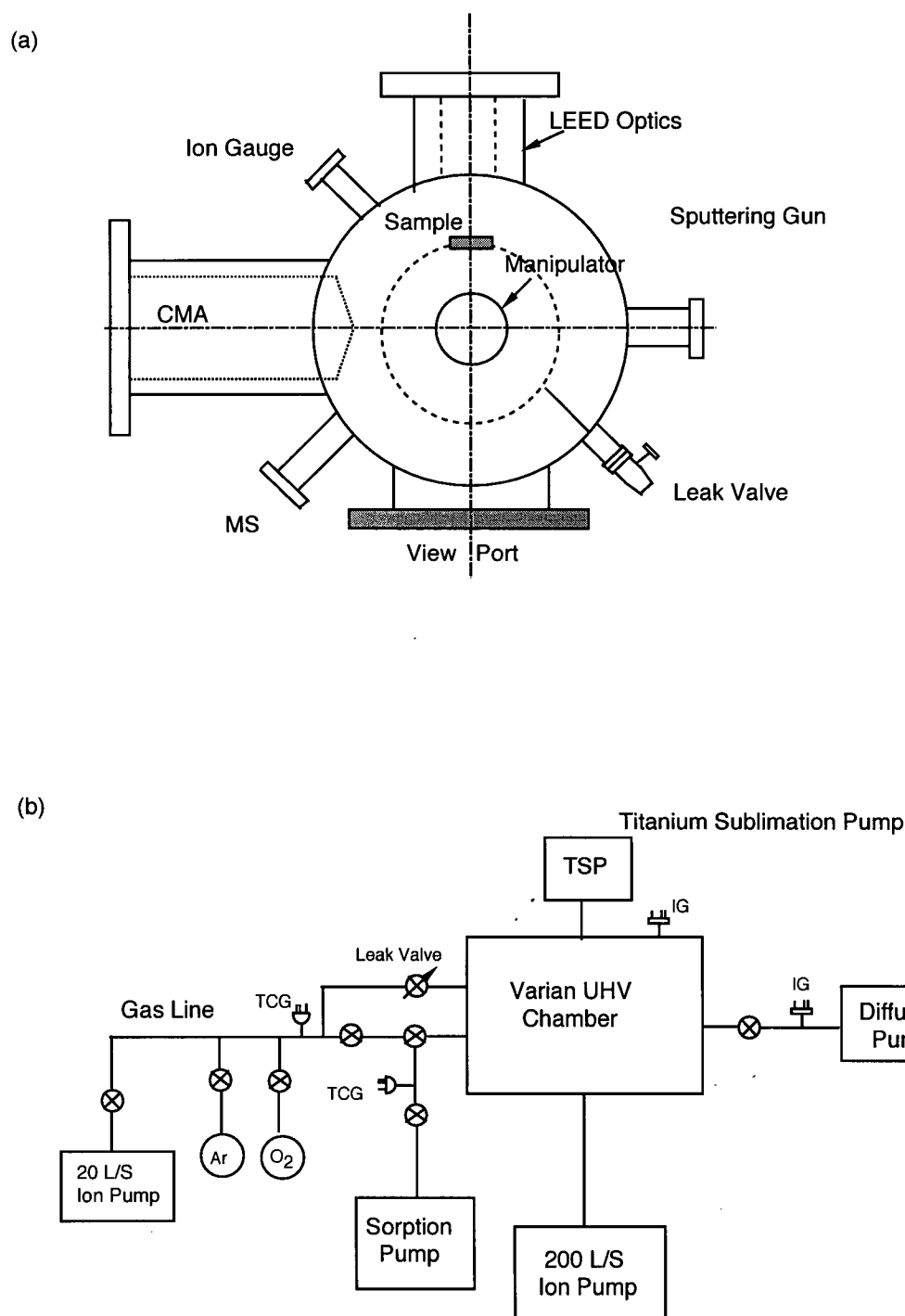
Figure 4.7   UHV chamber for LEED studies: (a) schematic view from top, (b) indication of the pumping system and gas line.

(a)

G₁

Fluorescent Screen

G₄

sample

Electron Gun

+ 5kV

G₃

G₂

1-3 V
Energy
Selection

Beam
Energy

(b)

Voltage
Sweep

Lock-in
Amplifier

Display

Sample

UHV-Chamber

Electron
Multiplier

Cyclindrical Mirror Analyzer
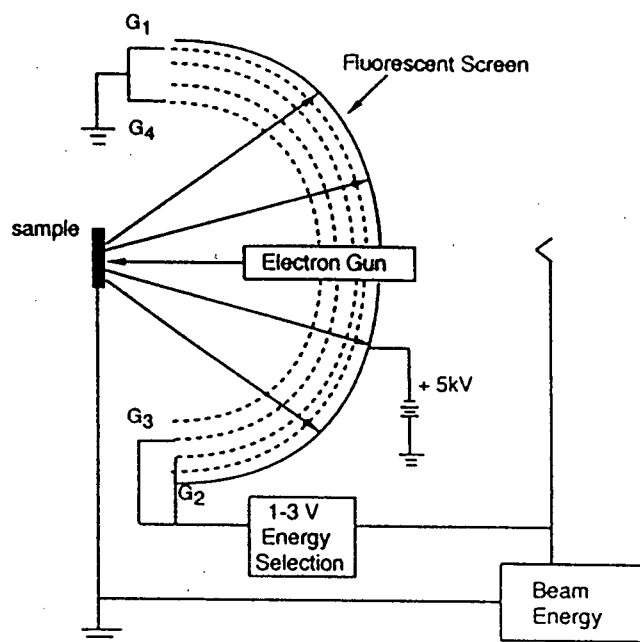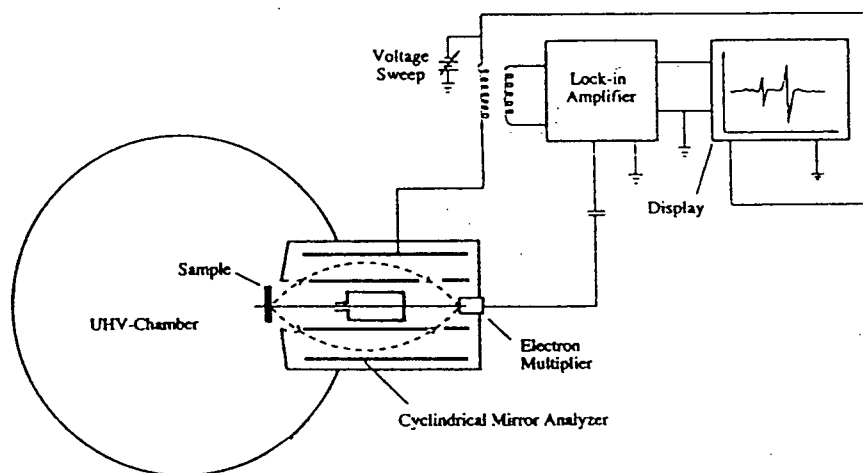
Figure 4.8   Schematic diagrams showing: (a) LEED optics, (b) single-pass cylindrical mirror
analyzer with integrated electron gun.

includes the fluorescent screen and a set of hemispherical grids (transparency to electrons around 80% for each). The first grid is grounded, but the second and third grids are linked together and biased at a slightly negative potential to prevent most inelastically scattered electrons from reaching the fluorescent screen, which is held at a positive potential (e.g. 5 kV). The fourth grid is grounded to isolate the screen potential from the retarding potential of grids 2 and 3. A set of Helmholtz coils are placed around the chamber to cancel any magnetic disturbance, especially from the earth's field.

A single-pass cylindrical mirror analyzer (CMA) (Figure 4.8 (b)) is used for measuring the intensity of Auger electrons. An electron gun mounted along the axis of the cylinder provides the primary electron beam with typical energy 3 keV and current 2.3 μA. The CMA was first introduced for surface analysis by Palmberg *et al.* [127]. It consists of two co-axial cylinders; the outer one is held at a negative potential (-V) with respect to the inner cylinder which is grounded. Electrons that are emitted from the sample enter the analyzer at 42° to ensure second order focusing and a high transmission for a given energy [128]. For a particular V, only electrons in a narrow energy range can pass through the exit slit to the electron multiplier collector. The energy analysis is done by scanning the DC voltage on the outer cylinder (-V), and simultaneously measuring the electron current at the collector. The Auger electron signals represent small structures on a large background of secondary electrons, and therefore in practice AES measurements are often made in the derivative mode. This is accomplished by superimposing a small sinusoidal voltage ($\Delta V = k \sin\omega t$) on the outer cylinder voltage and synchronously detecting with a lock-in amplifier the component with frequency ω in the signal from the electron multiplier. This directly generates the Auger spectrum in dN(E)/dE vs. E form. A CMA

improves the signal-to-noise ratio (by ~10^2) over a retarding field analyzer based on four-grid LEED optics [129]. In principle, less than 1% of a monolayer of impurity can be detected.

4.3.2. LEED Intensity Measurement Using the Video LEED Analyzer (VLA)

Experimental I(E) curves in the current study were measured with a video LEED analyzer (VLA, Data-Quire Co., Stony Brook, N.Y.) connected to an IBM PC (Intel 486, 66 MHz) as shown schematically in Figure 4.9. A silicon-intensified TV camera placed in front of the viewing window allowed the diffracted pattern to be displayed on a monitor. The camera defined the viewing area as a 256×256-pixel frame and recorded the intensity of each diffracted beam by summing the digitized intensities inside a 10×10-pixel window, which completely covered the spot. The computer unit was programmed to track the moving spots automatically as the incident electron energy was varied. In principle, up to 49 beams could be measured at the same time, but typically in practice no more than six beams were measured in one pass; usually ten passes were made for each set of beams to improve the signal-to-noise ratio. In addition, appropriate gain level settings were chosen for measuring beams of different overall intensity.

This approach for measuring intensities of diffracted beams involves two electron/photon signal conversions: (i) diffracted-beam electron flux to photons at the fluorescent screen; and (ii) photons from the screen to electrons in the TV camera. Although this approach for measuring diffracted beam intensities from the brightness of spots is somewhat indirect, a number of tests have shown that the resulting I(E) spectra can match well with those measured directly using a Faraday cup [36]. In general, for the instrumentation and maximum beam current used, linearity is believed to be maintained over three orders of magnitude in the diffracted beam current [36]. The special advantage of the VLA method lies in its ability to make measurements while the

81
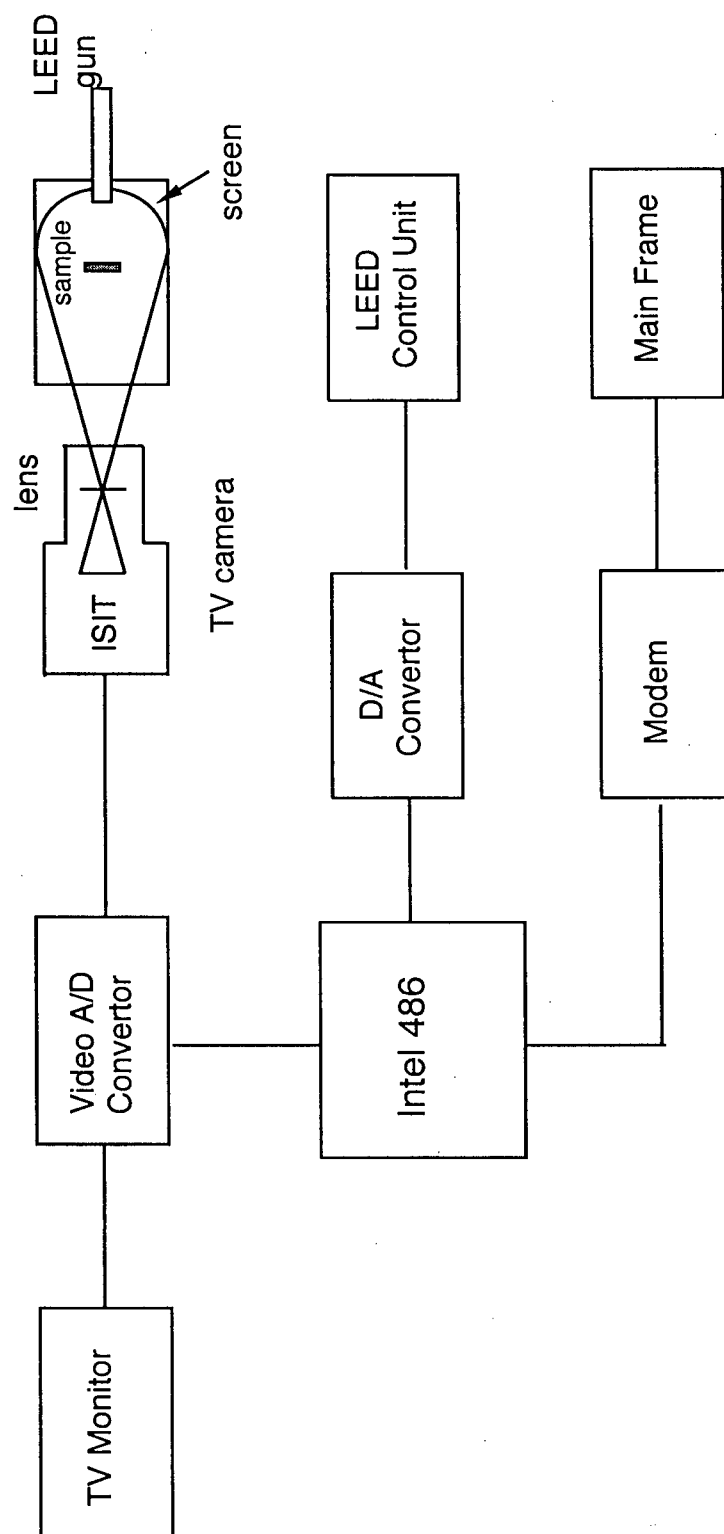
Figure 4.9   Schematic diagram of the video LEED analyzer system.

surface remains in a reasonably constant state (measurements with a Faraday cup, for example, require measurement times at least one or two orders of magnitude greater).

In the first instance, LEED intensities were measured at normal incidence, since this gives the best control on direction and aids the subsequent calculations. Normal incidence is a symmetry direction in the surfaces studied, and I(E) curves for diffracted beams related by symmetry elements possessed by the real surface should be identical insofar as the incidence direction is exactly at the normal. The sample orientation was adjusted until the measured I(E) curves closely reflected the symmetry. When more data were desired than could be obtained at normal incidence, off-normal measurements were made to get more data points. Then, the polar angle θ was determined from the position of the specular beam on the screen with respect to the normal direction after calibrating to angular rotations measured from the manipulator. For these measurements, the azimuthal angle φ was adjusted so that the incidence direction coincided with a reflection plane in the sample; the latter was ensured by checking that measured I(E) curves from appropriate pairs of diffracted beams closely showed the required reflection symmetry.

The raw experimental I(E) curves need treatment before use in a structural analysis. First, they were normalized to a constant incident beam current according to

$$I = \frac{i}{i_0} \tag{4.24}$$

where i and i_0 are measured diffracted and incident currents respectively. This step is necessary because the current from the LEED gun varies significantly with energy, especially below 120 eV. Second, the curves from symmetrically related beams were averaged together. This helps to minimize error associated, for example, with any small misorientations (e.g. deviation from normal incidence, misalignment of the surface) [130]. Finally, the averaged I(E) curves were

smoothed (using a Fourier-transform smoothing scheme) to reduce noise which could adversely affect the later R-factor analysis [114]. Figure 4.10 illustrates these steps applied to a set of experimental data for the (1/2 0) beam from the Zr(0001)-(2×2)-O surface, while Figure 4.11 compares two sets of I(E) curves measured from independently prepared surfaces. The latter correspondence appears at a good level, and is typical of the correspondence between independent measured sets of I(E) curves achieved for all surfaces studied in this work,

4.4 Retrieval of Structural Information

LEED crystallography adopts a trial-and-error approach. Theoretical I(E) curves for a number of chemically plausible models of the surface are calculated, and comparison with experimental I(E) curves is done both visually and with the reliability indices (R-factors) to determine the best match (hence, the most probable model of the surface). A useful R-factor should be sensitive especially to structural parameters, such as atomic positions, and less sensitive to non-structural parameters, such as the Debye temperature and V_{oi}. However, all analyses must optimize V_{or} continually during the experiment-calculation comparisons because of the way it affects peak positions in I(E) curves. Various R-factors have been proposed for LEED as reviewed by Van Hove *et al.* [131] . All the reliability indices are defined so that the closer the correspondence between experimental and calculated I(E) curves, the smaller is R (the lower limit is zero for the correspondence of identical curves).

The most commonly used R-factor in LEED is that proposed by Pendry (R_p) [132] and it has been used throughout the structural studies in this work. It is based on the single-beam function
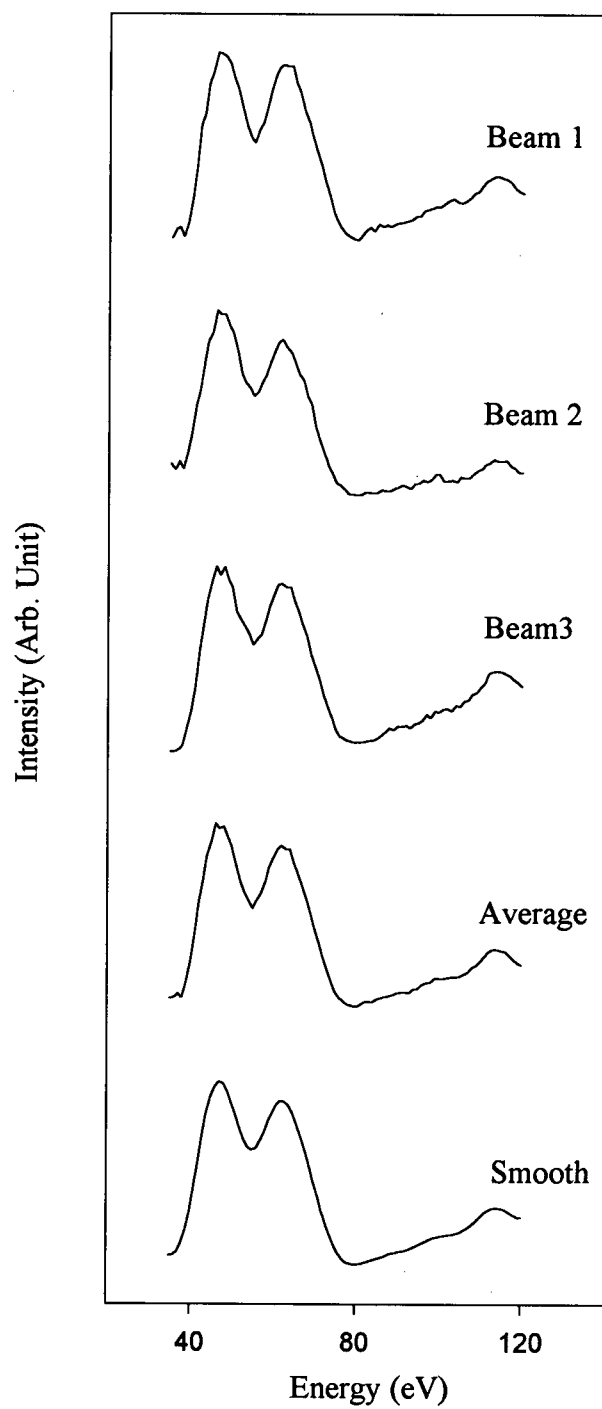
Figure 4.10   Measurement of LEED I(E) curves for (1/2 0) beam at normal incidence from the surface formed by 0.5 ML of O at Zr(0001). Three symmetrically equivalent beams were averaged and then smoothed.
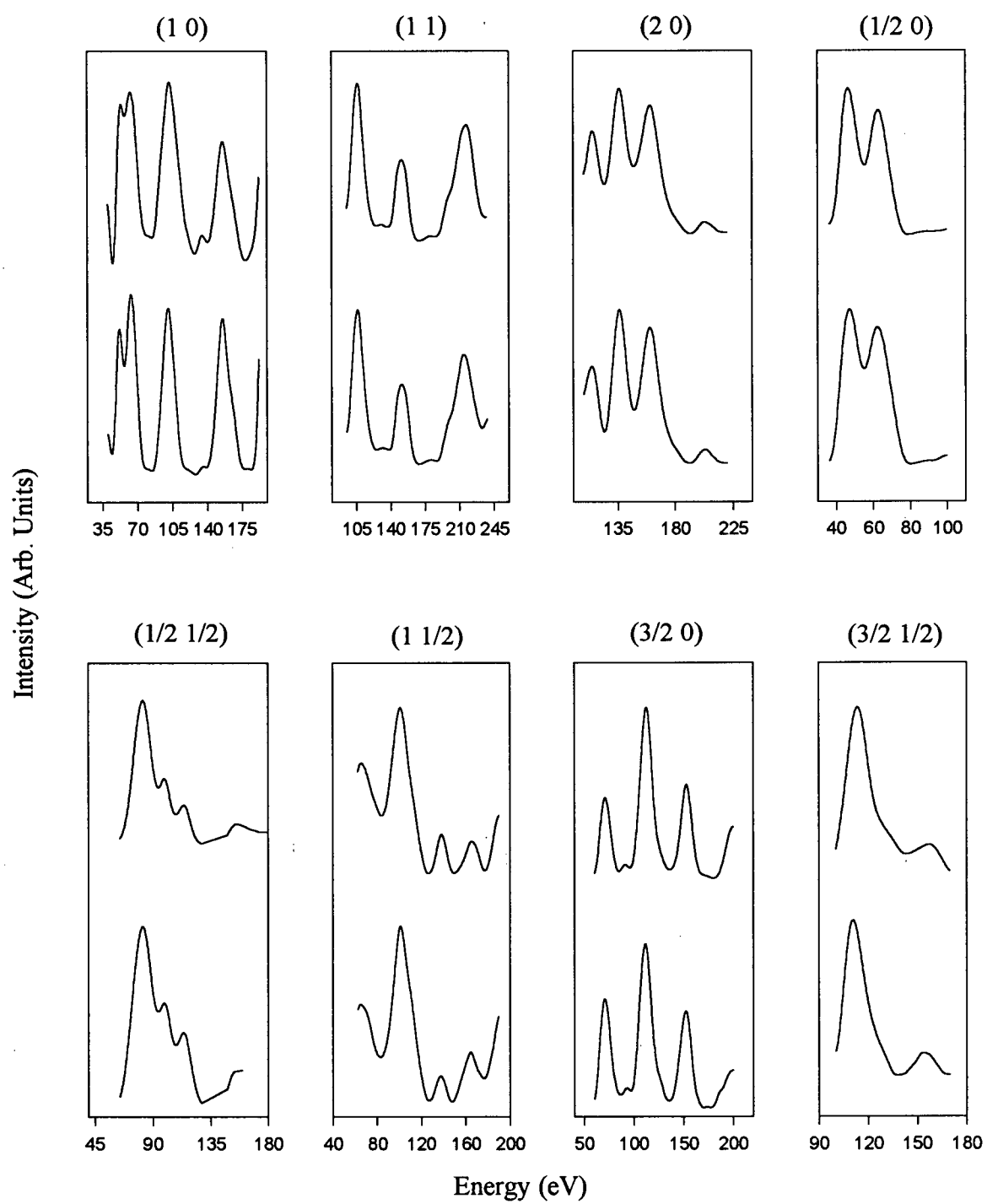
Figure 4.11   Two sets of I(E) curves measured from the surface formed by 0.5 ML of O at Zr(0001) surface.

$$r_p = \frac{\int [Y_{exp}(E) - Y_{cal}(E)]^2 \, dE}{\int [Y_{exp}^2(E) + Y_{cal}^2(E)] \, dE} \tag{4.25}$$

where

$$Y(E) = \frac{L(E)}{1 + V_{oi}^2 \, L^2(E)} \tag{4.26}$$

and L is the logarithmic derivative of the intensity

$$L(E) = \frac{I'(E)}{I(E)} \tag{4.27}$$

The overall R-factor for use in a structural analysis is an average of all the single-beam values with a weighting according to their energy ranges as

$$R_P = \frac{\sum_i r_P^i \Delta E^i}{\sum_i \Delta E^i} \tag{4.28}$$

where summations are over the various diffracted beams.

This index was designed to be approximately unity when there is no correlation between the calculated and experimental curves. It follows the idea that all peaks in I(E) curves carry structural information caused by constructive interference, and it weighs all the peaks equally whether large or small. Pendry also attempted to estimate the reliability of a comparison between experiment and calculation by considering the probability that a minimum in R_p is a local minimum due to the operation of random fluctuations. He defined a 'double reliability factor' (RR) as

$$RR = \frac{var \, R}{R} = \sqrt{\frac{8|V_{oi}|}{\Delta E}} \tag{4.29}$$

where var R is the variance of R, V_{oi} is the imaginary part of the muffin-tin potential V_o and ΔE is the total energy range. He proposed that the reliability of a minimum R_p value is

$$\text{var } RR_{min} = RR \times R_{min} \tag{4.30}$$

which can correspond to an error width for a structural parameter on the R_p versus parameter plot.

Another approach to error estimation is provided by Andersen *et al.* [133]. It is assumed that the R-factor near the minimum can be written as a quadratic form of the different parameters $p(i)$, $i=1,2, \ldots k$ as shown in Eq (4.31), where k is the total number of parameters to be determined. In the generalized form,

$$R = R_{min} + \frac{1}{2}\left(p - p_{opt}\right)^{T} G\left(p - p_{opt}\right) \tag{4.31}$$

where the superscript T signifies a matrix transpose, and the matrix element of G is

$$G_{ij} = \frac{\partial^2 R}{\partial p(i) \partial p(j)} \tag{4.32}$$

Then an error matrix (ε) can be defined by :

$$\varepsilon = G^{-1} \tag{4.33}$$

and the uncertainty results from:

$$\Delta p(i) = \sqrt{\frac{R_{min}\varepsilon_{ii}}{F}} \tag{4.34}$$

where ε_{ii} is a diagonal element of the error matrix ε, and F is the number of degrees of freedom resulting from the total number N of main peaks appearing in the experimental I(E) curves (F = N-k). In principle, this method can be applied to any R-factor. However, there is still no fully accepted approach for estimating error bars in surface structure determinations, even when R_p is used in an analysis. The uncertainties in geometrical parameters determined from the Pendry

procedure are often at least twice those from the scheme of Andersen *et al.*, and these approaches have been seen as giving upper and lower limits respectively [36,134].

4.5 Tensor LEED (TLEED)

Until recently, the application of LEED was limited beyond relatively simple structures because of the extensive multiple scattering calculations required, particularly in the trial-and-error procedure for determining many geometrical parameters. In conventional LEED, for an individual model, the computing time (CPU) scales roughly as N^3, where N is the number of inequivalent atoms in the surface unit cell. Even more seriously, at this level of approach, the times required for the optimization procedure scale roughly exponentially with the number of parameters being varied. An approach for overcoming this challenge is provided by the recently developed tensor LEED method [103], which depends on an approximate scheme for calculating diffracted beam intensities. Further, when combined with an automated search algorithm, the structural optimization can be carried out very efficiently. The approach starts with a particular geometrical structure, or *reference structure*, for which the scattered electron wavefield is calculated exactly. Structural distortions from the reference structure are treated as a perturbation, and Pendry and his collaborators showed that if the atomic displacements are sufficiently small, their effect on the LEED intensities can be calculated directly with scattering matrices stored from the calculation for the reference structure [135-138]. Different levels of sophistication have been proposed [103]; but the most widely available version of the theory, which is used in this work, is briefly outlined as follows.

For a reference structure, the scattering of each atom is expressed in terms of phase shifts as in Eq (4.19). The TLEED approach depends on treating the displacement of atoms from the reference structure as a non-spherical distortion of the scattering potential so that

$$t'^j = t^j + \delta t^j(\delta \mathbf{r}_j),$$ (4.35)

where t_j' and t_j are respectively t-matrices for the displaced and undisplaced atoms j, and δt_j is the change produced by the displacement $\delta \mathbf{r}_j$ (defined relative to the undisplaced atomic position $\mathbf{r}_j$ in the reference structure). The change in each t-matrix element can be written as

$$\delta t^j_{\ell m, \ell' m'} = \sum_{\ell_1 m_1} G_{\ell m, \ell_1 m_1}(\delta \mathbf{r}_j) \, t_{\ell_1} \, G_{\ell_1 m_1, \ell' m'}(-\delta \mathbf{r}_j) - t^j_\ell \, \delta_{\ell \ell'},$$ (4.36)

where G is a spherical wave propagator which converts a spherical wave centered on the original position of the atom $j(\mathbf{r}_j)$ to a set of spherical waves centered on $\mathbf{r}_j + \delta \mathbf{r}_j$, and $\delta_{\ell \ell'}$ is the Kronecker delta. The change in scattering amplitude for a LEED beam with parallel wave vector $\mathbf{k}_{\parallel}$

$$\delta A = \sum_j \left\langle \Psi^+(\mathbf{k}'_{\parallel}) \left| \delta t_j \right| \Psi^+(\mathbf{k}_{\parallel}) \right\rangle$$ (4.37)

can be reexpressed as

$$\delta A = \frac{1}{N} \sum_j \sum_{\ell m, \ell' m'} F^j_{\ell m, \ell' m'} \, S^j_{\ell m, \ell' m'}(\delta \mathbf{r}_j)$$ (4.38)

where N is the number of displaced atoms. The matrix S is a function of atomic displacements alone, and the tensor F contains the information which depends only on the reference structure. The latter, therefore, need only be calculated once, and in consequence I(E) curves for any number of trial structures, each of which would have required doing a new full-dynamical calculation in conventional LEED, can be done quickly by recalculating the matrix S (the CPU time now scales as N, instead of N^3, where N is the number of displaced atoms).

The speed with which I(E) curves for a trial structure can be calculated using TLEED naturally suggests implementation of an automated search procedure [134] which is now available in a program package for the work reported in this thesis. Comparison between the theoretical and experimental curves is done by the program, and the resulting increase or decrease in R-value is used to direct the choice of the next trial structure. This process is repeated until an R-factor minimum is reached. Figure 4.12 illustrates the automated search strategy as realized in the program used in this work [134]. The layer stacking in the TLEED program was performed by the RFS method and the automated search was made using a direction-set Powell algorithm. Symmetry elements possessed by a particular type of trial model could be maintained through the search procedure. This program provided an efficient way to explore the local R-factor hypersurface in the neighborhood of a particular reference structure, although strictly the TLEED approximation maintains its validity only over fairly restricted changes in geometry. For example, Rous [103] suggested the approximation can remain reliable over a vertical separation of up to 0.4 Å in a simple adsorption structure. However, in more complex structures with substantial vertical and lateral displacements, much care is needed in the implementation of this method, practically to avoid just finding local minima in R. In this work, vertical positions of the atoms were optimized before lateral positions, and the analysis was taken through a series of TLEED cycles, each starting from a different but progressively more-refined reference structure, for which a full FD calculation was made. These cycles were repeated until the TLEED-optimized structure showed clear convergence in the atomic coordinates [103].
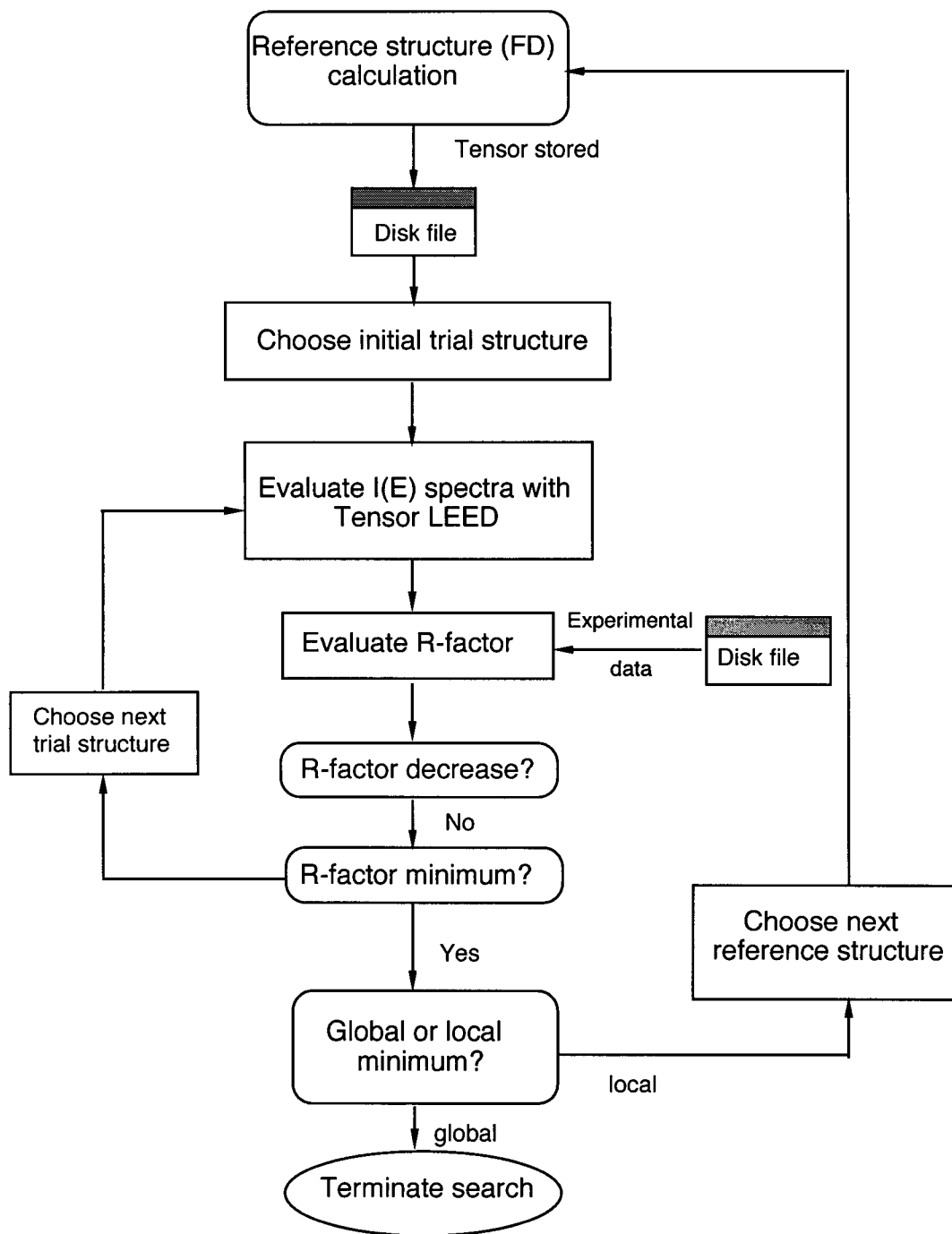
Figure 4.12   Direct search optimization scheme for structural analysis by tensor LEED.

Chapter 5: LEED Analyses for Structures Formed by Zr(0001): the Surface When Clean and When Containing 0.5 ML of O

5.1 Introduction

XPS studies described in Chapter 3 have provided new observations, from the surface chemistry perspective, for the interaction of oxygen with zirconium. To get a better understanding of this process, more knowledge is required for the structures involved, and LEED provides an important approach for determining such details [29]. However, the identification of the structures formed during the initial stages of interaction of oxygen with the (0001) surface of zirconium has provided a challenge for many years [14-16]. This may be attributed to a number of reasons, including: (i) the difficulties of obtaining clean well-characterized zirconium surfaces, given this metal's high reactivity and its bulk phase change at 863°C [139] and (ii) the challenge of optimizing surface ordering with O confined to the surface region (the limitation is set by the onset of O diffusion into the bulk at 230°C [16,17]). Moreover, the initial difficulty in getting good structural determinations for the O on Zr(0001) system also now appears as a consequence of the relaxations that occur in the metallic structure around the incorporated O atoms. A thorough structural analysis, which includes such effects, implies a computational effort that only really became possible after the development of the tensor LEED (TLEED) method, described in Section 4.5.

Earlier studies have shown, when the (0001) surface of zirconium is exposed to oxygen, that a (2×2) type LEED pattern forms at low exposures (e.g. one Langmuir (L) or less) [12,14,16,17], and nuclear reaction analysis [17] indicated that the surface with an O coverage of 0.5 ML corresponds to the point at which the half-order beams are both sharpest and most intense

in the (2×2) pattern [16]. Initial LEED crystallographic analyses [14,15], which compared I(E) curves from experiment with those from multiple scattering calculations, pointed to O atoms incorporating into octahedral hole underlayer sites at the metal surface, for the surfaces which exhibit both the (2×2) and the first (1×1) LEED patterns, although large uncertainties remained. For example, while an initial analysis [14] from a (2×2)-type LEED pattern suggested that O incorporates several layers down with a fcc-type reconstruction for the metal, the study for the (1x1) structure [15], which forms directly with higher exposures, could not convincingly distinguish between the model involving a single underlayer immediately below the zirconium surface and those with deeper O incorporation. Nor indeed, in the latter case, was there clear-cut evidence for the metallic reconstruction. In both these analyses, but more especially that for the (2×2) LEED pattern, the correspondence reached between the calculated and experimental I(E) curves was at a less than satisfactory level. Even so, independent studies with work function measurements have also supported the view that the O interaction gives underlayer absorption [17].

In order to start to fill in some of the uncertainties applying to this challenging surface system, new studies and measurements have been undertaken. As part of this program, a crystallographic analysis with tensor LEED [134] has been made for the half-monolayer structure formed by O at the Zr(0001) surface. Additionally, in order to provide a better basis for comparing with the O structures, a new structural analysis has also been carried out to refine an early study of the clean Zr(0001) surface [140].

5.2 The Clean Zr(0001) Surface

5.2.1 Sample Preparation and Cleaning

The Zr(0001) sample used in this study was cut from a high-purity single crystal rod, provided by Chalk River Laboratories (Atomic Energy of Canada Ltd.), and was oriented and polished to within 0.5° of the (0001) plane [141]. The sample surface was mechanically polished with increasingly finer diamond paste (9-1 μm), followed by a 30 s chemical etch in acid solution (45% HNO_3, 50% H_2O, 5% HF by volume) [142]. From time to time during the polishing process, the sample orientation was rechecked by Laue X-ray back reflection while the optical alignment was done with a He/Ne laser [141,143]. After these preparation steps, the sample (dimensions about 1 mm thick, 8 mm diameter) appeared optically shining, and it was rinsed with trichloroethylene, acetone and then methanol to remove any grease from the surface prior to entry into the LEED chamber.

The cleaning and ordering under vacuum followed established procedures [141,143]. For the first cleaning after entry from atmosphere, considerable Ar^+ bombardment (2 keV, 5-6μA) was needed at room temperature until C was the only detectable contaminant. Then the sample was annealed at 700°C for 30 min to drive C and S impurities to the surface. Several further cycles of Ar^+ bombardment and annealing were needed to minimize the C and S contaminations. To avoid problems with overlapping peaks in AES (e.g. S(150 eV) and Zr(147 eV)), the Auger peak height ratio Zr_{147}/Zr_{92} was monitored to ensure it had the appropriate value for the clean surface (~2.0 for the CMA used in this study) with no significant presence of sulfur [143]. The cleaning procedures for the Zr(0001) surface during the study involved several cycles of Ar^+ bombardment (1.5 keV, 5-6 μA), followed by annealing to around 590°C for about 25 minutes.

Both AES and LEED were used throughout the sample treatments in order to check the surface cleaning and ordering. The Zr(0001) surface was taken to be cleaned and ordered when no AES signals associated with contaminants could be detected with the single pass cylindrical mirror analyzer, and a sharp (1×1) LEED pattern with hexagonal symmetry was apparent for normal incidence [140]. An AES spectrum from a cleaned Zr(0001) surface is shown on page 118.

5.2.2 The Structure of (0001) Surface of Zirconium

Two independent sets of I(E) curves for normal incidence were measured for the (1 0), (1 1) and (2 0) beams from the cleaned and well-ordered Zr(0001) surface. Additionally, I(E) curves from this surface were measured for an off-normal direction of incidence (polar angle θ of 12°, azimuthal direction along $\left[11\overline{2}0\right]$), for five beams designated (0 0), (-1 1), (0 1), (-2 1) and (-2 2) (using the beam notation indicated in Figure 5.1). These two independently measured sets agreed closely, and that with the most extensive energy range (approximately 1210 eV) was used in the tensor LEED analysis. The non-structural parameters in the calculations are specified as follows. The real part of the constant potential (V_{or}) between the muffin-tin spheres was initially set at -10.0 eV and the imaginary part of this constant potential was fixed throughout at -5.0 eV. Values of V_{or} were refined for each structural model during the comparisons of the experimental and calculated I(E) curves. The phase shifts used were specified in Section 4.2, and throughout the Zr Debye temperature was fixed at 270 K [14].

The TLEED program [134] allowed comparison of both the normal and off-normal incidence data simultaneously, and the correspondence between the experimental and calculated intensity curves was assessed with R_p, the R-factor introduced by Pendry (Section 4.4). Two
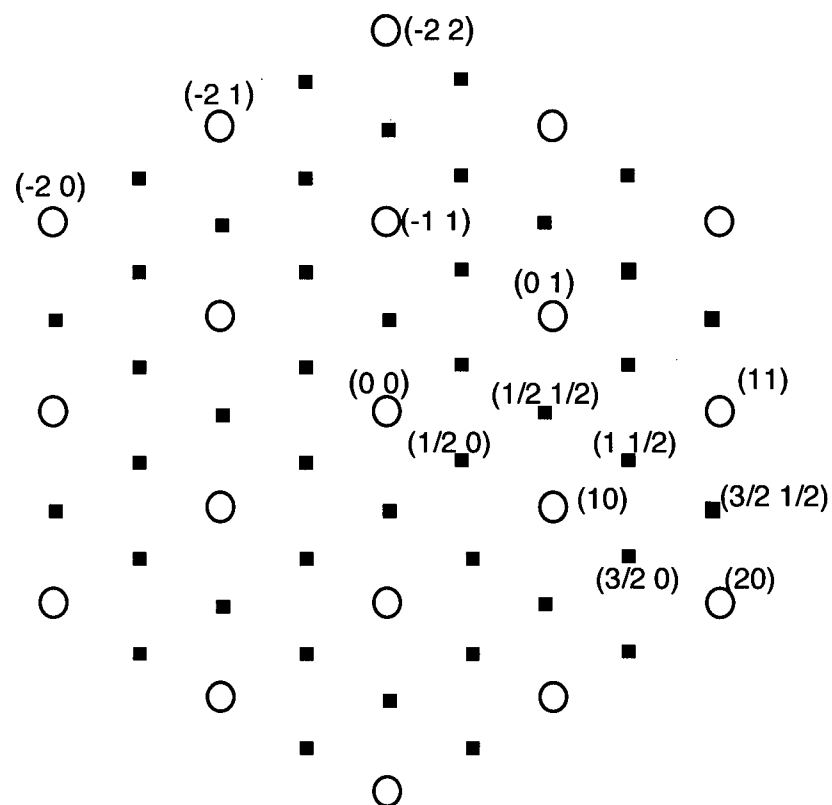
Figure 5.1   Schematic indication of beam notation used for LEED patterns from the O/Zr(0001) surfaces; open circles identify integral beams, while the filled symbols are for fractional beams observed for the (2×2)-type pattern.

termination sequences were investigated for the cleaned Zr(0001) surface. One corresponded to the regular ABAB.. stacking of the hcp bulk structure, while the other designated as CABAB... had a fcc reconstruction for the first three layers. For both models, the first four interlayer spacings were varied during the analysis, and the optimized R_p values turned out to equal 0.238 and 0.386 for the hcp and fcc-reconstructed models, respectively. That the regular structure gave a significantly better correspondence between experimental and calculated I(E) curves was also confirmed by visual inspection, and Figure 5.2 shows this comparison for the favored model. The spacing between the first and second metal layers is determined to be 2.53 Å, which is slightly contracted (by ~1.6%) compared with the bulk value (2.57 Å); this conclusion agrees closely with the early LEED analysis [140]. No significant relaxations below the second layer could be detected (the successive interlayer spacings are indicated to be at 2.58, 2.57 and 2.57 Å). Uncertainties in the first four interlayer spacings are estimated to equal ±0.02, ±0.03, ±0.03 and ±0.04 Å according to the criterion discussed by Anderson *et al.* [133].

While our finding of a slight contraction for clean Zr(0001) is in good agreement with results for other close-packed surfaces of hcp crystals, as indicated by LEED analyses [144,145], it is smaller by a factor of 2.8 compared to that given by the first principles calculations of Yamamoto *et al.* [146]. Similar discrepancies have been found for other close-packed metal surfaces including the Ti(0001) and Ru(0001) surfaces [147]. The origin of this conflict between experiment and calculation is not yet clear, although there has been speculation by a theoretician [147] that H-contamination in the experiment may result in the smaller contractions being reported by LEED. Certainly it would be useful to test for the presence of H by vibrational spectroscopy, and to see how the surface relaxations may change with deliberate exposure to H_2 gas.
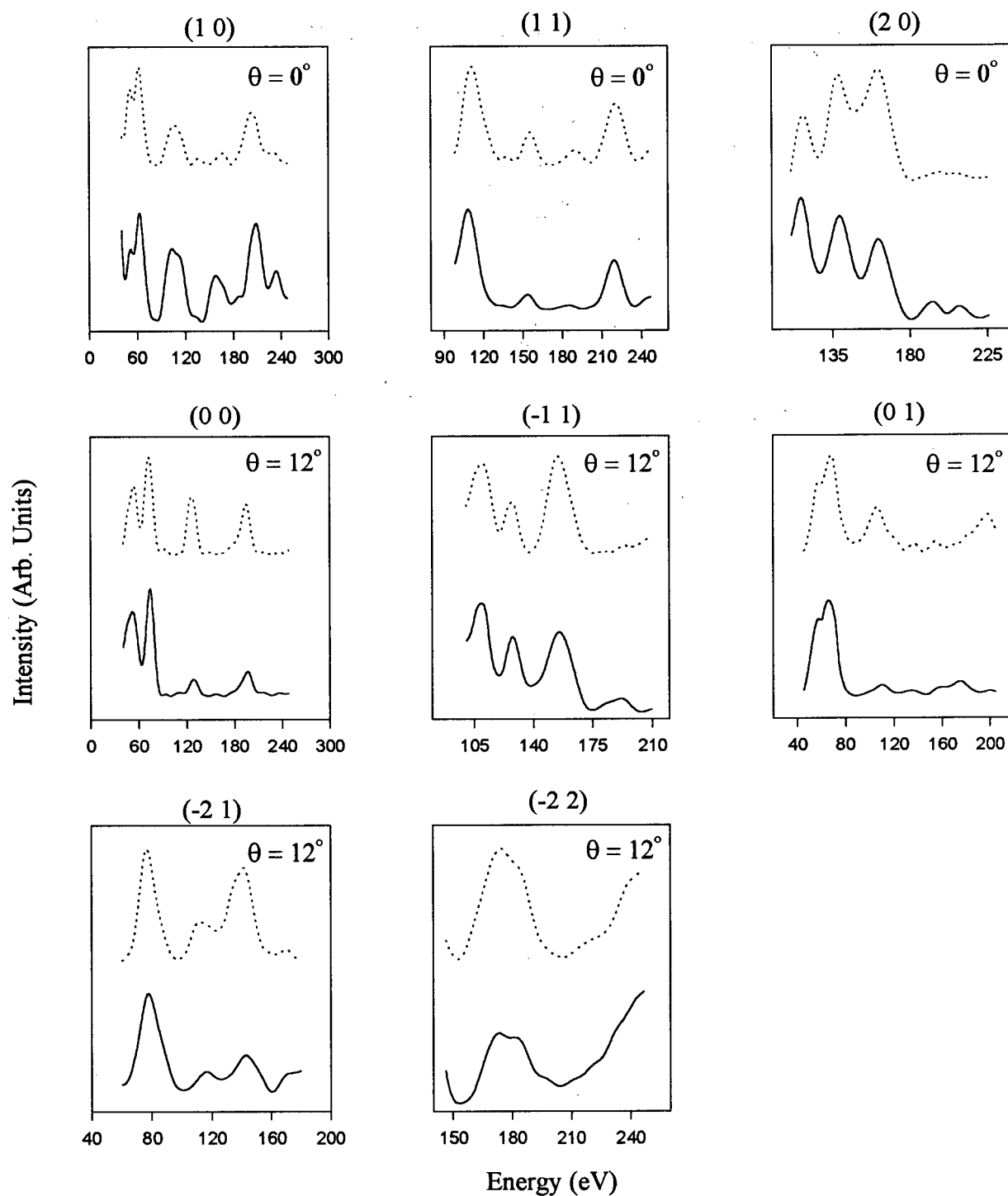
Figure 5.2   Experimental I(E) curves (dotted) for eight diffracted beams from a cleaned Zr (0001) surface and compared to those calculated (full lines) for the structural model that minimizes R_p

5.3 The Half Monolayer Structure Formed by O at the Zr(0001) Surface

5.3.1 Experimental

The cleaned and well-ordered Zr(0001) surface was exposed to high purity O_2 gas (Linde) at around 1×10^{-8} Torr with the sample held at room temperature, followed by a flash to about 220°C and then cooled back to room temperature in order to show optimal sharpness in the (2×2) LEED pattern. It was important to ensure that the heating was sufficient to order the diffraction pattern, while not encouraging significant O diffusion into the bulk [16,17]. Throughout the amount of O chemisorbed was monitored by the Auger peak-to-peak height ratio (R_o) defined by the height of the Auger peak of O at 510 eV divided by that for Zr at 92 eV. It was found that the sharpest and best developed (2×2) pattern was reached after an oxygen exposure of about 1.2 L (i.e. 2 min at 1×10^{-8} Torr), when the corresponding R_o value equals 0.38. With increasing coverage, the half-order beams disappear completely at $R_o = 0.74$, and that is taken to indicate the coverage at which the first (1×1)-O pattern is established. This corresponds to a coverage about twice that for the surface studied here, and therefore these observations appear fully consistent with the nuclear reaction analysis study of Zhang *et al.* [17].

I(E) curves were measured with the video LEED analyzer system from three independently prepared (2×2) surfaces for normal incidence. In each case, I(E) curves were measured for the three integral and five fractional beams designated (1 0), (1 1), (2 0), (1/2 0), (1/2 1/2), (1 1/2), (3/2 0) and (3/2 1/2) according to the beam notation in Figure 5.1. These separate data sets agree very closely (a representative example is shown in Figure 4.11). The total energy range available for the analysis was 950 eV.

5.3.2 Calculations

Following earlier work from this laboratory [14,15], all analyses were done for models in which O atoms occupy octahedral holes between close packed layers of zirconium. Throughout the Debye temperature for zirconium was fixed at 270 K [14], while that for oxygen (645 K) was chosen so that all vibrating atoms probed by LEED have a constant root-mean-square amplitude [114]; other non-structural parameters followed those detailed in Section 5.2.2.

Twenty six models were analyzed using TLEED and they are listed in Table 5.1 using the notation that specifies the stacking sequence of close-packed layers by the symbols ABAB ... (hcp) and ABCABC ... (fcc). The lateral positions of the O atoms are described by the same symbols in parentheses. These models can be divided into three groups:

(1) Total 0.25 ML coverage (2×2) periodicity. These models have oxygen atoms distributed in a single layer, between the first and second or between the second and third close-packed Zr layers. Of the four models considered within this category, two have the simple unreconstructed hcp arrangement for the metal, while the other two show some local fcc-type reconstruction in the vicinities of the O atoms.

(2) Total 0.5 ML coverage (2×1) periodicity. The models considered in this category are similar to those considered in group (1), except that the oxygen coverage is 0.5 ML. The latter requires the (2×1) periodicity, rather than (2×2), but equal populations of the three rotationally related domains will ensure a symmetrical (2×2) LEED pattern (Section 4.1.3).

(3) Total 0.5 ML coverage (2×2) periodicity. This category covers the possibility of two-underlayer models. In these models, each oxygen underlayer has 0.25 ML coverage with the (2×2) periodicity while the local metallic structure has either the simple hcp arrangement or is fcc

reconstructed. Note that in the model A(C)B(C')AB..., the oxygen underlayers designated C and C' are displaced laterally from one another by a unit translational vector appropriate to the Zr(0001) substrate (see Figure. 5.5 (b)).

5.3.3 Results of TLEED Analysis

TLEED calculations for the 26 models in Table 5.1 allowed variations in positions of the O atoms as well as for Zr atoms in the top few metal layers (usually four). All models have O atoms in octahedral holes, and the first reference structure for each had the Zr-Zr interlayer spacing equal to 2.66 Å when there are O atoms between the layers, and the regular bulk value of 2.57 Å otherwise. The former value was chosen to fit to the O-Zr bond length in bulk ZrO [45], where the O atoms are also 6-fold coordinate. As a comparison to the TLEED optimized R_p values given in column II of Table 5.1, values are also listed (column I) for when the close-packed layers are kept regular and flat (i.e. with metal atoms in bulk positions, and all O atoms positioned exactly half-way between the layers). It is clear that at the latter level of calculation no significant distinction can be made between the different models.

The TLEED analysis for each model type began with an optimization of the atomic coordinates perpendicular to the surface, and that was then fine-tuned by also allowing lateral displacements. The optimized R_p values are listed in column II of Table 5.1. Using Pendry's statistical estimate [132], we obtained $\Delta R_p = 0.06$ as the uncertainty in R_p (using $R_p = 0.28$ as reference). According to this criterion, the model type A(C)B(C')AB ... , with an optimized R_p value of 0.284, is clearly favored over the other models tested. By contrast, at the level of keeping the Zr layers regular and flat, as in column I of Table 5.1, it would be much harder to argue that any one particular model is convincingly better than another. Figure 5.3 compares

Table 5.1 Optimized R_p values for different models of the 0.5 ML O at Zr(0001) surface structure.

Model	I	II
Total 0.5 ML coverage (2×2) periodicity		
A(C)B(C')AB<u>A</u>[a]..	0.609	0.284
A(C)B(C)AB<u>AB</u> ..	0.628	0.415
A(C)B(A)CA<u>BA</u> ..	0.708	0.483
C(B)A(C)BA<u>BA</u>...	0.634	0.429
A(C)B(A)CA<u>BCA</u>..	0.712	0.489
AB(C)A(C)B<u>AB</u> ..	0.751	0.501
AB(A)C(B)A<u>BA</u>..	0.893	0.539
AC(B)A(C)B<u>AB</u> ..	0.785	0.485
AB(A)C(B)A<u>BCA</u>..	0.891	0.547
AB(C)A(C')B<u>AB</u> ..	0.880	0.437
Total 0.5 ML coverage (2×1) periodicity		
A(C)BAB<u>AB</u> ..	0.615	0.386
A(C)BCA<u>BA</u>..	0.720	0.460
C(B)ABA<u>BA</u> ..	0.663	0.419
A(C)BCA<u>BCA</u>..	0.723	0.455
AB(C)AB<u>AB</u> ..	0.695	0.422
AB(A)CA<u>BA</u> ..	0.799	0.513
AC(B)AB<u>AB</u> ..	0.731	0.468
AB(A)CA<u>BCA</u>..	0.804	0.520
Total 0.25 ML coverage (2×2) periodicity		
A(C)BAB<u>AB</u> ..	0.604	0.406
A(C)BCA<u>BA</u>..	0.655	0.424
C(B)ABA<u>BA</u> ..	0.675	0.435
A(C)BCA<u>BCA</u>..	0.661	0.433
AB(C)AB<u>AB</u> ..	0.701	0.451
AB(A)CA<u>BA</u> ..	0.728	0.467
AC(B)AB<u>AB</u> ..	0.740	0.490
AB(A)CA<u>BCA</u>..	0.725	0.460

Results under I are for keeping the close-packed Zr layers regular and flat with bulk interlayer spacings throughout. Those under II are for TLEED calculations which allow full relaxations in all atoms in the vicinity of the O atoms.

[a] In each case, the underlined atoms signify the beginning of the substrate (either hcp Zr when two underlined or fcc Zr when three underlined). The coordinates of all other atoms are varied in the TLEED analyses reported under II.
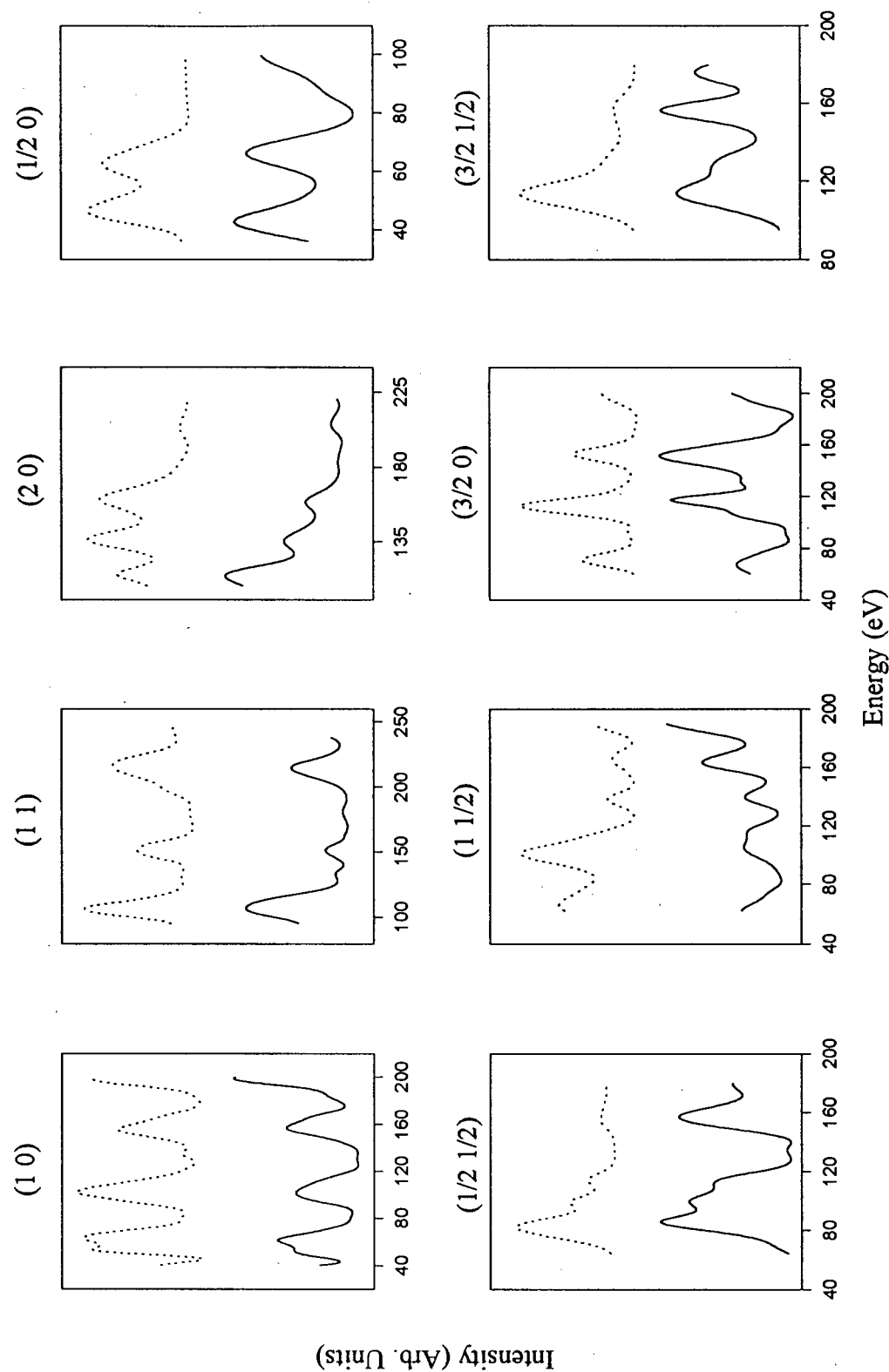
Figure 5.3   Experimental I(E) curves (dotted) for eight diffracted beams at normal incidence from the 0.5 ML O on Zr(0001) surface and compared with those calculated (full lines) for the model A(C)B(C')AB... with the best-fit geometry.

experimental I(E) curves with those calculated for the model favored by the TLEED analysis and atomic coordinates for this structure are listed in Table 5.2. The correspondence between calculated and experimental diffracted beam intensities reached in this work is at a good level. The dominant effects of the metallic relaxations are in the spectra of the fractional beams, and Figure 5.4 shows this for the beams (1/2 1/2) and (3/2 0). One additional point should be mentioned. For 25 of the 26 model types considered, the atomic coordinates were optimized over the first four metal layers, but for the favored A(C)B(C')AB.. model, the optimization was restricted to the first three metal layers only. Inclusion of the four metal layers for the favored model type appears to improve R_p by a further 0.03, although the changes in geometry then occur especially in the fourth metal layer. This reduction in R_p may not therefore be significant, and in any event a visual analysis shows that the resulting changes in the I(E) curves are small.

A pictorial representation of aspects of the optimized A(C)B(C')AB.. model is shown in Figure 5.5, and some corresponding geometrical parameters are reported in Table 5.3. In this model, the O atoms occupy octahedral holes in an unreconstructed metallic structure, with 0.25 ML between the first and second metal layers, and 0.25 ML between the second and the third metal layers. These two (2×2)-O arrays are displaced laterally from one another by an unit translational vector of the Zr(0001) substrate. A crucial feature of this model is that the O atoms induce both vertical and lateral relaxations in the three topmost Zr layers. The largest displacements are found in the second Zr layer, which is in contact with two layers of O. In this layer, the rumpling is indicated to have a magnitude of 0.11 Å and the maximum lateral atomic displacement is 0.22 Å. The first and third Zr layers are, however, much flatter, and the lateral atomic displacements in these two layers are also smaller than for the second Zr layer.

Table 5.2   Atomic coordinates in Å for the TLEED-determined structure of the surface formed by 0.5 ML of O at Zr(0001) and corresponding to the model A(C)B(C')AB..

Atomic label	X	Y	Z
Zr(1a)	−1.90	3.23	0.04
Zr(1b)	−1.79	0.00	0.02
Zr(1c)	0.94	−1.61	0.05
Zr(1d)	0.94	1.61	0.05
O(1)	0.03	0.00	1.35
Zr(2a)	−0.74	1.51	2.60
Zr(2b)	−0.74	−1.51	2.60
Zr(2c)	1.75	−3.23	2.70
Zr(2d)	2.06	0.00	2.72
O(2)	0.00	−3.23	3.95
Zr(3a)	−1.91	3.23	5.23
Zr(3b)	−1.84	0.00	5.27
Zr(3c)	1.08	−1.58	5.25
Zr(3d)	1.08	1.58	5.25
bulk repeat vector	1.8660	0.0000	2.5738[a]
	0.9330	1.6160	2.5738[b]
2D repeat vector	5.5980	−3.2320	0.0000
	0.0000	6.4640	0.0000

The z-direction is perpendicular to the surface, the x-direction is parallel to the mirror line (shown in Figure 5.5) and y-direction is parallel to $[1\bar{2}10]$.

[a] This vector connects bulk layer B to A

[b] This vector connects bulk layer A to B
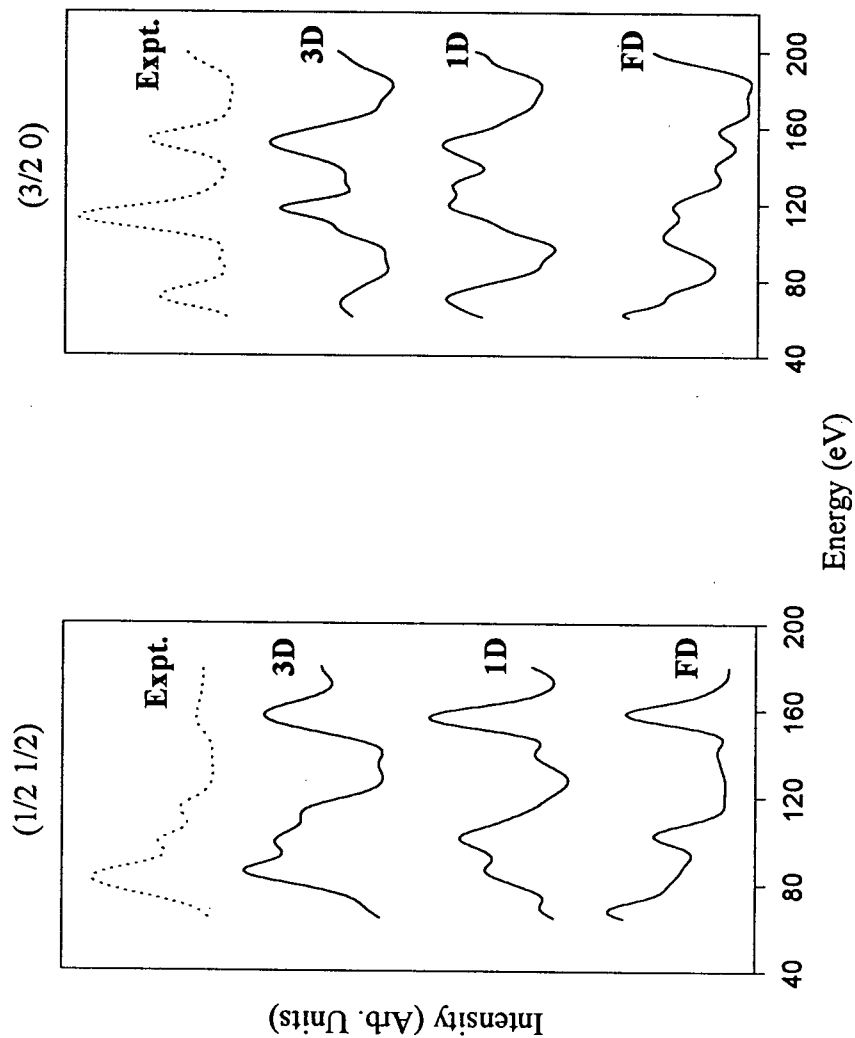
Figure 5.4   Experimental I(E) curves (dotted) for (1/2 1/2) and (3/2 0) beams compared to those calculated for the model type A(C)B(C')AB.. at three different levels of refinement. The solid curves on the bottom are calculated with close-packed Zr layers kept regular and flat; the solid lines in the middle are from a calculation which allowed the Zr atoms to displace vertically, while those on the top are from the full TLEED optimization in Zr and O coordinates with regard to both vertical and lateral displacements.
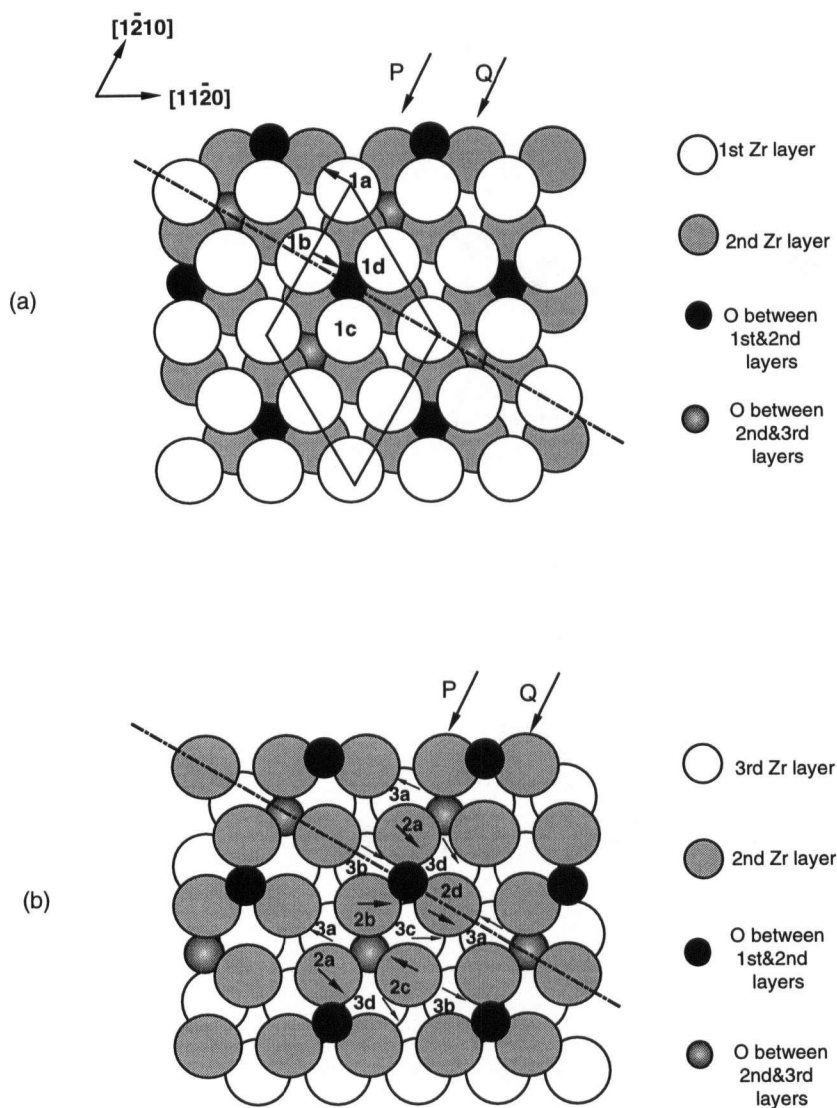
Figure 5.5 (a) Top view of the first and second Zr layers and the neighboring O atoms in the TLEED-determined model for the low-coverage O at Zr(0001) surface structure. The dash-dotted line identifies a mirror plane for this structure. Symbols 1a-1d indicates different Zr atoms within the (2×2) unit mesh for the first metal layer. The arrows indicate directions of lateral displacement for Zr atoms. In (b) the first Zr layer has been removed in order to show the second and third Zr layers. Neighboring atoms are in contact; they are shown apart in this figure simply to demonstrate the positions of deeper atoms.

Table 5.3   Some TLEED optimized structural parameters (in Å) for the model A(C)B(C')AB..

	Center-of-mass-spacing	Lateral displacement [a]	
Zr (2P) - Zr (2Q)[b]	0.11	1b	0.08
Zr*(1) - O(1)	1.31	2a, 2b	0.22
Zr*(2) - O(1)	1.31	2c	0.12
Zr*(2) - O(2)	1.30	2d	0.19
Zr*(3) - O(2)	1.30	3c, 3d	0.15
Zr*(3) - Zr(4)	2.55		

[a] Figure. 5.5 identifies atom notation and direction of displacement (note that unit mesh side for surface layer in Zr(0001) is 3.23 Å).

[b] Corrugation in second Zr layer i.e. between atoms in rows P and Q (note bulk Zr(0001) spacing is 2.57 Å).

Zr*(1), Zr*(2)... represent averages over vertical coordinates for atoms in first, second... Zr layers.

5.3.4 Discussion

That oxygen incorporates into the zirconium structure is consistent with that metal being a strongly gettering material. The state of O dissolved in bulk Zr at infinite dilution is believed to correspond to the thermodynamically most stable form known for that element [148], and indeed, at higher solubility, O dissolves to give the approximately Zr_3O interstitial phase [149] in which the Zr atoms retain their basic bulk positions while the O atoms occupy octahedral holes. Therefore, it is perhaps not surprising that the surface structure formed by 0.5 ML of O atoms should retain the hcp form for the metal. Additionally, octahedral incorporation is most probable because it can occur with only a small change in the Zr interlayer spacing. For example, the Zr-Zr interlayer spacing in bulk ZrO (sodium chloride lattice with cell constant 4.60 Å) [45] corresponds to only a 4.1% expansion over that in metallic Zr.

Another feature that is likely to have a role in determining the details of the surface structure concerns the O-Zr bond ionicity, which is estimated at 67% according to the Pauling electronegativity difference [150]. The O-Zr bonds are likely to have a highly polar character, and any Zr atoms that bond directly to O will therefore have a partial positive charge. An implication is that a relatively high charge would be developed at the metal surface when a strongly electronegative atom like O is absorbed immediately below. Indeed it is now well recognized that the large net charges that may be expected at polar surfaces of compound materials commonly induce relaxations or reconstructions to lower energy states [151,152]. In the context here, a lower energy state may be provided by O between the second and the third Zr layers, since that would reduce the surface charge expected if all O is between the first and second metal layers. This possibility has been supported by first principles calculations of Yamamoto *et al.* [153] which show that the octahedral hole sites between the second and third Zr

layers provide the energetically most favorable sites for the Zr(0001)-(1×1)-O surface structure at 1 ML coverage. However, in our analysis for 0.5 ML total coverage, the two-underlayer model is favored over the one-underlayer model (i.e. with 2×1-type translational symmetry for 0.5 ML). Two factors may be involved. In the first, with all 0.5 ML oxygen atoms distributed in a single layer, O-O replusions will be larger than when they are distributed in the two layers. Secondly, the perturbation on the metal structure could be larger than in the former case, and an indication of this is provided by LEED studies for the O-Ru(0001) system where the metallic relaxations are smaller in the 0.25 ML (2×2) phase than in the 0.5 ML (2×1) phase [154]. The O-O repulsion argument should favor A(C)B(C')AB.. over A(C)B(C)AB..; consistently the TLEED analysis shows (Table 5.1) a much larger optimized R_p value for the second model.

In the favored model, the 0.5 ML of oxygen is distributed in two O layers, each of 0.25 ML, and three metal layers are in direct contact with the O atoms. Within the second metal layer, adjacent rows of Zr atoms parallel to $[1\bar{2}10]$ are different (see Figure 5.5(b)). In the row type designated P, each Zr atom bonds to two O atoms, one above and one below the second Zr layer, while in row Q, each Zr atom bonds to just one O atom. Furthermore, within this latter row, adjacent Zr atoms also differ because one bonds to a first layer O atom while the other bonds to a second layer O atom. The relaxations in the metallic structure depend on the reduction in symmetry, and the LEED analysis here shows larger layer bucklings and lateral displacements in the second Zr layer compared with those in the first and third Zr layers (Table 5.4). The larger atomic displacements in the second layer appear to correlate with the larger effective charges in that layer. With the pure ionic description for illustrative purposes only, all six Zr atoms neighboring an octahedrally bonded O would be allocated a charge +1/3. These contributions

Table 5.4. Layer bucklings and average lateral displacements (in Å) for the first three Zr layers in the TLEED-determined model for the low-coverage O on Zr(0001) surface structure.

Layer	Buckling	Average lateral displacement	Effective layer charge in unit mesh
1	0.01	0.04	+1
2	0.11	0.19	+2
3	0.05	0.09	+1

These values are compared with the effective layer charge per unit mesh assuming a pure ionic model for the O-Zr bonding.

sum unequally through the surface structure so that, per (2×2) unit mesh, the first and third Zr layer atoms have charges +1/3 (three) and 0 (one), while the second Zr layer has charges +2/3 (two) and +1/3 (two).

Overall the structure indicated by TLEED appears to satisfy the requirements of O-Zr bonding without too seriously disrupting the Zr-Zr bonding. Basically O seems able to incorporate into the metallic structure with only relatively small changes to the latter. For example, the center of mass spacings between the first and second Zr layers (2.62 Å) and between the second and third Zr layers (2.60 Å) have just small increases over the value (2.57 Å) appropriate to the bulk metal. The average O-Zr bond lengths for the first three Zr layers are: 2.26 Å (Zr(1) - O(1)), 2.24 Å (Zr(2) - O(1)), 2.26 Å (Zr(2) - O(2)) and 2.34 Å (Zr(3) - O(2)). The average O-Zr (second layer) bond length is plausibly shorter than that involving the third metal layer because of the larger effective charge in the second layer. The O-Zr (first layer) and O-Zr (third layer) bond lengths are expected to be equivalent as far as electrostatic effects alone are considered. However, the Zr atoms in the first layer have a smaller number of nearest neighbor metal atoms (CN=9) than the Zr atoms in the third layer (CN=12), and that may be a factor in the O-Zr (first layer) length being shorter than that for O-Zr (third layer).

Certainly the vertical and lateral displacements indicated for the metal atoms can be appreciable (e.g. in the second Zr layer as reported in Table 5.2), but the structure seems to adapt to maintain distances which on average appear reasonable. For example, the second layer Zr atoms may be expected to form essentially equal bonding with O atoms above and below, and this is consistent with the TLEED analysis insofar as the average O-Zr bond lengths are closely similar. Also, even though the structure has substantial relaxations, lateral displacements of O atoms from the octahedral hole positions are indicated to be less than 0.03 Å.

Physically, as some atoms move toward one another, other atoms may need to move away, and such tendencies appear to have been picked up by the TLEED analysis. For example, Figure. 5.5(b) shows for the second Zr layer that as atoms 2a and 2b move in atom 2d is displaced out. Likewise as atoms 2b and 2a move apart, room is made for atom 2c to move in toward the center of the octahedral site. Moreover, displacements of Zr atoms in one layer may require further displacements in neighboring layers. For example, as atoms 3c, 3d and 3a move toward each other laterally, atom 2d is lifted up in a vertical sense. A cooperative two-layer effect is seen within a cluster of six atoms: as atoms 2c, 2b and 2a displace together, the atoms 3c, 3d and 3a are pushed away. Similar examples are identifiable in the first layer displacements. Overall such trends appear to have broad plausibility, even though it may not yet be possible to consider some individual details as significant.

In summary, the present LEED crystallography study of a structure, formed by 0.5 ML of O at Zr(0001) surface, favors a novel type of structural model which has 0.25 ML of O at octahedral hole sites in (2×2) arrays both between the first and second metal layers, and between the second and third metal layers. These O arrays are displaced laterally from one another by a unit translational vector parallel to the Zr(0001) substrate. This model is intrinsically different from the simple one-underlayer model, with (2×1) translational symmetry, suggested by Zhang *et al.* [17], although our model also involves three rotationally-related domains. Inevitably factors associated with kinetics are involved to some degree in the existence of this ordered 0.5 ML structure. The A(C)B(C')AB.. model is favored in our case because it gives the best correspondence between experimental and calculated I(E) curves that we have been able to obtain for this system.

The long-term difficulty in getting good structural determinations for the O on Zr(0001) system appears as a consequence of the vertical and lateral relaxations that occur in the metallic structure around the incorporated O atoms. These relaxations are most significant in the second metal layer, which is in contact with two layers of O. The hole sites show some distortion in the vicinity of each 6-coordinated O atom, but the overall average O-Zr bond length of 2.28 Å is close to the value 2.30 Å indicated for the same coordination in bulk ZrO [45].

Chapter 6: LEED Analyses of Structures Formed by 1 ML and 2 ML of O at Zr(0001) Surface

6.1 Introduction

The interaction of the (0001) surface of zirconium with oxygen for exposures in the range to about 15 L (1 Langmuir = 10^{-6} Torr.s) has shown some interesting trends. For example in LEED, this system initially manifests a (2×2)-type diffraction pattern; the point at which the half-order beams are both sharpest and most intense in the pattern now appears to correspond to a 0.5 ML surface structure for which the structural details have been reported in Chapter 5. Prior to that work, the form of that structure had provided a bit of a mystery, and the same can be said for other structures formed at higher O coverages. For example, the half-order fractional beams extinguish at about 1 ML to show a (1×1)-type LEED pattern [17], but the earlier LEED analysis [15] could not convincingly distinguish between the model involving a single O underlayer and those with deeper O incorporation, although it pointed out that this is also an underlayer structure with O atoms incorporated into octahedral hole sites. The (1×1)-type LEED pattern remains at higher oxygen coverages, but the measured I(E) curves for various diffracted beams indicate the establishment of a new surface structure for a coverage of about 2 ML [155]. AES shows that new structure associated with the Zr(MNV) transition develops at 140 eV (in addition to that at 147 eV) as the oxidation proceeds [9,156], and Zhang *et al.* concluded that the nucleation of oxide starts at oxygen coverages above 1 ML [156]. For the lower coverages, the work function change $\Delta\phi$ is negative, and reaches a minimum at about 0.5 ML, but from there $\Delta\phi$ increases with increasing coverage, and the work function returns to the value of the clean surface at around 2 ML [157]. Structural determination has not been made before for the surface formed by 2 ML of O at

Zr(0001). As part of a program to probe the evolution of surface structure with increasing coverage, we have undertaken studies for these two further surface structures formed by O on Zr(0001), and that provides the subject for the current chapter. In addition, the structural features obtained will be compared with those found for the corresponding 0.5 ML surface, reported in Chapter 5. The overall aim is to contribute some initial understanding for the evolution of structure in this surface system.

6.2 Structure Formed by 1 ML of O at Zr(0001) Surface

6.2.1 Experimental

The main experimental approaches follow the procedures defined in Chapter 5. The surface with 1 ML of O at Zr(0001) was prepared by exposing at room temperature the cleaned and ordered Zr(0001) surface to about 3.2 L of high-purity O_2 gas (Linde). On flashing to 220°C, and cooling back to room temperature, this surface showed a (1×1) LEED pattern and an Auger ratio R_o equal to 0.74, which is approximately double that for the best (2×2)-type pattern (R_o = 0.38). Furthermore, in the Auger spectrum of zirconium (Figure 6.1 (b)), a new feature at 141 eV started to appear when the half-order beams were just extinguished and this also helped to identify the formation of the first (1×1) surface. I(E) curves from two independent preparations of this surface were measured for the beams (1 0), (1 1) and (2 0) at normal incidence, and for the beams (0 0), (-1 1), (0 1), (-2 1), (-2 0) and (-2 2) at the off-normal direction corresponding to the $\left[1\bar{1}20\right]$ azimuth with θ =14°. These independently measured sets agreed closely; the total energy range of the data available for the structural analysis was 1297 eV.
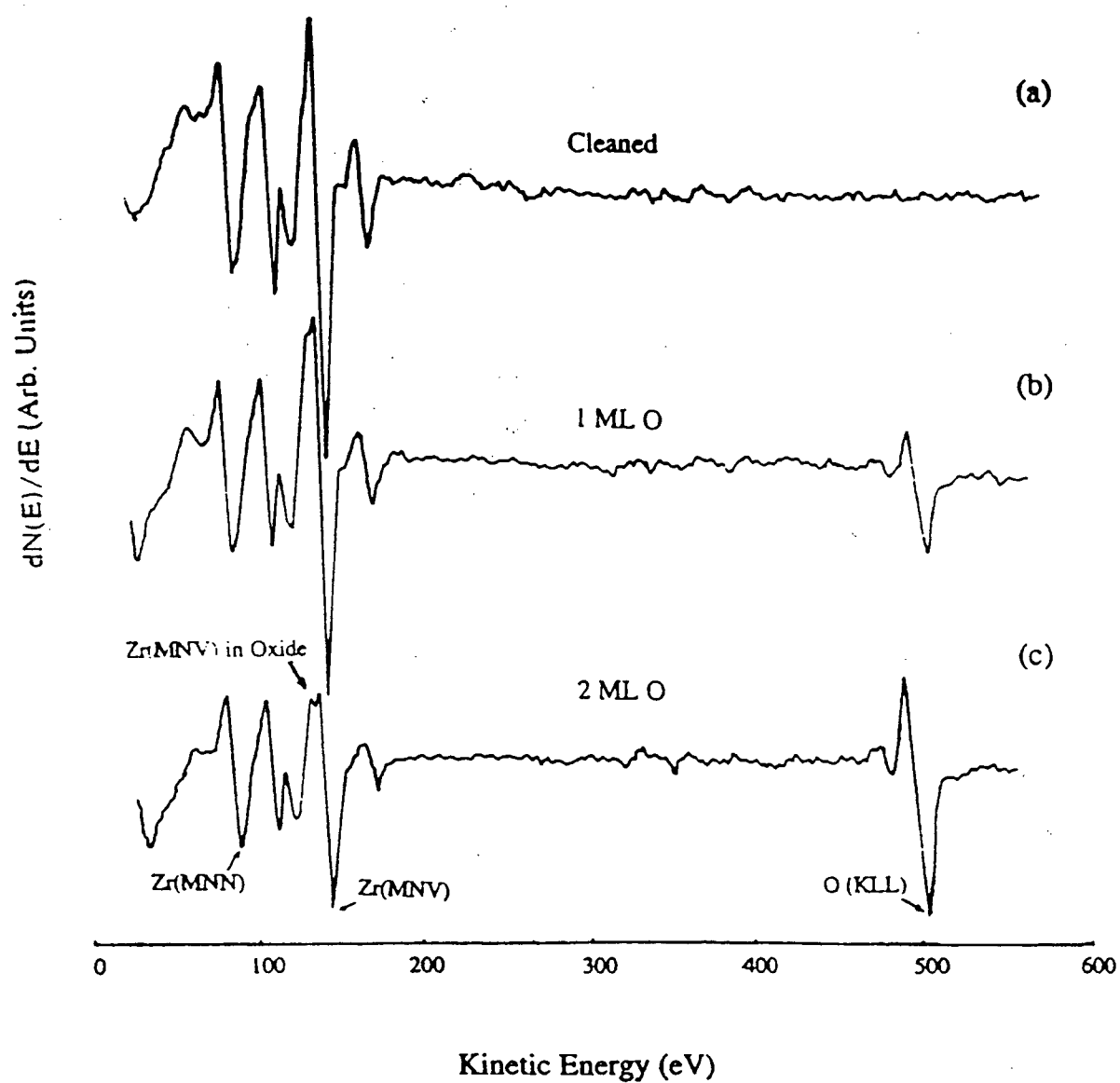
Figure 6.1   Auger electron spectra from Zr(0001) surfaces when: (a) cleaned, (b) containing 1 ML of O and (c) containing 2 ML of O.

6.2.2 Calculations

The main computational methods, and non-structural parameters, used here are exactly those defined in Chapter 5. But one new feature arose because of a need to investigate structural models where O occupies octahedral holes in the Zr structure on a statistical, rather than strictly ordered, basis. Such situations are treated with the average t-matrix approximation (ATA) [158], which follows successful uses of this approximation for surface alloy systems, where lattice sites are randomly occupied [159]. For an example, in a disordered bimetallic alloy, where the two constituents (species A and B) are randomly distributed on the lattice sites, this approximation assumes each site has an averaged scattering amplitude weighted by the respective concentration for each species:

$$t_{avg} = t_A \times C_A + t_B \times C_B \tag{6.1}$$

where t_A and t_B refer to the scattering amplitudes of the pure metal atoms, and C_A and C_B are the concentrations of the species A and B in that layer. In our context, the ATA approach amounts to assigning each octahedral hole site in a particular O layer a scattering amplitude weighted according to the fraction of sites occupied in that layer. For example, taking a layer where half of the octahedral holes are statistically occupied by O atoms, while the other half are empty, Eq. (6.1) becomes

$$t_{avg} = t \times 0.5 + t \times 0 = t/2 \tag{6.2}$$

where t is the O atom scattering amplitude. With this approximation, one such half-monolayer is represented by a full (1×1) array of "half atoms", with the scattering amplitude of these pseudo atoms being as $t/2$ (an average of the "full atom" scattering amplitude t and the nil scattering by the absent atoms).

Twenty three model types (specified in Table 6.1) were tested to cover a range of possibilities for the O structure, including adsorption on top of the Zr(0001) surface, and atomic incorporation into octahedral or tetrahedral holes below the surface. A range of coverage was also included. As in Chapter 5, the subscripts in the notation $A(C_{0.5})B(C_{0.5})AB..$, for example, indicate that O atoms are distributed randomly to occupy half the octahedral holes between the first and second metal layers, and another half between the second and third Zr layers. Scattering by those O atoms is treated with the ATA approach.

6.2.3 Results and Discussion

The TLEED analysis for each model type allowed variations in vertical positions of O atoms as well as for Zr atoms in the top few metal layers (usually four). The first reference structure for each model had the Zr-Zr interlayer spacing equal to 2.66 Å when there are O atoms between these layers in octahedral holes, but the bulk value of 2.57 Å otherwise. However this spacing was increased to 3.37 Å for the initial reference structures of models with O atoms in tetrahedral holes. These values were chosen to fit to the O-Zr bond lengths measured in bulk ZrO (2.30 Å) [45] and in cubic ZrO_2 (2.20 Å) [160], where the O coordination numbers are also 6 and 4 respectively. For the models with O adsorbed above the Zr(0001) surface, the corresponding bond length was set at 2.09 Å in the initial reference structure; this value was chosen by parametrizing the bond length - bond order relation [161]

$$r = r_0 - 0.85 \log s \tag{6.3}$$

to the O-Zr bond length in ZrO_2. Eq. (6.3) has proven useful for rationalizing trends in bond lengths in both bulk and surface structures [162]; in the general context r can be seen as the X-M bond length for bond order s, while r_0 is the corresponding single-bond distance. In practice, s is

Table 6.1   Optimized R_p values from TLEED analyses for different models of the surface formed by absorption of around 1 ML of O at Zr(0001).

Model	R_p
A(C)BAB<u>AB</u>..	0.433
C(B)ABA<u>BA</u>..	0.552
A(B)CBA<u>BA</u>..	0.561
AB(C)AB<u>AB</u>..	0.392
AC(B)AB<u>AB</u>..	0.447
(B)ABAB<u>AB</u>..	0.482
(C)ABAB<u>AB</u>..	0.501
A(B$_t$)BAB<u>AB</u>..[*]	0.655
A(A$_t$)BAB<u>AB</u>..	0.610
A(C$_{0.5}$)B(C$_{0.5}$)AB<u>AB</u>..	0.267
C(B$_{0.5}$)A(C$_{0.5}$)BA<u>BA</u>..	0.406
A(C)B(C)AB<u>AB</u>..	0.472
C(B)A(C)BA<u>BA</u>..	0.523
(C)A(C)BAB<u>AB</u>..	0.615
(B)C(A)BAB<u>AB</u>..	0.655
(A)B(C)ABA<u>AB</u>..	0.627
(C)B(A$_t$)ABA<u>AB</u>..	0.526
(C)B(B$_t$)ABA<u>BA</u>..	0.591
(A)B(A$_t$)ABA<u>BA</u>..	0.530
(A)B(B$_t$)ABA<u>BA</u>..	0.558
A(B$_t$)(A$_t$)BA<u>BA</u>..	0.673
A(B$_t$)B(C)AB<u>AB</u>..	0.526
A(A$_t$)B(C)AB<u>AB</u>..	0.550

[*]The subscript "t" indicates that O atoms incorporate into tetrahedral holes.

expressed as the valency of X (2 for O) divided by the number of neighboring M atoms (e.g. 4 for O in a tetrahedral hole).

The best-fit R_p value for each model type is listed in Table 6.1. The correspondence between the experimental and calculated I(E) curves was always poor for models involving either overlayer adsorption or absorption into tetrahedral holes, and this confirms the previous experience [15]. Also models corresponding to total O coverages greater than 1 ML had minimized values of R_p 0.472 or greater. The lowest R_p value (0.267) was obtained for the model $A(C_{0.5})B(C_{0.5})AB..$, and the next lowest value of 0.392 applied for AB(C)AB... Using Pendry's statistical estimate [132], the variance in the lowest minimum in R_p is indicated to equal to 0.05; the latter value gives an uncertainty in the minimized value of R_p due to random fluctuations. This is sufficiently small to support the view that the model $A(C_{0.5})B(C_{0.5})AB..$ is clearly favored over the other models tested. Figure 6.2 compares the measured I(E) curves with those calculated for the best-fit model. The correspondence reached appears at a good level, and Table 6.2 includes the optimized interlayer spacings for this structure.

The average separation between the first and the second Zr layers (2.65 Å), and between the second and third Zr layers (2.63 Å), for the 1 ML structure match to within 0.02 Å of the center-of-mass values for the 0.5 ML case (Table 6.2). Equally, in both structures, the metal-metal spacing below the third layer are essentially unchanged from the bulk spacings, an observation that may point to no significant O being present in those regions for the preparation procedures used in this work. For the 1 ML case, the O-Zr bond distance is estimated to equal 2.28 Å, in satisfactory correspondence with the value of 2.30 Å in bulk ZrO. Incidentally, the interlayer spacings given in Table 6.2 for the 1 ML case, using the average t-matrix approximation, are only slightly altered (e.g. by 0.02 Å) if the O atoms are neglected altogether.
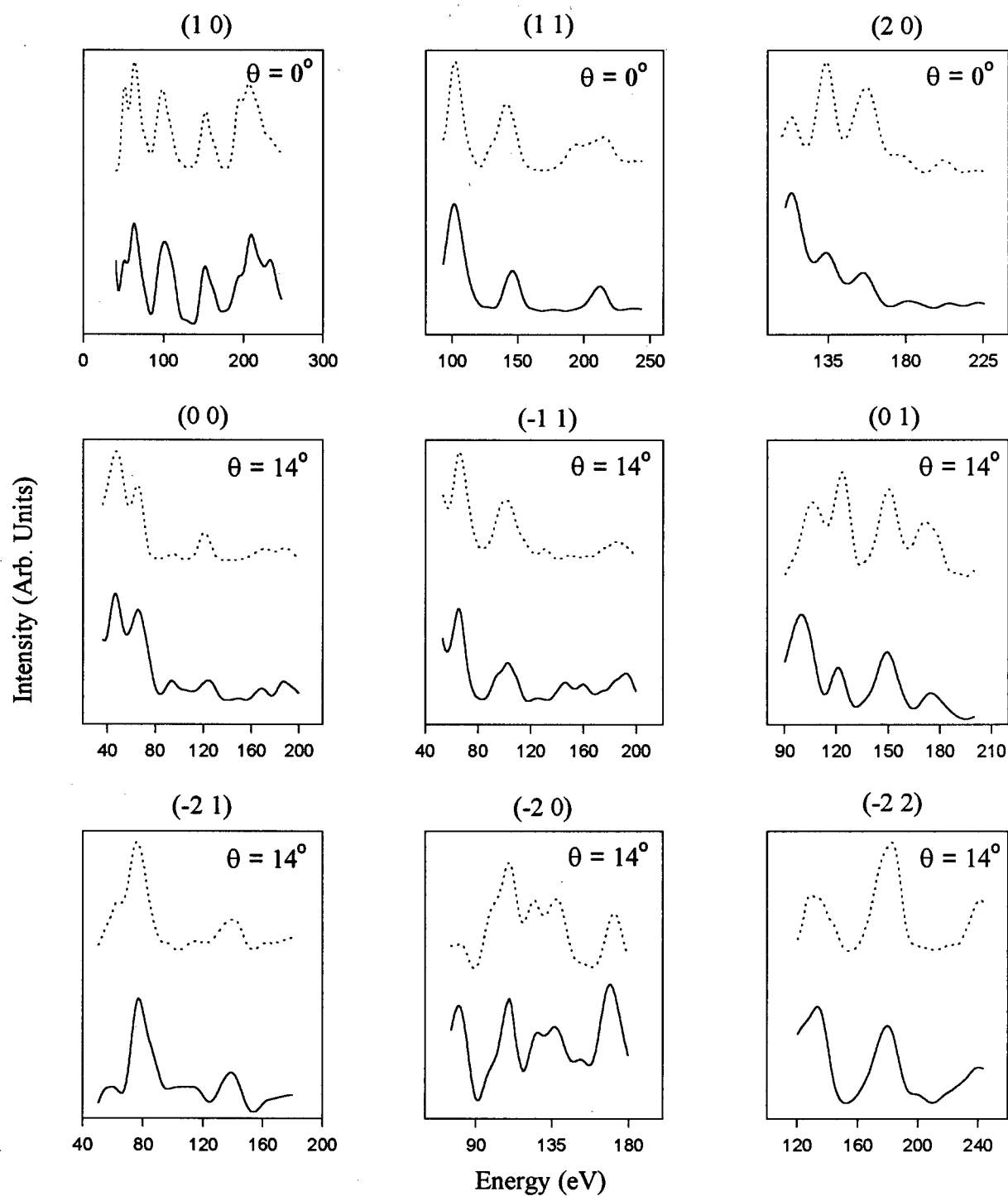
Figure 6.2　　Experimental I(E) curves (dotted) for eight diffracted beams from the 1 ML O on Zr(0001) surface and compared to those calculated (full lines) for the model $A(C_{0.5})B(C_{0.5})AB..$

Table 6.2   Comparative features for Zr(0001) surfaces when cleaned, and when containing 0.5 ML, 1 ML and 2 ML of O.

	Center-of-mass-spacing (Å)				O-Zr Bond Length (Å)		Bulk Analogy
	Zr(1) - Zr(2)	Zr(2) - Zr(3)	Zr(3) - Zr(4)	Zr(4) - Zr(5)			
Clean	2.53	2.58	2.57	2.57	–		–
0.5 ML	2.62	2.60	2.55	2.57	2.28	(CN = 6)	ZrO
1 ML	2.65	2.63	2.58	2.57	2.28	(CN = 6)	ZrO
2 ML	3.44	2.56	2.58	2.57	2.22 (CN = 4) 2.07 (CN = 3)		Cubic ZrO_2

This observation emphasizes the importance of the stronger-scattering atomic species in determining the measured I(E) curves. The similarity in the conclusions for the half and one monolayer structures have interest also since information for the latter was obtained entirely from integral diffracted beams, whereas in the former case the fractional beams have a dominant role in the analysis.

The 1 ML surface studied in this work was prepared by directly exposing the clean Zr(0001) surface to the appropriate amount of O_2, although the same basic structure, as judged by the constant I(E) curves, can be formed by exposing the 0.5 ML (2×2)-surface to more oxygen (although the latter approach tends to yield a higher background with less sharp diffracted beams). This whole evidence therefore suggests that the formation of the 1 ML structure at the O/Zr(0001) surface has evolved smoothly from the 0.5 ML structure. There is no support for the possibility that the increase in coverage has resulted in the O atoms compressing into a one-monolayer underlayer, for example the model AB(C)AB.. where O atoms fill all octahedral holes between the second and third metal layers, which received some support in the calculations of Yamamoto *et al.* [153].

In summary, the present LEED crystallographic study for the 1 ML structure formed by O at the Zr (0001) surface indicates a structural model where a half monolayer of O is distributed randomly over the octahedral holes between the first and second metal layers, and a further half monolayer resides between the second and third Zr layers. For a number of years there have been suggestions that some higher-coverage systems that show (1x1)-type LEED patterns may involve disordered arrangements of the adsorbing species [163], and the example here appears to provide direct support. However, with the lack of complete surface order, the diffraction analysis used in this work is not able to detail the precise local structure for the Zr positions in the immediate

vicinity of the randomly occupied octahedral hole sites. Nor indeed can we rule out some degree of unequal sharing of O between the top two interlayer spacings.

6.3 Structure Formed by 2 ML O at Zr(0001) Surface

6.3.1. Experimental

The main experimental approaches used followed those defined in Chapter 5. Surfaces with increasing O coverage were prepared by exposing the cleaned Zr(0001) surface to different amounts of O_2 (in the range 4-15 L), flashing to 220°C, and then cooling back to room temperature when Auger spectra were assessed. I(E) curves were measured for diffracted beams from surfaces for which no extraneous impurites could be detected with the cylindrical mirror analyzer, and for which the diffraction pattern indicated the maximum level of order obtainable. LEED patterns for the higher-coverage (1×1) surfaces showed increased background as well as less sharp spots, indicative of lower levels of surface order compared, for example, with the 0.5 ML case, but the degree of order was still considered adequate for a structural analysis. The Auger ratio R_o (defined as the peak-to-peak height of the O Auger peak at 510 eV divided by that for Zr at 92 eV) was used to monitor the O coverage in this work, and to relate to coverages applying in our earlier studies on the O/Zr(0001) system.

Figure 6.3 reports a sequence of I(E) curves measured at normal incidence for the (1 1) beam as the O coverage is increased beyond that for the 1 ML surface (characterized by $R_o = 0.74$). A new structural feature is a peak at 120 eV which grows as the O coverage increases. This peak is maximized at about $R_o = 1.58$, at which value the I(E) curve appears essentially constant as R_o increases further. Given that this value is approximately twice that for the 1 ML surface (previously guided by NRA and peak-to-peak measurements in AES [17]), for the purposes of the present study
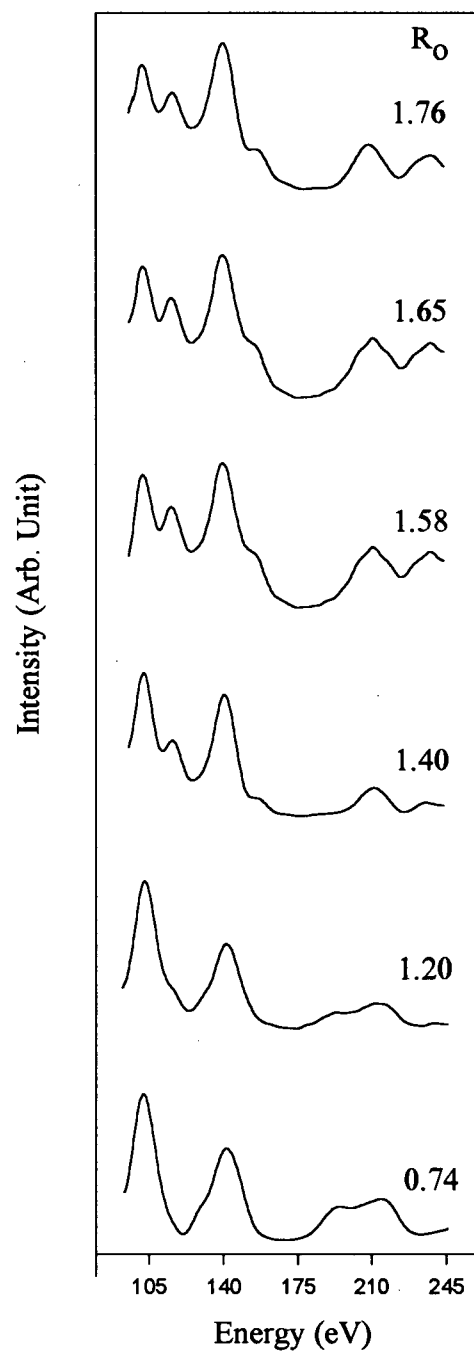
Figure 6.3   Evolution with increasing R_o value for I(E) curves measured for (1 1) beam at normal incidence from O/Zr(0001) system.

we take $R_o = 1.58$ to be indicative of the surface with a total O coverage of 2 ML. For this surface, two independent sets of I(E) curves were measured with the video LEED analyzer system for the (1 0), (1 1) and (2 0) beams at normal incidence, and for the six beams designated (0 0), (-1 1), (0 1), (2 1), (-2 0) and (-2 2) at an off-normal direction of incidence (specified by the polar angle (θ) equalling 16° with the azimuthal direction parallel to [11$\overline{2}$0]). These sets agreed closely and provided the intensity data for the structural analysis; the total energy range available was 1220 eV.

6.3.2 Structural Analysis

That the basic structure for the 2 ML O/Zr(0001) surface is likely to be different from those at 0.5 and 1 ML is suggested by the I(E) curves measured at normal incidence, for which comparative data are shown in Figure 6.4 for three integral beams. Visual analysis indicates close similarities for the (2×2) and initial (1×1) surfaces, whereas changes are apparent for the higher-coverage (1×1) surface; for example, with increase in coverage beyond the 1 ML situation, the peak at 114 eV disappears in the (2 0) curve while, as noted above, a new feature emerges at 120 eV in the (1 1) beam. In spite of this indication, a wide range of model types was still investigated for the 2 ML surface, as indicated by the 30 entries in Table 6.3. Consideration was given to different combinations of O adsorbing into overlayer sites as well as incorporating into interstitial octahedral and tetrahedral holes; also some examples were allowed for models with greater than 2 ML coverage. Throughout the computational details and non-structural parameters used were those detailed earlier for the lower coverage O/Zr(0001) systems.

The TLEED analysis for each model type allowed variations in vertical positions of O atoms as well as Zr atoms in the top few metal layers (usually four). The Zr-Zr interlayer spacings in the first reference structure of each model were those defined in Section 6.2.3. Table 6.3 lists values of
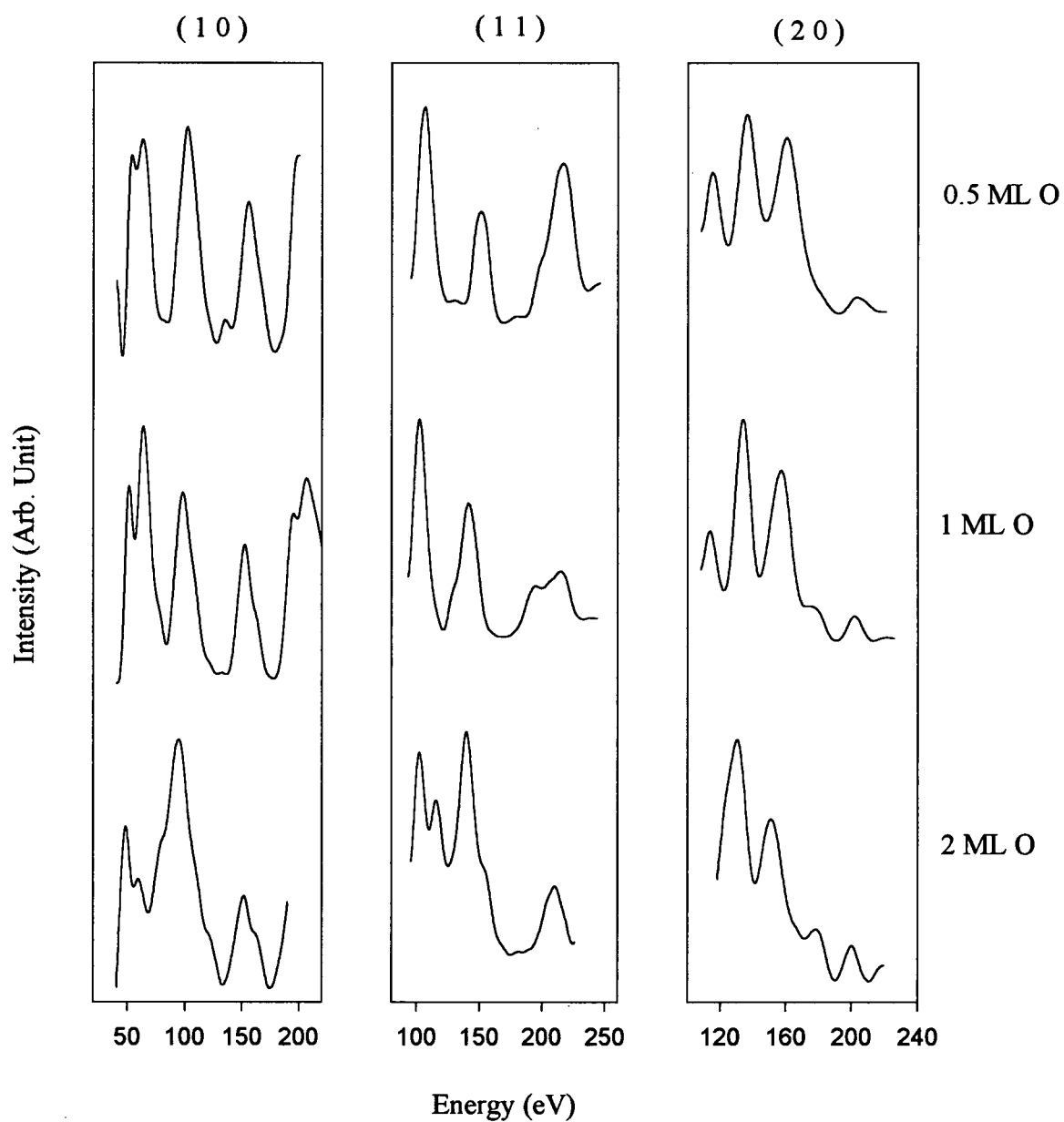
Figure 6.4   I(E) curves measured for (1 0), (1 1) and (2 0) beams at normal incidence for three

Zr(0001) surfaces containing O: (2×2) at 0.5 ML (top), (1×1) at 1 ML (middle)

and (1×1) at 2 ML (bottom).

Table 6.3   Optimized R_p values from TLEED analyses for different models of (1×1) structure formed by the incorporation of around 2 ML of O at the Zr(0001) surface.

Model	R_p
A(C)B(C)AB<u>AB</u>..	0.486
A(C)B(C)A(C)B<u>AB</u>..	0.540
A(C)B(A)C(B)A<u>BA</u>..	0.586
A(C$_{0.5}$)B(C$_{0.5}$)A(C$_{0.5}$)B(C$_{0.5}$)A<u>BA</u>..	0.452
C(B)A(C)BA<u>BA</u>..	0.605
(C)A(C)BAB<u>AB</u>..	0.595
(A)B(C)ABA<u>BA</u>..	0.450
(B)C(A)BAB<u>AB</u>..	0.502
(A)C(A)BAB<u>AB</u>..	0.483
(C)A(C)B(C)AB<u>AB</u>..	0.623
(A)B(C)A(C)B<u>AB</u>..	0.516
A(B$_t$)(A$_t$)BAB<u>AB</u>..	0.433
A(B$_t$)B(A$_t$)AB<u>AB</u>..	0.538
A(A$_t$)B(B$_t$)AB<u>AB</u>..	0.552
A(B$_t$)B(B$_t$)AB<u>AB</u>..	0.497
A(A$_t$)B(A$_t$)AB<u>AB</u>..	0.510
A(B$_t$)(A$_t$)B(A$_t$)(B$_t$)A<u>BA</u>..	0.561
A(B$_t$)A(A$_t$)B(C)A<u>BA</u>..	0.502
(C)B(A$_t$)ABA<u>BA</u>..	0.278
(A)B(B$_t$)ABA<u>BA</u>..	0.409
(C)B(B$_t$)ABA<u>BA</u>..	0.395
(A)B(A$_t$)ABA<u>BA</u>..	0.459
A(B$_t$)B(C)AB<u>AB</u>..	0.548
A(A$_t$)B(C)AB<u>AB</u>..	0.550
A(C)B(B$_t$)AB<u>AB</u>..	0.570
A(C)B(A$_t$)AB<u>AB</u>..	0.531
(A)B(A$_t$)A(C)BA<u>BA</u>..	0.386
(A)B(B$_t$)A(C)BA<u>BA</u>..	0.430
(C)B(A$_t$)A(C)BA<u>BA</u>..	0.405
(C)B(B$_t$)A(C)BA<u>BA</u>..	0.422

R_P which have been optimized for each model type. Using Pendry's statistical estimate [132], we obtain var R_p = 0.05 as the range of uncertainty on R_p (using R_p = 0.27 as reference). According to this criterion, the model (C)B(A$_t$)AB.., with an optimized R_p value of 0.278, is clearly favored over all other models tested. Figure 6.5 reports I(E) curves for the nine diffracted beams from experiment and from calculation for the optimized model; the match generally appears satisfactory. The atomic coordinates for the optimized structure are listed in Table 6.4. This structure has two layers of O: one forms an overlayer where each O atom bonds to a metal site of three-fold coordination (hollow type with local fcc-type stacking sequence), while the other layer has O atoms in tetrahedral hole sites. The stacking sequence corresponds to the first three layers of anion-terminated cubic ZrO_2 superimposed on the regular (hcp) zirconium structure. This surface form of ZrO_2 appears laterally compressed by about 10% compared with the known (metastable) bulk form with the fluorite lattice structure. The top five interlayer spacings are O(1)-Zr(1) 0.89 Å, Zr(1)-O(2) 1.22 Å, O(2)-Zr(2) 2.22 Å, Zr(2)-Zr(3) 2.56 Å, and Zr(3)-Zr(4) 2.58 Å. The latter two are not believed to be significantly different from the Zr(0001) bulk value of 2.57 Å, although uncertainties in the first three values are estimated to equal ±0.03, ±0.03, ±0.04 Å respectively according to the criterion discussed by Anderson *et al.* [133]. The center-of-mass spacings for first four Zr layers are summarized in Table 6.2 and compared to those of the corresponding 0.5 and 1 ML surfaces. A particularly significant feature here is the expansion in the first Zr-Zr interlayer spacing to 3.44 Å as a result of some O atoms going into tetrahedral hole sites. The O-Zr bond lengths in this surface structure are indicated to be 2.07 Å for the overlayer O atoms and 2.22 Å for those in the hole sites (with the distances from each tetrahedral O atom to the neighboring upper and lower Zr atoms being essentially equal).
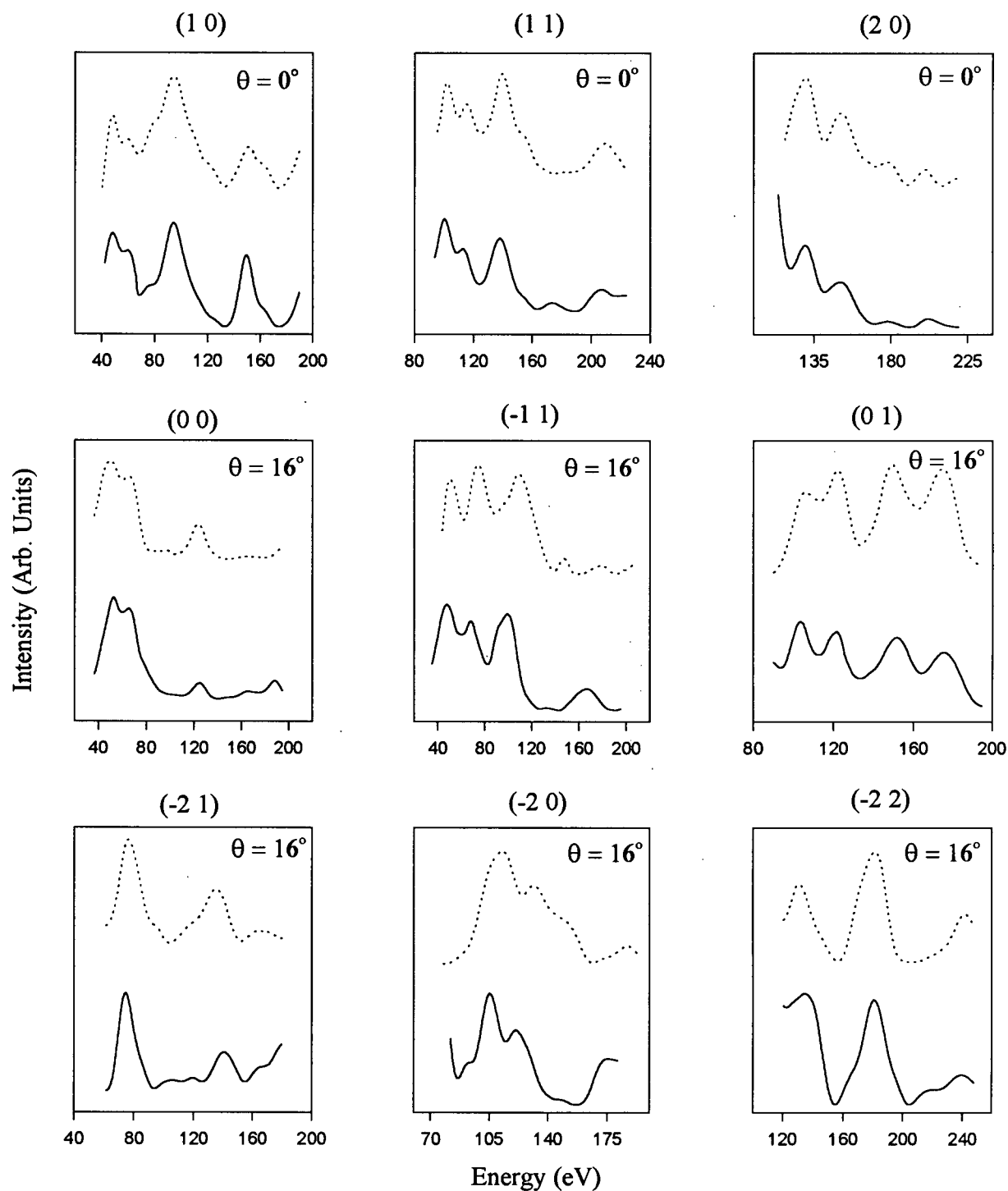
Figure 6.5   Experimental I(E) curves (dotted) for eight diffracted beams from the 2 ML O on Zr(0001) surface and compared to those calculated (full lines) for the (C)B(A$_t$)AB.. model with atomic coordinates given in Table 6.4.

Table 6.4   Atomic coordinates in Å for the TLEED-determined structure of the surface formed by 2 ML of O at Zr(0001) and corresponding to the model $(C)B(A_t)AB..$

Atomic label	X	Y	Z
O(1)	1.62	-0.93	0.00
Zr(1)	1.62	0.93	0.89
O(2)	0.00	0.00	2.11
Zr(2)	0.00	0.00	4.33
Zr(3)	1.62	0.93	6.89
Zr(4)	0.00	0.00	9.47
bulk repeat vector	1.6160	-0.9330	2.5738
	1.6160	0.9330	2.5738
2D repeat vector	1.6160	-2.7990	0.0000
	1.6160	2.7990	0.0000

The z-direction is perpendicular to the surface, and the x- and y-directions are parallel to $[11\overline{2}0]$ and $[\overline{1}100]$ respectively

6.3.3. Discussion

Oxygen has a strong tendency to incorporate into the structure of metallic zirconium (Section 5.3.5). Strictly for the conditions studied in this work, thermodynamics favors the dissolution of O into bulk Zr [148], and in turn kinetic factors must have a role in controlling the surface O/Zr(0001) systems that have been studied in this program, as well as in complementary work done elsewhere [17,156]. As the total O coverage increases, the partial ionic character is expected to get more established in the surface region, and this may reduce the activation barriers for O migrating back (e.g. from the second Zr-Zr interlayer spacing to the first). In any event, there are independent indications from measurements of both work function and Auger spectra that structural changes occur for the O/Zr(0001) system at around 1 ML [17,156,157]. Quite independently, the study here finds no support for the 2 ML structure corresponding to a simple extension from the models indicated for the 0.5 and 1 ML systems. For example, this analysis is not consistent with models like $A(C)B(C)AB..$ or $A(C_{0.5})B(C_{0.5})A(C_{0.5})B(C_{0.5})AB..$ being applicable to the 2 ML surface structure. In consequence, this work strongly supports a change in structure at above 1 ML, and accordingly we postulate that the changes in work function and Auger spectra previously noted for the O/Zr(0001) system in this coverage regime are associated with the formation of a ZrO_2-like surface model.

No new superstructure beams were observed by LEED for the 2 ML O/Zr(0001) system, and therefore the calculations made have assumed that the overlayer part of the structure involving O has the same diperiodic repeat dimensions as the Zr(0001) substrate. For the favored structure, this requires a lateral compression by about 10% in surface ZrO_2 compared with the cubic bulk structure [160] (3.60 to 3.23Å); accordingly this surface compound appears as having a modified form compared with known bulk forms of ZrO_2 (in any event the thermodynamically most stable bulk

form at normal conditions is baddeyelite which is monoclinic [164]). The stacking sequence identified for the top three layers in the 2 ML surface structure match those for the corresponding layers at the (111) surface of cubic ZrO_2 with anion termination. For the bulk (fluorite) structure, Tasker [165] noted, on the basis of electrostatic continuum calculations, that the non-polar, anion termination should be energetically favored over the polar, cation termination, for which the first four layers can be expressed as $A(B_t)(A_t)B..$. Consistent with this, the present work provides no support for the latter model type in the context of the 2 ML O/Zr(0001) surface system.

That the 0.5 ML (2×2) structure formed by O at the Zr(0001) surface involves O incorporating both between the first and second layers, and between the second and third layers, strongly suggests that O . . O electrostatic repulsions have a significant role in determining its form (a similar statement can also be made for the 1 ML structure). Additionally, incorporation into octahedral holes requires only a relatively small modification to the bulk Zr structure (e.g. the interlayer spacing increases from 2.57 to about 2.65 Å), and accordingly the O/Zr(0001) surfaces at 1 ML and below have structures related to that in (metastable) bulk ZrO, which adopts the NaCl lattice with the O atoms occupying octahedral hole sites with respect to the structure formed by the Zr atoms. But as the O coverage in the surface region increases, the most stable form may be expected to represent an appropriate balance between the various Zr to O, Zr to Zr and O to O bonding and repulsive interactions. As a simple example, the cation-termination model of surface ZrO_2, with the arrangement $A(B_t)(A_t)BA..$, seems less favorable than $(C)B(A_t)AB..$ entirely on grounds of the increased O . . O repulsions in the former.

However other comparisons are less direct. For example, Table 6.5 lists results from the first-principles total-energy calculations by Yamamoto for the 2 ML O/Zr(0001) surface structure [166]. In that work, the model $(B)A(C)BA..$ is favored over $(C)B(A_t)AB..$ by about 0.25 eV per O atom,

Table 6.5 Interlayer spacings, bond lengths (Å) and binding energies (eV per atom) for various models of the 2 ML O/Zr(0001) surface structure according to total-energy calculations of Yamamoto [166].

	(B)A(C)BAB..	(C)B(A)ABA..	(C)B(B)ABA..	(C)A(C)BAB
Center-of-mass spacing				
O(1) - Zr(1)	1.06	1.05	1.03	1.09
Zr(1) - O(2)	1.39	1.15	2.06	1.47
O(2) - Zr(2)	1.40	2.13	1.25	1.36
Zr(2) -Zr(3)	2.56	2.56	2.51	2.52
O-Zr Bond Length				
O(1) - Zr(1)	2.14	2.14	2.13	2.16
O(2) - Zr(2)	2.33	2.19	2.06	2.38
O(2) - Zr(3)	2.34	2.13	2.24	2.31
Binding Energy	-8.9855	-8.7315	-8.5026	-8.9592

although it is also noted that some of the calculated Zr-Zr interlayer spacings differ appreciably from those obtained from LEED analyses. Taking a purely ionic model for illustrative purposes, these two models would be expected to have atomic charges +3 and +1 for the first two Zr layers in (A)B(C)AB.., but +7/2 and +1/2 for the first two Zr layers in (C)B(A$_t$)AB... Assuming further that all ionic charges are uniformly distributed on the layers, and that their interlayer distances fit the conditions defined above for the choice of initial reference structure, then the electrostatic interactions among the first four layers are indicated to be proportional to -10.06 and -11.70 for the models (A)B(C)AB.. and (C)B(A$_t$)AB.. respectively. The latter appears to gain from more favorable attraction terms plus a reduction in the Zr$^{\delta+}$ . . Zr$^{\delta+}$ repulsion term, but these simplistic arguments do not of course take account of the covalent bonding terms that must also operate. In principle the total energy calculations should accommodate all these factors, but in addition there still remains an open question regarding the degree to which the surface structure studied by LEED is thermodynamically stable, even in the restricted sense of comparing with other structures where layers of O bond in the top three or so layers of Zr(0001).

Chapter 7: Concluding Remarks

7.1 Summary of New Results

7.1.1 XPS

The XPS work reported in this thesis represents exploratory research in which a thin film approach is used to study interfacial chemistry in the challenging O/Zr system. By keeping the film sufficiently thin, XPS could be used to reveal changes in the interfaces after exposure to reactive gases. In particular, studies were made of changes in the lower oxidation state material (ZrO_x), identified at the interface between oxide and substrate, that can be further oxidized to form ZrO_2 by either H_2O or O_2 at 300°C, although the process is hindered as the oxide layer gets thicker. A new observation was that exposure to D_2 can promote the ZrO_x to ZrO_2 conversion; this apparently remarkable result has opened up a series of subsequent research investigations [91,92]. The effect of H has also been recognized in these follow-up studies, which provide independent evidence that H can activate oxidation for a partially oxidized zirconium thin film. Such effects are likely to be relevant to the properties of oxide coatings on real CANDU pressure tube material, for which hydrogen is believed to have a destabilizing influence under certain circumstances.

7.1.2 LEED

New LEED crystallographic studies have been made for a cleaned Zr(0001) surface as well as for three surfaces with differing O coverages, and interesting changes in structural features have been identified as the coverage evolves. At the lower coverage, O incorporates into zirconium without too seriously disrupting the metal lattice. Both the 0.5 ML and 1 ML surface

structures have O atoms occupying octahedral holes in the metal, which can occur with only a small change (<4%) in the Zr-Zr interlayer spacing. Accordingly, they have structures related to that of bulk, but metastable, ZrO. Here O-O repulsive interactions appear to play an important role in determining the form of the structures. For example, in the 0.5 ML case, O-O repulsions are reduced by the O atoms incorporating both between the first and second metal layers, and between the second and third metal layers, with one (2×2) array being laterally displaced with respect to the other. As the coverage increases to 1 ML, O atoms still appear distributed into the same two interlayer regions. But now the O atoms are distributed somewhat randomly in the octahedral hole sites with a loss of long-range order. Further structural change is indicated for a total O coverage of about 2 ML; now 1 ML of O atoms incorporate into tetrahedral holes between the first and second Zr layers, and the other 1 ML of O occupy 3-fold sites on top of the Zr(0001) surface. This structure has surface layers resembling the stacking sequence at a (111) surface of cubic ZrO_2; this leads to 34% expansion in the first Zr-Zr interlayer spacing.

Chemical state evolution during the oxidation of zirconium appears to be seen in XPS as the lower oxidation state material that is converted to ZrO_2 in the oxidizing environment. The latter change can be identified directly since the amount of O present is limited, and its diffusion into the bulk is inhibited by the choice of a Au substrate. For the structural studies by LEED, the effect of O diffusion into bulk Zr is limited by kinetic factors associated with the temperature range used so that, in all three surface structures, the O atoms remain especially in the region of the first three Zr layers. For these conditions, the O concentration around the surface can increase with oxygen exposure, therefore leading to the formation of a surface oxide layer. Overall, these studies provide a picture for the evolution of chemical state and structure at the Zr interfaces during incipient oxidation.

7.2 Future Directions

This work has established some useful approaches which should help gain new fundamental information for interfacial properties of oxidized zirconium, with possible relevance to challenges related to pressure tube corrosion in nuclear reactors. Future expansions are possible in the following directions:

7.2.1 Interaction with H and H_2O

A particularly important future direction is to learn how an oxidized zirconium interface is chemically affected by incorporated H. Such information appears very relevant for establishing better understanding for nuclear reactor pressure tube corrosion. The XPS study reported here shows that the ZrO_2/ZrO_x interface provides a potentially important indicator of change below the oxide surface, but even so the mechanistic details of H bonding in these materials are still not known. Such information should be obtainable from vibrational spectroscopy, including high-resolution electron energy loss spectroscopy (HREELS) [167], and work is already planned in this direction. It is hoped that this will help to develop a mechanistic model for the role of H in the oxidation process, for example to distinguish between molecular and atomic adsorption, to identify underlayer absorption and the actual species involved (e.g. H, OH), and to determine conditions for H incorporation (temperature, defect sites etc.). Further, study of the H effect has fundamental scientific interest, even though the initial motivation was provided by the technological problem of pressure tube corrosion. Additionally, it will be interesting to study effects of deliberately added H on the Zr(0001) surface in relation to speculation that H contamination may affect some measured surface relaxations (noted in Chapter 5). Such work should help reveal the origin of discrepancies reported for surface

relaxations between the results from first principles calculations and from LEED, including for Zr(0001).

Water chemistry is relevant to the problem of corrosion in CANDU pressure tubes because one side of a tube is in contact with heavy water at 300°C. Observations in Chapter 3 have shown the ability of H_2O (at even very low pressure) to form oxide films and to oxidize partially oxidized films. Improved understanding is needed for the role of H_2O in relation to the details of dissociative adsorption and binding states, as well the conditions for water adsorption and dissociation (e.g. temperature, coverage). New structural information can be obtained by studying the interaction of H_2O with an oriented ZrO_2 surface using HREELS, in conjunction with other basic surface characterization techniques. As noted previously, ZrO_2 samples are not readily available for surface science study, but this work has established that the 2 ML O/Zr(0001) system should provide an useful model for the oxide surface. The quantitative side of this work also helps substantiate other studies where very thin layers of ZrO_2 are believed to have been prepared by depositing Zr in an oxidizing environment onto different substrates, including Pt(111) [84] and Au(111) [90].

7.2.2. Interfaces in Heterogeneous Material

Real pressure tube material for the CANDU reactor is not only heterogeneous in the vertical sense (i.e. variation in O composition with depth), but composition variations are known to be present as a result of its alloy nature (e.g. 2.5wt% Nb) and other impurities (e.g. Fe) which appear to affect interfacial properties [168-170]. Following the approach in this work, studies have been extended to those involving Zr/Nb, Zr/Fe, and Nb/Fe interfaces [171-174], but mechanistic information is still needed. Again vibrational spectroscopy (including HREELS)

should be particularly helpful for investigating the role of water interactions in these systems. For example, it should be useful to investigate how the presence of Nb or Fe may affect the nature of surface oxide, and its ability to incorporate H (e.g. from H_2O). The long-term aim of this program remains to study the chemistry of individual interfaces associated with heterogeneous CANDU pressure tube material, so that AECL scientists and others can build up a broader mechanistic model for its oxidation and interactions with molecules in its environment, including H_2O.

References

1   J.S. Foord, P.J. Goddard and R.M. Lambert, *Surf. Sci.* **94** (1980) 339.

2   M.Y. Zhou, R.H. Milne, M.A. Karolewski, D.C. Frost and K.A.R. Mitchell, *Surf. Sci.* **139** (1984) L181.

3   K.O. Axelsson, K.E. Keck and B. Kasemo, *Surf. Sci.* **164** (1985) 109; *Appl. Surf. Sci.* **25** (1986) 217.

4   C. Morant, J.M. Sanz, L.Galán, L.Soriano and F. Rueda, *Surf. Sci.* **218** (1989) 331.

5   R.L. Tapping, *J. Nucl. Mater.* **107** (1982) 151.

6   P. Sen, D.D. Sarma, R.C. Budhani, K.L Chopra and C.N.R. Rao, *J. Phys.* **F 14** (1984) 565.

7   C.O. De González and E.A. Garcia, *Surf. Sci.* **193** (1988) 305; C.O. De González and E.A. Garcia, *Appl. Surf. Sci.* **44** (1990) 211.

8   G.R. Corallo, D.A. Asbury, R.E. Gillbert and G.B. Hoflund, *Phys. Rev.* **B 35** (1987) 9451.

9   M. Tomita, T. Tanabe and S. Imoto, *Surf. Sci.* **209** (1989) 173; T. Tanabe and M. Tomita, *Surf. Sci.* **222** (1989) 84; T.Tanabe, M. Tanaka and S. Imoto, *Surf. Sci.* **187** (1987) 499.

10   M.C. Deibert, B.P. Thiesen and R. Kahraman, *Appl. Surf. Sci.* **35** (1989) 302.

11   J.M. Sanz, C. Palacio, Y. Casas and J.M. Martinez-Duart, *Surf. Interf. Anal.* **10** (1987) 177.

12   K. Griffiths, *J. Vac. Sci. Technol.* **A 6** (1988) 210.

13   G.B. Hoflund, D.F. Cox and R.E. Gilbert, *J. Vac. Sci. Technol.* **A 1** (1983) 1837.

14   K.C. Hui, R.H. Milne, K.A.R. Mitchell, W.T. Moore and M.Y. Zhou, *Solid State Commun.* **56** (1985) 83.

15   P.C. Wong, K.C. Hui, B.K. Zhong and K.A.R. Mitchell, *Solid State Commun.* **62** (1987) 293.

16   P.C. Wong and K.A.R. Mitchell, *Can. J. Phys.* **65** (1987) 464.

17   C.S. Zhang, B.J. Flinn, I.V. Mitchell and P.R. Norton, *Surf. Sci.* **245** (1991) 373.

18   C.S. Zhang, B.J. Flinn and P.R. Norton, *Surf. Sci.* **264** (1991) 1.

19   B.J. Flinn, C.S. Zhang and P.R. Norton, *Phys. Rev.* **B 47** (1993) 16499.

20   A. Stamper, D.W. Greve, D. Wong and T.E. Schlesinger, *Appl. Phys. Lett.* **52** (1989) 302.

21   Acronym based on CANada Deuterium Uranium; this nuclear reactor is manufactured by the Atomic Energy of Canada Ltd.

22   G.A. Somorjai, *Introduction to Surface Chemistry and Catalysis*, Wiley, New York, 1994

23   H. Heinemann and G.A. Somorjai, Eds. *Catalysis and Surface Science*, Marcel Dekker, New York, 1985.

24   R.N. Lamb, M. Grunze, J. Baxter, C.W. Kong and W.N. Unertl, in: *Adhesion and Friction*, Eds. M. Grunze and H.J. Kreuzer, Springer, Berlin, 1990.

25   L.K. Doraiswamy, *Prog. Surf. Sci.* **37** (1991) 1; L.K. Doraiswamy and S.D. Prasad, in: *Frontiers in Chemical Reaction Engineering* **I**, Eds. L.K. Doraiswamy and R.A. Mashelkar, Wiley Eastern, New Dehli, 1984.

26   D. Briggs and M.P. Seah, Eds. *Practical Surface Analysis by Auger and X-ray Photoelectron Spectroscopy*, John Wiley and Sons Ltd., West Sussex, 1990.

27   T.A. Carlson, *Photoelectron and Auger Spectroscopy*, Plenum, New York, 1975.

28   M.A. Chesters, *J. Electron Spectrosc. Relat. Pheno.* **38** (1986)123.

29   M.A. Van Hove *Surf. Rev. Lett.* **3** (1996) 1271; M.A. Van Hove, W.H. Weinberg and C.M. Chan, *Low Energy Electron Diffraction*, Springer, Berlin, 1986.

30   J.B. Pendry, *Low Energy Electron Diffraction*, Academic, New York, 1974.

31   F. Jona, P.M. Marcus and H.D. Shih, in: *Determination of Surface Structure by LEED*, Eds. P.M. Marcus and F. Jona, Plenum, New York, 1984.

32   A. Cachard and J.P. Thomas, in: *Material Characterization Using Ion Beams*, Eds. J.P. Thomas and A. Cachard, Plenum Press, NewYork, 1978.

33   A. Benninghoven, K.T.F. Janssen, J. Tümpner and H.W. Werner, Eds. *Secondary Ion Mass Spectrometry SIMS* **VIII**, Wiley, New York, 1992.

34   C.M. Chan, R. Aris and W.H. Weinberg, *Appl. Surf. Sci.* **1** (1978) 360.

35   M. Cardona and L. Ley, in: *Topics in Applied Physics* **26**, Eds. M. Cardona and L. Ley, Springer-Verlag, 1978.

36   K. Heinz, *Prog. Surf. Sci.* **27** (1988) 239.

37   C.S. Zhang, B. Li and P.R. Norton, *J. Alloy Comp.* **231** (1995) 354; C.S. Zhang, B.J. Flinn, K. Griffiths, *J. Vac. Sci. Technol.* **A 10** (1992) 2560.

38   B. Li, K. Griffiths, C.S. Zhang and P.R. Norton, *Surf. Sci.* (In Press).

39   B.D. Warr, E.M. Rasile, A.M. Brennenstuhl, M.B. Elmoselhi, N.S. McIntyre, S.B. Newcomb and W.M. Stobbs, in: *Proc. 1st Int. Conf. on Microscopy of Oxidation*, University of Cambridge, Eds. M.J. Bennett and G.W. Lorimer (The Institute of Metals, 1990) 292.

40   T. Laursen, J.R. Leslie and R.L. Tapping, *J. Nucl. Mater.* **182** (1991) 151.

41   P.C. Lichtenberger, N. Ramasubramanian, B.D. Warr, R.L. Tapping and V.F. Urbanic, *Hydrogen Ingress in Zr-Nb Pressure Tubes*, Ontario Hydro Report No. **91-270-P**, COG No. **91-277** (1991).

42   N.S. McIntyre, R.D. Davidson, C.G. Weisener, B.D. Warr and M.B. Elmoselhi, *Surf. Interf. Anal.* **17** (1991) 757.

43   J. Kondo, Y. Sakata, K. Domen, K. Maruya and T. Onishi, *J. Chem. Soc. Faraday Trans.* **86** (1990) 397.

44   T. Onishi, H. Abe, K. Maruya and K. Domen, *J. Chem. Soc. Chem. Commun.* (1985) 617.

45   N. Schönberg, *Acta Chem. Scand.* **8** (1954) 627, 1460.

46   E. Bauer, *Vacuum* **22** (1972) 539.

47   J.C. Riviere, *Surface Analytical Techniques*, Clarendon Press, Oxford, 1990.

48   G.A. Somorjai, *Chemistry in Two Dimensions: Surfaces*, Cornell University Press, Ithaca, N.Y. 1981.

49   M.P. Seah and W.A. Dench, *Surf. Interf. Anal.* **1** (1979) 2.

50   H. Hertz, *Annal. Phys.* **31** (1887) 982; A. Einstein, *Anal. Phys.* **17** (1905) 132.

51   H. Robinson and W.F. Rawlinson, *Phil. Mag.* **28** (1914) 277; H. Robinson, *Phil. Mag.* **50** (1925) 241.

52   K. Siegbahn, C.N. Nording, A. Fahlman, R. Nordberg, K. Hamrin, J. Hedman, G. Johansson, T. Bermark, S.E. Karlsson, I. Lindgren and B. Lindberg, *ESCA: Atomic, Molecular and Solid State Structure Studied by Means of Electron Spectroscopy*, Almqvist and Wiksells, Uppsala, 1967.

53   C.R. Brundle and M.W. Roberts, *Proc. Roy. Soc.* **A 331** (1972) 383.

54   D. Finello and H.L Marcus, in: *Electron and Positron Spectroscopies in Material Science and Engineering*, Eds. O. Buck, J.K. Tien and H.L. Marcus, Academic Press, New York, 1979.

55   L.C. Feldman and J.W. Mayer, Eds. *Fundamentals of Surface and Thin Film Analysis*, Elsevier Science, New York, 1986.

56   P.W. Palmberg, *Anal. Chem.* **45** (1973) 549.

57   M.E. Packer and J.M. Wilson, *Auger Transitions*, Institute of Physics, London, 1973; P.W. Palmberg, G.E. Riach, R.E. Weber, and N.C. MacDonald, *Handbook of Auger Electron Spectroscopy*, Physical Electronics Industries, Inc. Edina, 1972.

58   G.E. Muilerbery, Ed. *Handbook of X-ray Photoelectron Spectroscopy*, Perkin Elmer, Minnesota, 1979.

59   Y.L. Leung, Master thesis, University of British Columbia, 1992.

60   MAX200 User Manual (Leybold, Koln, Germany).

61   B.D. Ratner, T.A. Horbett, D. Shuttleworth and H.R. Thomas, *J. Collid Interf. Sci.* **83** (1981) 630.

62   T.D. Bussing and P.H. Holloway, *J. Vac. Sci. Technol.* **A 3** (1985) 1973.

63   Yu.G. Abashkin, S.E. Borodyanskii, L.A. Vasil'ev and A.P. Dement'ev, *Poverkhost*, **10** (1989) 71.

64   G.C. Smith and A.K. Liversey, *Surf. Interf. Anal.* **19** (1992) 175.

65   P.J. Cumpson, *J. Electron Spectrosc. Relat. Pheno.* **73** (1995) 25.

66   C.S. Fadley, *Prog. Surf. Sci.* **16** (1984) 275; C.S. Fadley, *Surf. Sci. Rep.* **19** (1993) 231.

67   C.S. Fadley, M.A. Van Hove, A.P. Kaduwela, *J. Electron Spectrosc. Relat. Pheno.* **75** (1995) 273.

68   W.F. Egelhoff Jr., *CRC Crit. Rev. Solid State Mater. Sci.* **16** (1990) 3.

69   S.A. Chambers, *Adv. Phys.* **40** (1991) 357.

70   G. Ertl and J. Küppers, *Low Energy Electrons and Surface Chemistry*, VCH Verlags, Weinheim, 1985.

71   H.E. Bishop, J.P. Coad and J.C. Riviere, *J. Electron Spectrosc. Relat. Pheno.* **1** (1972) 389.

72   J.A. Simpson, in: *Methods of Experimental Physics*, Eds. V.W. Hughs and H.L. Schultz, **4A**, Academic Press, New York, 1967.

73   L.J. Richter and W. Ho, *Rev. Sci. Instrum.* **57** (1986) 1469.

74   D.A. Shirley, *Phys. Rev.* **B 5** (1972) 4709.

75   H.E. Bishop, *Surf. Interf. Anal.* **3** (1981) 372.

76   M.C. Burrell and N.R. Armstrong, *Appl. Surf. Sci.* **17** (1983) 53.

77   S. Tougaard, *J. Electron Spectrosc. Relat. Pheno.* **52** (1990) 243.

78   T. Laursen, M. Leger, X.P. Ma, J.D. MacArthur, G.R. Palmer and J.L. Whitton, *J. Nucl. Mater.* **165** (1989) 156.

79   J.S. Forster, T.K. Alexander, D. Phillips and R.L. Tapping, *Nucl. Instr. Meth.* **B 56/57** (1991) 821.

80   F.R. Ding, P.R. Okamoto and L.E. Rehn, *J. Mater. Res.* **4** (1989) 1444.

81   Y.T. Cheng, A.A. Dow and B.M. Clemens, *Appl. Phys. Lett.* **53** (1988) 1346.

82   G. Hultquist, G.K. Chuah and K.L Tan, *Corros. Sci.* **31** (1990) 149.

83   Y.L Leung, M.Y. Zhou, P.C. Wong , K.A.R. Mitchell, *Appl. Surf. Sci.* **62** (1992) 175.

84   V. Maurice, M. Salmeron and G.A. Somorjai, *Surf. Sci.* **237** (1990) 116.

85   P. Steiner, S. Hüfner, N. Mårtensson and B. Joansson, *Solid State Commun.* **37** (1981) 73.

86   N. Mårtenson and B. Johansson, *Solid State Commun.* **32** (1979) 791.

87   B. Johansson and N. Mårtensson, *Phys. Rev.* **B 21** (1980) 4427.

88   P.R. Davis, *Surf. Sci.* **91** (1980) 385.

89   U. Bardi, P.N. Ross and G.A. Somorjai, *J. Vac. Sci. Technol.* **A 2** (1984) 40.

90   J.R. Lou, U. Hess and K.A.R. Mitchell, *Appl. Surf. Sci.* **62** (1992) 175.

91   P.C. Wong, Y.S. Li, M.Y. Zhou and K.A.R. Mitchell, *Appl. Surf. Sci.* **89** (1995) 255.

92   Y.S. Li, P.C. Wong and K.A.R. Mitchell, *Appl. Surf. Sci.* **89** (1995) 263.

93   V.E. Henrich, *Rep. Prog. Phys.* **48** (1985) 1481; *Prog. Surf. Sci.* **9** (1979) 143.

94   T. Norby, in: *Zirconia '88: Advances in Zirconia Science and Technology*, Eds. S. Meriani and C. Palmonari, Elsevier , London, 1988.

95   D.L. Douglass, *The Metallurgy of Zirconium*, IAEA, Vienna, 1971.

96   T. Norby, in: *Selected Topics in High Temperature Chemistry: Defect Chemistry of Solids*, Eds. O. Johansen and A.G. Andersen, Elsevier, Amsterdam, 1989.

97   F.M. Ernsberger, *J. Am. Ceram. Soc.* **66** (1983) 747.

98   C.J. Davisson and L.H. Germer, *Nature* **119** (1927) 558; *Phys. Rev.* **29** (1927) 908; *Phys. Rev.* **30** (1927) 705.

99   R. Feidenhans'l, *Surf. Sci. Rep.* **10** (1989) 105; I.K. Robinson and D.J. Tweet, *Rep. Prog. Phys.* **55** (1992) 599.

100   J.F. van der Veen, *Surf. Sci. Rep.* **5** (1985) 199.

101   R. Wiesendanger and H.-J. Güntherodt, Eds. *Scanning Tunneling Microscopy* I, Springer-Verlag, Berlin, 1994.

102   J. Stöhr, in: *X-ray Absorption*, Eds. D.C. Koningsberger and R. Prins, Wiley, New York, 1988.

103   P.J. Rous, *Prog. Surf. Sci.,* **39** (1992) 3.

104   A. Messiah, *Quantum Mechanics* **II**, North-Holland, Amsterdam, 1962.

105   E.A. Wood, *J. Appl. Phys.* **35** (1964) 1306.

106   P.L. Park and H.H. Madden, *Surf. Sci.* **11** (1968) 188; P.J. Estrup and E.G. Mcrrae, *Surf. Sci.* **25** (1971) 1.

107   G. Comsa, *Surf. Sci.* **81** (1979) 57.

108   M. Henzler, *Appl. Surf. Sci.* **11/12** (1982) 450.

109   K. Heinz, *Vacuum* **41** (1990) 328.

110   D.K. Saldin, J.B. Pendry, M.A. Van Hove and G.A. Somorjai, *Phys. Rev.* **B 31** (1985) 1216; G.S. Blackman, M.-L. Xu, M.A. Van Hove and G.A. Somorjai, *Phys. Rev. Lett.* **61** (1988) 2352.

111   G.H. Stout and L.H. Jensen, *X-ray Structure Determination: A Practical Guide*, Wiley, New York, 1989.

112   J.A. Strozier Jr., D.W. Jepsen and F. Jona, in: *Surface Physics of Materials* **I**, Ed. J.M. Blakely, Academic, New York, 1975.

113   S.Y. Tong, *Prog. Surf. Sci.* **7** (1975) 1.

114   M.A. Van Hove and S.Y. Tong, *Surface Crystallography by LEED*, Springer, Berlin, 1979.

115   N. Stoner, M.A. Van Hove and S.Y. Tong, in: *Characterization of Metal and Polymer Surface*, Ed. L.-H. Lee, Academic Press, New York, 1977.

116   D.W. Jepsen, P.M. Marcus and F. Jona, *Phys. Rev.* **B 8** (1972) 2436.

117   A. Messiah, *Quantum Mechanics* **I**, North-Holland, Amsterdam, 1970.

118   A.A. Maradudin, E.M. Montroll, G.H. Weiss and I.P. Ipatova, *Theory of Lattice Dynamics in the Harmonic Approximation*, Academic Press, New York, 1971.

119   D.W. Jepsen and P.M. Marcus, in: *Computational Methods in Band Theory*, Eds. P.M. Marcus, J.F. Janak and A.R. Willams, Plenum Press, New York, 1971.

120   V.L. Moruzzi, J.F. Janak and A.R. Williams, *Calculated Electronic Properties of Metals*, Pergamon, New York, 1978.

121   J.E. Demuth, D.W. Jepsen and P.M. Marcus, *Phys. Rev. Lett.* **31** (1973) 540.

122   C.B. Duke, *Adv. Chem. Phys.* **27** (1974) 1.

123   S.Y. Tong and M.A. Van Hove, *Phys. Rev.* **B 16** (1977) 1459.

124   J.B. Pendry, *J. Phys.* **C 4** (1971) 3095.

125   J.L. Beeby, *J. Phys.* **C 1** (1968) 82.

126   W.S. Yang, F. Jona, *Phys. Rev.* **B 28** (1983) 2049.

127   P.W. Palmberg, G.K. Bohn and J.C. Tracy, *Appl. Phys. Lett.* **15** (1969) 254.

128   H.Z. Sar-el, *Rev. Sci. Instrum.* **38** (1967) 1210;. H. Hafner, J.A. Simpson and C.E. Kuyatt, *Rev. Sci. Instrum.* **39** (1968) 33.

129   R.K. Wild, *Vacuum* **31** (1981) 183; N.A. Alford, A. Barrie, I.W. Drummond and Q.C. Herd, *Surf. Interf. Anal.* **1** (1979) 36.

130   H.L. Davis and J.R. Noonan, *Surf. Sci.* **115** (1982) L75.

131   M.A. Van Hove and R.J. Koestner, in: *Determination of Surface Structure by LEED*, Eds. P.M. Marcus and F. Jona, Plenum Press, New York, 1984.

132   J.B. Pendry, *J. Phys.* **C 13** (1980) 937.

133   J.N. Anderson, H.B. Nielsen, L. Petersen and D.L. Adams, *J. Phys.* **C 17** (1984) 173.

134   P.J. Rous, M.A. Van Hove and G.A. Somorjai, *Surf. Sci.* **226** (1990) 15; A. Wander, M.A. Van Hove and G.A. Somorjai, *Phys. Rev. Lett.* **67** (1991) 626; M.A. Van Hove, W. Moritz, H. Over, P.J. Rous, A. Wander, A. Barbieri, N. Materer, U. Starke and G.A. Somorjai, *Surf. Sci. Rep.* **19** (1993) 191.

135   P.J. Rous, J.B. Pendry, D.K. Saldin, K. Heinz, K. Müller and N. Bickel, *Phys. Rev. Lett.* **57** (1986) 1951.

136   N. Bickel, K. Heinz, H. Landskron, P.J. Rous, J.B. Pendry and D.K. Saldin, in: *The Structure of Surface* **II**, Eds. J.F. van der Veen and M.A. Van Hove, Springer, Berlin, 1988.

137   J.B. Pendry, K. Heinz, W. Oed, H. Landskron, K. Müller and G. Schmidtlein, *Surf. Sci.* **193** (1988) L1.

138   P.J. Rous and J.B. Pendry, *Surf. Sci.* **219** (1989) 355, 373; *Comput. Phys. Commun.* **54** (1989) 137, 157.

139   W.B. Pearson, *A Handbook of Lattice Spacings and Structures of Metals and Alloys*, Pergamon Press, 1958.

140   W.T. Moore, P.R. Watson, D.C. Frost and K.A.R. Mitchell, *J. Phys.* **C 12** (1979) L887.

141   K.C. Hui, *Ph.D. Thesis*, University of British Columbia, 1986.

142   F.M. Cain Jr., *Zirconium and Zirconium Alloys*, American Soc. Metals, 1953.

143   P.C. Wong, *Ph.D. thesis*, University of British Columbia, 1987.

144   H.D. Shih, F. Jona, D.W. Jepsen and P.M. Marcus, *J. Phys.* **C 9** (1976) 1405.

145   G. Michalk, W. Moritz, H. Pfnür and D. Menzel, *Surf. Sci.* **129** (1983) 92.

146   M. Yamamoto, C.T. Chan and K.M. Ho, *Phys. Rev.* **B 50** (1994) 7932.

147   P.J. Feibelman, *Surf. Sci.* **360** (1996) 297.

148   B. Cox, University of Toronto, private communication.

149   B. Holmberg and T. Dagerhamn, *Acta Chem. Scand.* **15** (1961) 919.

150   L. Pauling, *Nature of the Chemical Bond*, Cornell University Press, Ithaca, 1960.

151   I. Manassidis, A.De Vita and M.J. Gillan, *Surf. Sci.* **285** (1993) L517.

152   W.C. Mackrodt, R.J. Davey, S.W. Black and R. Docherty, *J. Cryst. Growth* **80** (1987) 441.

153   M. Yamamoto, S. Naito, C.T. Chan and K.M. Ho, Abstract for Meeting of *American Physical Society*, March, 1995.

154   H. Pfnür, G. Held, M. Lindroos and D. Menzel, *Surf. Sci.* **220** (1989) 43; M. Lindroos, H. Pfnür, G. Held and D. Menzel, *Surf. Sci.* **222** (1989) 451.

155   J.R. Lou, *Ph.D. Thesis*, University of British Columbia, 1992.

156   C.S. Zhang, B.J. Flinn and P.R. Norton, *Surf. Sci.* **264** (1992) 1.

157   B.J. Flinn, *Ph.D. Thesis*, University of Western Ontario, 1992.

158   B.L. Györffy and G.M. Stocks, in: *Electrons in Disordered Metals and at Metallic Surfaces,* Eds. P. Phariseau, B.L. Györffy and L. Scheire, Plenum, New York, 1979; F. Jona, K.O. Legg, H.D. Shih, D.W. Jepsen and P.M. Marcus, *Phys. Rev. Lett.* **40** (1978) 1466.

159   See, for example, Y. Gauthier, Y. Joly, R. Baudoing and J. Rundgren, *Phys. Rev.* **B 31** (1985) 6216; J.M. Bugnard, R. Baudoing-Savois, Y. Gauthier and E.K. Hill, *Surf. Sci.* **281** (1993) 62; R. Döll, M. Kottcke, K Heinz, L. Hammer, K. Müller and D.M. Zehner, *Surf. Sci.* **307-309** (1994) 434.

160   G. Katz, *J. Am. Ceram. Soc.* **54** (1971) 531.

161   I.D. Brown and D. Altermatt, *Acta Crystallogr.* **B 41** (1985) 244.

162   K.A.R. Mitchell, S.A. Schlatter and R.N.S. Sodhi, *Can. J. Chem.* **64** (1985) 1435.

163   H. Ohtani, C.T. Kao, M.A. Van Hove and G.A. Somorjai, *Prog. Surf. Sci.* **23** (1986) 155.

164   D.K. Smith and H.W. Newkirk, *Acta Crystallogr.* **18** (1965) 983.

165   P.W. Tasker, in: *Computer Simulation of Solids*, Eds. C.R.A. Catlow and W.C. Mackrodt, Springer-Verlag, Berlin, 1982.

166   M. Yamamoto, Kyoto University, to be published.

167   H. Ibach and D.L. Mills, *Electron Energy Loss Spectroscopy and Surface Vibrations*, Academic Press, 1982.

168   Y. Ding and D.O. Northwood, *J. Alloy Comp.* **187** (1992) 317.

169   D. Khatamian and F.D. Manchester, *J. Nucl. Mater.* **166** (1989) 300.

170   T.L. Laursen and J.R. Leslie, *J. Nuclear. Mater.* **182** (1991) 158.

171   Y.S. Li, K.C. Wong, P.C. Wong and K.A.R. Mitchell, *Appl. Surf. Sci.* (In Press).

172   K.C. Wong, P.C. Wong, Y.S. Li and K.A.R. Mitchell, *Surf. Rev. Lett.* (In Press).

173   Y.S. Li, W. Liu, P.C. Wong and K.A.R. Mitchell, *Surf. Rev. Lett.* **2** (1995) 759.

174   P.C. Wong, K.C. Wong, Y.S. Li and K.A.R. Mitchell, *Surf. Rev. Lett.* **2** (1995) 495.

List of Publications

XPS Studies of the Stability and Reactivity of Thin Films of Oxidized Zirconium

Y.M. Wang, Y.S. Li, P. C. Wong and K.A.R. Mitchell, *Appl. Surf. Sci.* **72** (1993) 237-244

A LEED Crystallography Analysis for the Half Monolayer Structure Formed by O at the Zr(0001) Surface

Y.M. Wang, Y.S. Li and K.A.R. Mitchell, *Surf. Sci.* **342** (1995) 272-280.

LEED Analyses Revisited for Two Structures Formed by Zr(0001): The Surface when Clean and when containing Sufficient Oxygen to Just Extinguish the Half-Order Beams

Y.M. Wang, Y.S. Li and K.A.R. Mitchell, *Surf. Sci.* **343** (1995) L1167-1173.

LEED Analysis of the Surface Structure Formed by Two Monolayers of O at Zr(0001) Surface

Y.M. Wang, Y.S. Li and K.A.R. Mitchell, *Surf. Sci.* submitted